Molecular Sensors for Biological Applications

Nsikak Bassey Essien

Thesis submitted in part fulfilment of the requirements for the degree of Doctor of Philosophy

University of Sussex

January 2023

This is dedicated to God Almighty,

Who has given me the grace to keep fighting even when the odds seem insurmountable?

Declaration

I hereby confirm that this thesis is my own unless otherwise stated. This thesis is presented and conforms to a 'papers-style' format in which Chapters 2-5 comprise individual articles written in a style suitable for publication in peer-reviewed journals. Chapter 1 serves as a general introduction to key chemical concepts and literature related to this work. Chapter 6 offers a discussion of the presented works as a whole and discusses future research directions. Chapter 7 outlines the experimental details and synthetic procedures presented in this work.

Nsikak Bassey Essien

Chapter 2 is to be submitted for publication as follows:

'Asymmetric salan fluorescent selective Cu^{2+} sensors'

Nsikak B. Essien, Dimitrios A. Diamantis, Spyridon D. Katsakos, Antal Galvácsi, Csilla Kállay, Ramón González-Méndez, Andreas G. Tzakos, Alfredo Vargas, George E. Kostakis.

The author's contribution is as follows: G.E. Kostakis devised the project with critical input from Nsikak B. Essien. Nsikak B. Essien was responsible for the synthesis and characterisation of all the ligands and performed preliminary fluorescent studies. G E. Kostakis performed and evaluated the crystallographic data. D. A. Diamantis, S. D. Katsakos and A. G. Tzakos performed the systematic fluorescent evaluation. A. Galvácsi and C. Kállay performed solution studies. R. González-Méndez performed and evaluated MS studies. A. Vargas performed theoretical calculations. All authors contributed to the preparation of the article.

Chapter 3 is to be submitted for publication as follows:

'Fluorine-based Zn complexes for amine sensing'

Nsikak B. Essien, Antal Galvácsi, Csilla Kállay, Youssra Al-Hilaly, Ramón González-Méndez, Geoffrey R. Akien, Graham J. Tizzard, Simon J. Coles, Maria Besora, George E. Kostakis

The author's contribution is as follows: G.E. Kostakis devised the project with critical input from Nsikak B. Essien and he was responsible for the synthesis and characterisation of all the ligands and complexes as presented and performed the sensing studies with ^{19}F NMR. G E. Kostakis, G. J. Tizzard and S. J. Coles performed and evaluated the crystallographic data. A. Galvácsi and C.

Kállay performed solution studies. Y. Al-Hilaly performed and helped with the evaluation of circular dichroism studies. R. González-Méndez performed and evaluated MS studies. G. R. Akien performed diffusion ^{19}F NMR studies. Maria Besora performed theoretical calculations. All authors contributed to the preparation of the article.

Chapter 4 is to be submitted for publication as follows:

'Multimodal molecular γ-aminobutyric acid (GABA) sensor'

Nsikak B. Essien, Antal Galvácsi, Csilla Kállay, Youssra Al-Hilaly, Jamie Lai-Morrice, Cristina Pubill Ulldemolins, Louise Serpell, and George E. Kostakis

The author's contribution is as follows: G.E. Kostakis devised the project with critical input from Nsikak B. Essien. Nsikak B. Essien was responsible for the synthesis and characterisation of the ligand and complexes presented with input from Harry Carpenter. Nsikak B. Essien performed titration studies with ^{19}F NMR. Y. Al-Hilaly performed and helped with the evaluation of fluorescent studies. A. Galvácsi and C. Kállay performed solution studies. J. Lai-Morrice and C. Pubill Ulldemolins performed theoretical calculations. All authors contributed to the preparation of the article.

Chapter 5 is to be submitted for publication as follows:

*'*Molecular fluorine-based probes for heavy metals ion detection*'*

Nsikak B. Essien, Antal Galvácsi, Csilla Kállay, Maria Besora, and George E. Kostakis

The author's contribution is as follows: Nsikak B. Essien was responsible for the initial conception of the project with critical input from G.E. Kostakis, Nsikak B. Essien was responsible for all the design, synthesis and characterisation of all the ligands, and complexes presented as well performed preliminary ^{19}F NMR titration studies. A. Galvácsi and C. Kállay performed solution studies and ^{19} FNMR titration measurements with HMIs..G E. Kostakis performed and evaluated the crystallographic data. Maria Besora performed theoretical calculations. All authors contributed to the preparation of the article.

I hereby declare that this thesis has not been and will not be, submitted in whole or in part to another University for the award of any other degree.

Signature:

Acknowledgements

All praises go to the Almighty God for his grace, love, support, and strength over the challenging times during my PhD period. May the name of the Lord be continually blessed; in Jesus' name, amen.

I also express my deepest gratitude to my primary supervisor, Dr George E. Kostakis, whose scholarly guidance, keen interest, and encouragement have been a source of great inspiration throughout my research program. I cannot thank him enough for the incredible work he offered in terms of pieces of advice, corrections, and the faith he had in me; indeed, I have learned a lot.

I also offer special thank you to my co-supervisor, Dr J.F.C. Turner, for all his general advice, listening ears, and very ready-to-assist attitude, I am grateful to you, and I am also very appreciative and thankful to the following collaborators, Dr Csilla Kallay, Prof Louise Serpell, Prof John spencer, Dr Andreas G. Tzakos, Dr Alfredo Vargas, Dr Christina Pubill Ulldemolins, Dr Geoffrey Akien, Dr Maria Besora Bonet. Dr Andrew McGown, Dr Mahmoud Maina, and Dr Graham J. Tizzard for all their indelible contributions that make this thesis possible.

While mastering the concept of science, they have been other people I have come across like Dr Ian Crossley, Dr Eddy Viseaux, Emma Chorley, Dr Jack Davenport, Ghada , Mohammed, Dr Storm Hassel-Har, Helena, Joy, Lorna, Asma, I am so happy to have met these people.

I also want to give warm thanks to my family, Ukeme(wife), who took the responsibility of being both a wife, mother and temporary father to my lovely kids when I was absent studying to make them proud; I want to thank Isabella, Olivia (Kids) for enduring my absence even at a very tender age during this challenging period of my studies. I am also grateful to Elder and Elder (Mrs) B. U. Essien (Parents) Dr Essien, Ini-obong Essien (Brothers), Ekaette, Idongesit and Prof (Mrs) Aniema (Sisters) for their prayers, faith, moral support they all gave me.

I will not fail to express my gratitude to the management of Akwa Ibom State Polytechnic, who shortlisted and recommended me for sponsorship by the Tertiary education trust fund (Tet fund), thereby making my PhD dream possible. I cannot thank them enough for these kind gestures.

Lastly, I sincerely appreciate the Tertiary Education trust fund's sponsorship and the opportunity it offered me to undertake my PhD program at the University of Sussex.

Abstract

The PhD thesis centres on designing, synthesising, and fine-tuning the novel symmetric and asymmetric ligands derived from the ethylenediamine backbone to form molecular compounds. Some of the novel asymmetric molecular compounds were investigated for their sensing potentials using fluorescence spectroscopy, and results obtained show that they can selectively sense for the presence of Cu^{2+} and Fe^{3+} in an aqueous medium; the next chapter highlights the novel synthesis of chiral molecular compounds and their corresponding zinc complexes for sensing biologically important chiral amines, the mechanism of sensing was studied using ^{19}F-NMR spectroscopy, other novels symmetric and asymmetric molecular compounds were synthesis. Their corresponding zinc and yttrium complexes were used to sense for the presence of HMPs and Neurotransmitters, respectively, for the two other chapters and results presented and discussed.

Chapter 1 This aims to showcase to the reader the motivation, drive, design and development of the chemical concepts and literature discussed throughout the thesis; it further introduces some key concepts and considerations in coordination chemistry related to multiple ligand design and complex development. The second section introduces the reader to the ligand scaffolds and relevant areas of the research in this thesis.

Chapter 2 showcases a novel synthetic methodology for the synthesis of novel fluorescent asymmetric salan ligands. It investigates their sensing ability towards first-row transition elements with fluorescence. Computational studies underscore the selective sensing mechanism.

Chapter 3 presents the design, synthesis and characterisation of novel fluorine-based salan ligands and corresponding zinc complexes. The latter were used for chiral amine sensing with ^{19}F-NMR. Computational and solution state studies are also presented, and their sensing mechanism towards different analytes are discussed.

Chapter 4 presents the ligand design and synthesis of a new asymmetric water-soluble inexpensive heptandentate $H_4oct^{(p\text{-}OCF3)}salox$ ligand and the corresponding Yttrium complex $[Yoct^{(p\text{-}OCF3)}salox]^-$. The latter has been used for neurotransmitter sensing. The process has been monitored using ^{19}F-NMR, Fluorescence and UV-Vis spectroscopy. DFT calculations were also conducted providing useful insights regarding the interaction mechanism.

Chapter 5 presents the ligand design and the synthesis of a family of symmetric and asymmetric fluorine-based novel salan ligands and their corresponding zinc complexes. The latter entities

were used as molecular fluorine-based probes for detecting heavy metal ions in DMSO-H_2O solution.

Chapter 6 This shows the overall conclusion of this thesis and enlightens on the contributions that the presented thesis has made to their relevant fields. Suggested potential future directions in the relevant research areas are also discussed.

Chapter 7 contains the experimental designs and synthetic procedures. The bibliography of this work is presented in **Chapter 8**.

List of Abbreviations

AAS	Atomic absorption spectroscopy
Å	Angstrom
AC	Acetylcholine
CE	Capillary electrophoreses
CD	Circular dichroism
CH_3	Methyl group
DCM	Dichloromethane
DMSO	Dimethyl sulfoxide
DFT	Density functional theory
en	Ethylenediamine
ETS-NOCV	Extended transition state-natural orbitals for chemical valence
EPR	Electron paramagnetic resonance
ESI-MS	Electron spray ionization mass spectroscopy
FSCV	Fast-scan cyclic voltammeter
FTI	Fourier Transform Infrared spectroscopy.
GABA	Gamma amino butyric acid
HMPs	Heavy Metal Pollutants
HPLC	High-performance liquid chromatography
HRMS	High-resolution mass spectrometry
HSAB	Hard Soft Adic Base
ICP-AES	Inductively coupled plasma atomic emission spectroscopy.
ICP-OES	Inductively coupled plasma optical emission spectroscopy.
IUPAC	International Union of Pure and Applied Chemistry
LC	Liquid Chromatography
LMCT	Ligand to Metal Charge Transfer
Logβ	Complex stability constants
MeCN	Acetonitrile
MEP	Molecular electrostatic potential

Met	Methionine
Mg	Milligram
mL	Millilitre
mmol	Millimole
MOF	Metal-organic framework
MRI	Magnetic resonance imaging
MS	Molecular sieves
MW	Molecular weight
NMR	Nuclear magnetic resonance
NT	Neurotransmitter
PCM	Polarisable continuum model
Pm	Picometres
ppm	Parts per million
R.T.	Room temperature
ROS	Reactive oxygen species
Sal	Salicylaldehyde
SARS	Structural Activity Relationship Studies
SET	Single electron transfer
SER	Serotonine
SMMC	Small molecule metal chelator
Sqp	Square planar
SXRD	Single-crystal X-ray diffraction
TGA	Thermogravimetric analysis
THF	Tetrahydrofuran
Td	Tetrahedral
WHO	World Health Organization

Table of Contents

Chapter 1: General introduction

Salan ligands, hereto salans, are well-known organic scaffolds in coordination chemistry, mainly comprising tetradentate donors set N_2O_2. They are obtained through a condensation reaction between two equivalents of salicylaldehyde (Sal) and ethylenediamine (en), followed by reduction amination, usually performed with $NaBH_4$ (Figure 1.1).[1] Salans impose a flexible character compared to the corresponding salens, due to the presence of six atoms with sp^3 character. Salans form complexes with metal ions by coordinating the nitrogen and oxygen donor atoms. Steric and electronic effects around the metallic core can be fine-tuned through an appropriate selection of electron-withdrawing or electron-donating substituents. The oxygen and nitrogen donor atoms induce opposite electronic effects: the N atoms are soft donors and stabilize the lower oxidation state, while the phenolate O atoms, as hard donors, stabilize the higher oxidation state of the metal ion (Figure 1.1).[2] As such, salans can stabilize metals in different oxidation states. Their complexes with transition elements, mainly 3d, have applications in other areas, including sensing, pharmaceuticals, therapeutics, luminescence, magnetism, zeolite matrices and catalysis.[3,4,13–15,5–12] This thesis focuses on the design of new salans and their corresponding complexes with 3d-transition elements. It explores the use of these molecular entities as sensors for biological applications.

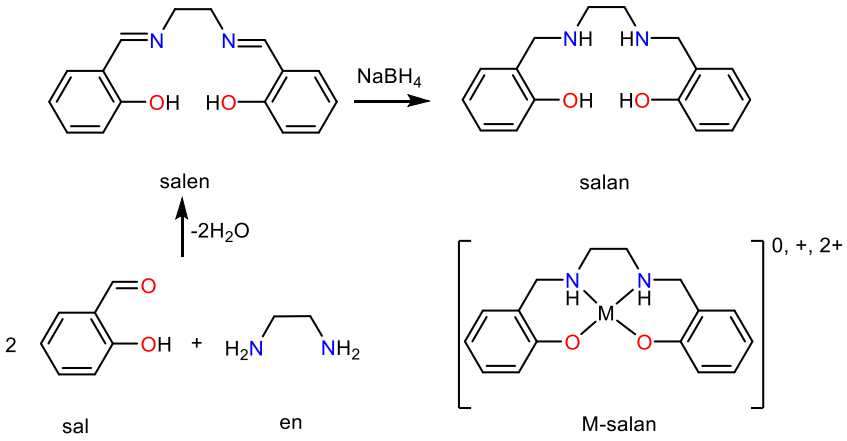

Figure 1.1. The typical synthetic procedure for salen and salan ligands and a metallo-salan complex.

1.1. Ligand design

The design of a ligand is vital for developing its coordination chemistry. The ligand can coordinate to metal centres differently; these include terminal, monodentate, chelating

to one metal centre or bridging bi- or tridentate to two metal centres (Figure 1.1.1). Also, it can form infinite architectures ranging from one to three dimensions. Complexes built from ligands with multiple heteroatoms are more stable than those built from a monodentate ligand.[16] The synthesis of a 3d complex necessitates the design of a polyfunctional ligand, as illustrated in Figure 1.1.2.

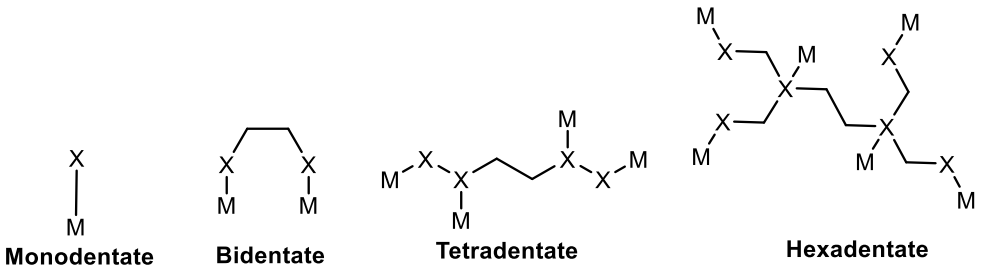

Figure 1.1.1. Examples of coordinating modes of ligands X= donor atoms: M = metal ions.

Most ligands are designed with preferences in geometry for specific pocket sizes for certain metal ions with ionic radii, oxidation state and valencies.[17] Sunadal[18] *et al.* reported a super silyl monodentate ligand (Figure 1.1.2, a) capable of stabilizing four-coordinated Mn^{2+} complexes for various applications, including catalysis[19] and biomedicine.[20] Hua[21] *et al.* reported a series of monodentate phosphoramidite ligands and demonstrated its high enantioselectivity in asymmetric catalytic transformations of cyclo-alkenones. Ferhan[22] *et al.* used bidentate ligands (Figure 1.1.2, b) to synthesise the corresponding Cu^{2+} complexes and investigated their antimicrobial activity towards *E. coli, B. cereus, B. subtilis and S. Aureus*. The corresponding binary Ni^{2+} complex from the same bidentate ligand was prepared as a precursor in a catalytic-polymerization reaction.[23] Gao[24] *et al.* demonstrated the catalytic applications of a Zn^{2+} complex from an asymmetric N, N, O-tridentate ligand in a Lactide polymerization reaction (Figure 1.1.2, c). Kuwabara[25] *et al.* reported Luminescent Ir^{3+} complexes containing benzothiazole-based tridentate ligands (Figure 1.1.2, d) These Ir^{3+} complexes have higher quantum yields and thermal stability than Ir^{3+} complexes built from bidentate ligands. They can be used as an efficient emissive dopant in organic light-emitting diodes. Anwar[26] *et al.* reported a family of Cu^{2+} complexes with tridentate donor ligands containing (N, O, S), (N, N, N), (N, N, S) or (S, S, S) heteroatoms. This study concluded that the ligand framework's flexibility and stereo electronics could be tuned systematically. Ratnam[27] *et al.* reported a new family of palladium complexes derived

from tridentate ligands, which were found to catalyse the Suzuki-Miyaura cross-coupling reaction. Complexes synthesised with tridentate ligand have found applications as catalysts,[28] corrosion inhibitors,[29] in quantum dots and in vivo imaging[30] and biomedicine.[20]

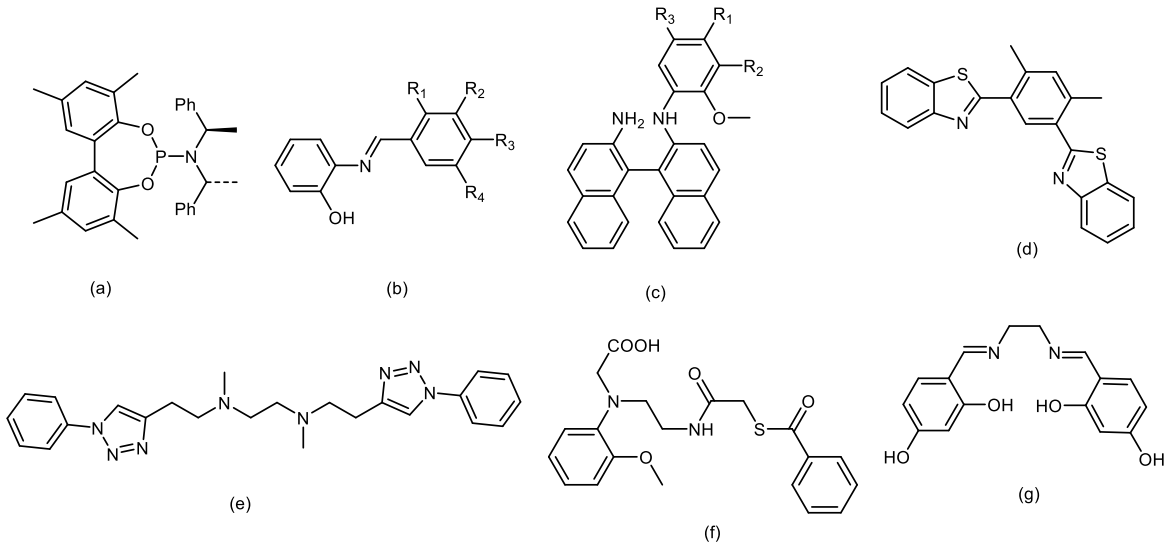

Figure 1.1.2. Illustrations of different ligands

Polydentate ligands with less steric effects and a higher number of donor atoms tend to form more stable complexes than monodentate ligands.[31] Specifically, tetradentate ligands bearing a pocket size suitable for transition metal ions tend to form stable complexes. Wang *et al*. [32] reported a series of tetradentate ligands (Figure 1.1.2, e) built using click chemistry and demonstrated the applicability of the corresponding complexes in organometallic chemistry. Fourteau[33] *et al.* reported a new class of N_2S_2 tetradentate ligands (Figure 1.1.2, f) and proposed their suitability for medicinal applications. The Cu^{2+} and Ni^{2+} complexes of a different tetradentate ligand (Figure 1.1.2, g) can sense hydrazine with high selectivity and specificity.[34] Pui *et al* reported a tetradentate ligand and its corresponding Pd^{2+} complex, which exhibited good performance for photocatalysis and green phosphorescence.[35] All the above studies demonstrate the polydentate ligand's versatility and their corresponding complexes' varied applications.

Several works report the design of salen ligands.[1,36–39] However, the stability of these ligands and their corresponding complexes are trivial; they are susceptible to hydrolysis or dehydrogenation depending on the nature of the solvents.[40] Reductive

amination of a salen ligand provides the corresponding salan ligands. The latter and their corresponding complexes have better stability in aqueous media. Very few reports support the stability of salan complexes over salen complexes in organic and non-organic solvents; Arnd[41] *et al.* investigated the higher stability of the salans complexes of Co^{2+}, Ni^{2+} and Cu^{2+} and their catalytic performance in different organic solvents. The Cu^{2+} and Ni^{2+} complexes from corresponding salen and salan ligands were reported by Isabel[42] *et al.* These compounds were characterised by potentiometry, UV-Vis spectroscopy and EPR and the Cu^{2+} salan complex showed high stability of about 95% even at varied pH 2 compared to the corresponding Cu^{2+} salen complex. A similar observation was noted for the Ni^{2+} complex.

1.2. Complex design

1.2.1. Development of complex

Complexes are molecular entities possessing one or more metal centre (s) bound to one ligand and/or co-ligands. It is a product of the Lewis acid-base reaction; the ligand is the Lewis base with lone pairs of an electron, while the Lewis acid is the transition metal.[43] The ligands are usually neutral or anionic molecules that possess heteroatoms with lone pairs of electrons to covalently bond to the metal(s). The ligands can be monodentate or polydentate molecules, which means organic scaffolds possessing two or more heteroatoms with lone pairs of electrons, as explicitly discussed in chapter 1.1. The metal centre is an acceptor for the lone pairs of electrons; thus, covalent bond(s) is(are) formed.[44,45] The metal centre adopts different geometries; this notion is governed by the number of heteroatoms present in the primary ligand and the presence, if any, of other co-ligands. For sala(e)n 3d complexes, the most common coordinating numbers are 4, 5 or 6 (Figure 1.2.1); however, different geometries can be achieved, including pentagonal bipyramid, square antiprism and tricapped trigonal prism. In assessing the bond strength between the ligand acting as the donor group and the metal ion as the acceptor, it is essential to consider Pearson's acid-base concept (HSAB theory),[46] this concept is based on the premise that strong acids bind favourably and strongly to a strong base. In contrast, soft acids bind favourably to soft bases.[47] A table showing the selection of acid and bases classified using Pearson's HSAB principle are shown below.

Table 0.1 Lewis acids and bases as classified with Pearson HSAB principle

Hard Acids	**Soft Acids**	**Borderline**
Li^+, Ca^{2+}, Na^+, K^+, Fe^{3+}, Co^{3+}, As^{3+}, Mg^{2+}, H^+, Mn^{2+}, Cr^{3+}, Mg^{2+}, Al^{3+}, Sn^{2+}	Cu^+, Ag^+, Au^+, Pt^{2+}, Hg^+, Cs^+, Hg^{2+}, Br^+, Pd^{2+}, Hg_2^{2+}, Cd^{2+}	Fe^{2+}, Co^{2+}, Ni^{2+}, Cu^{2+}, Zn^{2+}, Pb^{2+}, SO_2, NO^+, $B(CH_3)_3$
Hard Base	**Soft Base**	**Borderline**
NH_3, Cl^-, NO_3^-, OH^-, F^-, SO_4^{2-}, H_20, PO_4^{3-}, ROH, RNH_2	R_2S, C_2H_4, Co, RNC, SCN, R_3P, CN^-, I^-, RS^-	$C_6H_5NH_2$, C_5H_5N, BR^-, N_3^-, NO_2^-, SO_3^{2-}

This binding leads to different metal complexes with varied applications depending on their purpose; although the HSAB Pearson concept guides the design of coordination compounds, beyond these, there are principles that metal centres and heteroatoms obey; the following criteria should be considered.

- metal centre; its oxidation state and ionic radii,
- organic ligand; number and type of heteroatoms,
- coordination geometry: if the property of interest requires ligand/substrate exchange, then the ligand should partially fulfil the coordination geometry of the metal centre
- operational stability in coordinating/non-coordinating solvents, low or high temperatures, physiological or different pH values, dissociation etc…

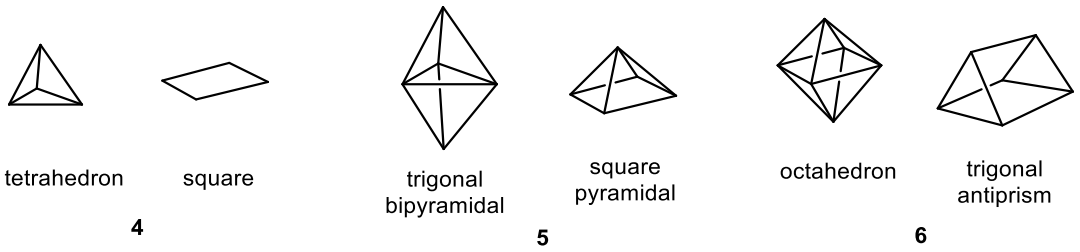

Figure 1.2.1. The most common geometries for coordination are numbers 4, 5 and 6.

A milestone in the history of complexes was achieved with the discovery of *cis*-platin in 1960 by Barnett Rosenberg.[48] *Cis*-platin is a Pt chemotherapeutic compound that is active against squamous cell carcinoma, carcinomatosis, and germinal cell tumours in dogs.[49] Notably its trans-isomer, *trans*-platin, is clinically ineffective against

cancer.[50] Ever since, the design of complexes has taken centre stage and found applications, which include cancer therapy,[48] sensing[51] and detection, biological and analytical applications,[52] fluorescent cell imaging[53] and catalysis.[11,54]

1.2.2. Complex stability constants

The stability of the complex is determined by the Logβ value, which measures the strength of interaction between metal-ligand in solution[55] and is given in the equations.[56]

$$\text{Metal + Ligand} \rightleftharpoons \text{Metal – Ligand} \qquad K_1 = (ML)/(M)(L) \qquad (1)$$

$$\text{Metal + Ligand}_2 \rightleftharpoons \text{Metal – Ligand}_2 \qquad K_2 = (ML_2)/(M)(L) \qquad (2)$$

$$\text{Metal + Ligand}_3 \rightleftharpoons \text{Metal – Ligand}_3 \qquad K_3 = (ML_3)/(ML_2)(L) \qquad (3)$$

Thus,

$$\text{Metal + Ligand}_{n-1} + \text{L} \rightleftharpoons \text{Metal – Ligand}_{n} \qquad K_n = (ML_n)/(ML_{n-1})(L) \qquad (4)$$

where K_1, K_2, K_3……K_n are all equilibrium constants and are known as overall stability constants.

The stability constant, known as well as formation or binding constant, can be determined using several methods, including potentiometry,[57,58] ion exchange,[59,60] distribution,[61] solubility,[62] polarography[63,64] and electrometric techniques.[65]

1.3. Geometric arrangements of ligand design and properties specific to its application

Different geometrical designs, configurations and fine-tuning of ligands have resulted in complexes with various purposes specific to intended applications. The shape and final adopted conformation of the ligand impact its stereochemistry which in turn restraints the geometry of the metal centre,[66,67] affecting its electronic properties.[68] Steric effects can restrict bond rotation and decrease ligand's flexibility, thus affecting

its conformational preferences and potentially the geometry of the final complex.[69] Stereochemical factors in ligands significantly affect the geometric shape that donor atoms can adopt and conform around a transition metal centre. Geometric constraints of the metal centre must also be considered during ligand design and developments specific to a specific application.[70] Ligands with aliphatic backbones tend to favour a variety of coordination geometries with different transition metals. In contrast, ligands with rather a rigid backbone promote a limited and specific binding mode with transition metal ions leading to limited coordination geometries.[71] On the other hand, the preferred geometry and configurations of transition metal ions when forming complexes with ligands depend on the number of ligands bonded to metal centres, ligand pocket sizes, transition metal charges and sizes.[72,73]

1.4. Spectroscopic methods for monitoring complexes

1.4.1. Fluorescence

Fluorescence spectroscopy is an analytical method that has gained wide acceptance owing to its high sensitivity,[74] specificities,[75] and selectivity.[76] When a molecule (typically fluorophore) absorbs energy in the form of light, an electron is promoted to the excited state (this may be either a singlet state or triplet excited state); the excited electrons can lose their energies in the following ways

(a) The molecule can dissipate its energy by direct collision with its neighbouring absorbing species in a non-radioactive way through energy transfer.

(b) If the excited triplet state overlaps with the excited singlet state, the molecule can cross over to the excited triplet state; this phenomenon is known as inter-system crossing, and on returning to the ground state after emitting light energy where ($T_1 \rightarrow S_0$) this process is known as phosphorescence.

(c) The molecule can partially dissipate energy by undergoing conformational changes and relaxing at the lowest vibrational excited energy level, this is called vibrational relaxation, and on returning to the ground state, it emits energy in the form of light ($S_1 \rightarrow S_0$), and this process is called fluorescence.[74]

These processes are explained in the Jablonski diagram, as shown in Figure 1.4.1.

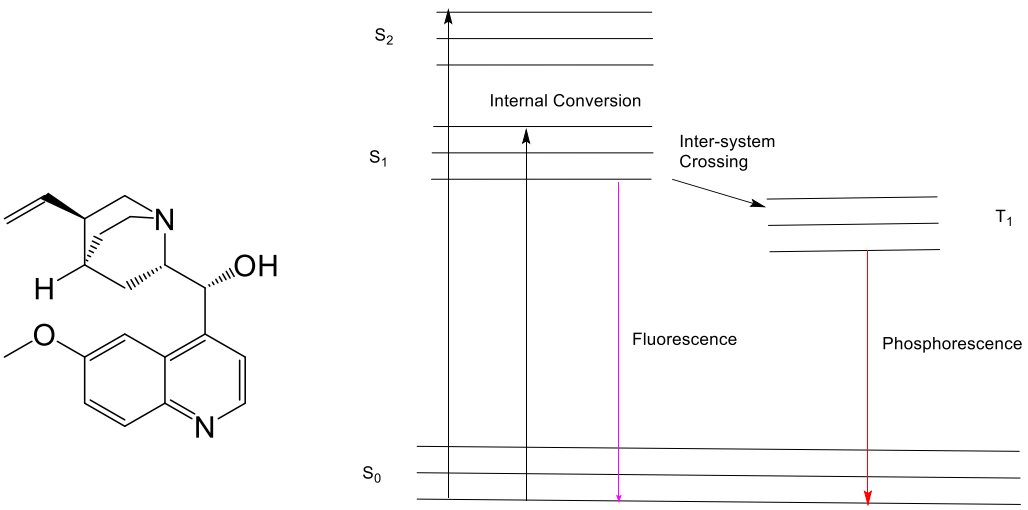

Figure 1.4.1. (left) The quinine molecule. (right) The Jablonski diagram.

In principle, polyaromatic-based compounds are excited from an energy source at a particular wavelength and emit light during relaxation at a longer wavelength is measured. The emitted energy of florescent photons in its ground state is always less than that of the excited photons, this is because energy is usually lost through vibrational relaxation and internal conversion, a typical fluorescence lifetime is in the region of 10 ns since the emission rates of fluorescence are typically 108 s^{-1}. A typical example of a fluorophore is quinine (Figure 1.4.1.), initially observed by Sir John Frederick William Herschel in 1845.[77] This compound, which is always present in tonic water, glows a faint blue colour by exposure to sunlight. Quinine is excited through ultra-violet light (sun) and, upon returning to its ground state, emits a blue light in the form of a photon with a wavelength in the region of 430-450nm. Naphthalene-based fluorophores have been extensively and efficiently used in supramolecular chemistry, organic optoelectronics, biochemistry, and biological and environmental studies.[78–81].

1.4.2. ^{19}F-NMR spectroscopy

The fluorine atom has a small size and single valency forms strong covalent bonds and is electronegative. The presence of fluorine atoms in biological molecules is rare[82,83] and only a few fluorinated biological compounds are known.[84,85] The NMR principles for the nucleus (^{1}H,^{13}C, ^{31}P, ^{15}N) are the same for the ^{19}F nuclei; however, no signal overlap or interferences in background signals can be identified. This lack of background signals identifies ^{19}F-NMR spectroscopy as an ideal technique for monitoring purposes.[86] For

example, the interaction of amino acids, glycols, and chiral amines with fluorinated analytes will be visible when a shift from the original fingerprint peak region is observed. For a nucleus to possess an overall spin, the number of neutrons plus the number of protons must be odd; this will give the nucleus a half-integer spin (i.e. 1/2, 3/2, 5/2).[87] However, if the number of neutrons and protons are both odd, the nucleus has an integer spin (i.e. 1, 2, 3).

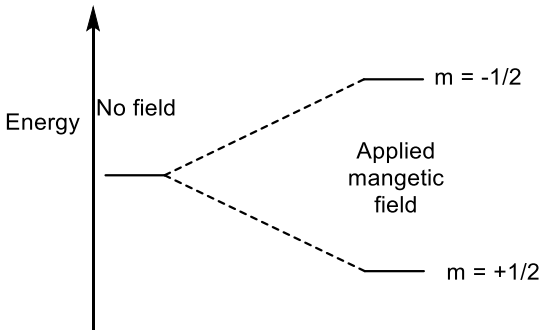

Figure 1.4.2. Energy Levels for a Nucleus with Spin Quantum Number

1.4.3. Circular Dichroism

Circular dichroism (CD) is a spectroscopic method used to differentiate specific molecules interacting differently with right and left circularly polarized light.[88, 89] When a beam of circularly polarized lights, of the same frequency and amplitude, passes through an optically active medium that has an absorption peak in the ultraviolet region, the left-handed and right-handed circular polarized light components contained in the region would have different propagation speeds mainly due to different refractive indexes and intensities, the light absorbed would be circularly polarized, secondary absorbance components will arise from circular dichroism and are measured by switching between right and left circularly polarized light, and the resulting difference is calculated as absorbance. This analytical method illustrates the difference between chiral molecules having non-superimposable mirror images of each other. It is widely used to study changes in the conformations of molecules[90] as well as to elucidate more on the configurations of chiral compounds,[91] thus, it finds applications in conformational studies of protein,[92] glycosides,[93] chiral amines,[94] and nucleic acids. Other techniques can be used to determine the enantiomeric purity of these chiral structures: chemiluminescence,[95] high-performance liquid chromatography (HPLC),[96] capillary electrophoresis,[97] electrochemical methods, etc. Although most of these techniques

help determine enantiomeric purity, they are time-consuming, use expensive and complex equipment, require trained personnel, and on some occasions, differentiation between two enantiomers is challenging.[98]

1.4.4. UV-Vis Spectroscopy

UV-Vis spectroscopy is an analytical technique used to characterise and evaluate different types of substances and solvents.[99] It is widely used since the cost of equipment and its maintenance is low.[100] It finds applications in biomedical studies like cancer,[101]characterization and catalytic studies monitoring [102] antimicrobials and antioxidant monitoring,[103] heavy metals removal and monitoring,[104] nanoparticles determination,[105] and sensing.[106] Its principles are based on the absorption of ultraviolet or visible light by chemical compounds leading to the production of some distinct spectra. It can give quantitative and qualitative information for a compound with a wavelength range from 200nm-800 nm.[107] Its principles are mainly based on the interaction between light and matter. When matter absorbs light, it is excited, and its relaxation to the ground state results in the production of the spectrum. The energy difference between the excited and ground states equals the energy absorbed by the absorbing species as defined by the Beer-Lambert Law. The absorbance of a solution is directly proportional to the concentration of the absorbing species in the solution and path length, as presented in the equation below.

$$A = \varepsilon bc \quad (5)$$

where A is absorbance (unitless, usually seen as arb. units or arbitrary units), ε is the molar absorptivity of the compound or molecule in solution ($M^{-1}cm^{-1}$), *b* is the path length of the cuvette or sample holder (usually 1 cm), and *c* is the concentration of the solution (M).

1.5. Heavy metals pollutants (HMPs)

Water polluted with heavy metals is a growing global concern due to its adverse effects on the environment and human health.[108] The overabundance of heavy metals

pollutants (HMPs) originates from scientific and technological advances, resulting in industrialization and unplanned urbanization.[109] These contaminate and pose adverse effects on our environment.[110] HMPs are released into the environment through natural and anthropogenic activities.[111,108,112] Most HMPs like Hg^{2+}, Ni^{2+}, Cd^{2+}, Pb^{2+}, As^{+}, Cr^{3+}[113] originate from less of a natural phenomenon but mostly from various anthropogenic activities. The chief sources of natural HMPs in the environment are from rocks (sedimentary, metamorphic, and igneous rocks); through leaching, erosion, weathering, soil formation etc. HMPs are distributed into the environment through groundwater (streams, springs, lakes, and rivers) for a considerable distance, and their composition varies from location to location. Other features defining HMPs concentration are chemical, biological and physical activities such as dilution and evaporation, redox potential, pH, temperature and living organisms.[108] HMPs carried by water can be absorbed by oxyhydroxides or aquatic organisms like algae which then introduce them to the food chain. HMPs quickly accumulate in living organisms through various processes like the food chains,[114] various industrial activities[115] like mining of metals, leaching of metals from different sources such as landfills, applications of land fertilizers,[116] incineration and internal combustion engines etc. World Health Organization sets a certain HMPs threshold standard concentration; when they are in excess cause severe adverse health defects like cancer, liver damage, renal failure, oxidative stress, and brain damage.[117]

HMPs detection with analytical methods has been used to alleviate environmental issues, contribute to knowledge in biomedical studies,[118] tackle global security concerns and make our environment green. Over the last few decades, different types of conventional analytical methods were employed in the detection of HMPs. They include Inductively coupled plasma mass spectroscopy (ICP-MS), atomic absorption spectroscopy (AAS), capillary electrophoreses (CE), UV-Vis spectroscopy, anodic stripping voltammetry (ASV), x-ray fluorescent spectroscopy (XFS), Inductively coupled plasma optical emission spectroscopy(ICP-OES) etc.[119] These methods detect and sense HMPs even at low concentrations, but have limitations like (a) expensive instrumentation,[120] (b) lack of trained and experienced personnel to operate the instruments, (c) ambiguous sample preparations and clean up (d) not used for on-field detection and monitoring of HMPs. To address these limitations, scientists develop less expensive, time-saving techniques,[121] portable and highly sensitive[122] sensors to quickly detect HMPs. These

new techniques are chemical and optical sensors, biosensors, electrochemical sensors, molecular sensors etc.

1.5.1. Copper

Copper (Cu) is a transition element belonging to group 1B with atomic number 29. It exists in +2, +1 and 0 (pure metal) oxidation states,[123,124] and is essential for living organisms participating in many catalytic activities associated with physiologically important enzymes.[125] It is disposed of as an industrial effluent into aqueous environments and enters bioaccumulation from the food chain. Its median intake in the united state is 1.0 to 1.6 mg/day for adult men and women.[108] Concentrations over this dose can cause severe health problems, including neurodegenerative disorders leading to Parkinson's or Alzheimer's disease[126] and hypoglycaemia. [125] Copper toxicity can also restrict the self-purification of seas, rivers and oceans by bacteria[127], thereby reducing the bacteria's biological functioning activities. Therefore, it is imperative to develop techniques to monitor copper imbalance in the land, water, and air.

1.5.2. Lead

Lead (Pb) is a soft, silvery-white transition metal with atomic number 82 and belongs to group 14 (IVa). It is known from ancient times with no known biological importance.[128] And yet very persistent in the environment,[129] non-biodegradable and extremely toxic[130] even at very low concentrations to both biological systems and humans.[131] It exists in both +4 and +2 oxidation states and has a low melting point. It was used in ancient times for building materials, pigments for glazing ceramics and water pipes. However, recently it has been extensively used in forming alloys with Sn[132] and batteries.[133,134] These recent uses resulted in extensive disposal of Pb in aqueous media; its excess can lead to severe health defects in the central nervous system,[135] the reproductive system and functions of the brain cells.[46,136]

1.5.3. Cadmium

Cadmium (Cd), with atomic number 48, is a transition element which belongs with Zinc and Mercury in Group IIb of the periodic table.[137] Cadmium usually exists in +2

oxidation; however, a few reports indicate that Cadmium also exists in the +1 oxidation state.[138] Friedrich Stromeyer discovered Cd in 1817 as a constituent of smithsonite ($ZnCO_3$) in zinc ore.[139] The main pathway Cadmium enters into the environment is via industrial waste processes, including electroplating, textile operations and refining, pigments, plastics, fertilizers, smelting, alloy manufacturing, cadmium-nickel batteries, mining, pigments and dyes.[140] Cadmium contamination from these various sources has become a serious threat to the environment and public health risk, including cancer,[141] skeletal systems,[142] renal, nervous and reproductive systems. Thus, the development of methods to purify and detect Cd in contaminated water and effluents is a major area of active research.[143]

1.6. Sensing principles

The definition and understanding of sensors are mostly field-dependent.[144] The idea and motive behind creating sensors in materials, chemistry, biochemistry, and physics, is to abandon expensive and complex instrumentation methods and replace them with inexpensive systems that anyone can operate. A classic example of successful sensors is the pregnancy test and glucose meter, which has touched many societies. Research is limited to both biological and chemical sensors. Broadly, biological sensors, often called molecular probes, tend to create future systems that identify important biological compounds and health risks and detect the presence of both desirable and undesirable compounds in a system.

1.6.1. Zn^{2+} complexes as sensing probes

Zinc is the second most abundant trace element in the human body,[145] characterized by filled $3d^{10}$ orbital and classified as a hard to borderline electron pair acceptor.[146] Zn^{2+} complexes are less toxic compared to other transition metal complexes. They have played an essential role in molecular recognition,[147] catalysis,[148] biological imaging applications,[149] anticancer agents,[145] and therapeutic applications.[150] The most common geometries for Zn^{2+} complexes are tetrahedral and octahedral with tetradentate ligands, but pentagonal bipyramid geometries are also possible.[151] Chiral Zn-porphyrin dimers have been previously reported as potential sensors for amino acid

derivatives;[152], these complexes showed good sensing and discrimination ability towards two enantiomers and their absolute configurations. Li *et al* demonstrated that chiral Zn^{2+} complexes could be selectively used as a fluorescent sensor to sense and distinguish cysteine and histidine from other naturally occurring amino acids in an aqueous solution. [153] To demonstrate the versatility of chiral Zn^{2+} complexes, Sano[154] *et al* had also reported the usefulness of Zn^{2+} complexes as fluorescent probes for varieties of medical studies.

1.6.2. Chiral amine sensing

Chiral compounds were first discovered by Louis Pasteur in 1848 when he successfully separated by hand sodium ammonium tartrate into its isomers.[155] Chiral compounds, due to their dexterity has found applications in forensic studies, [156] pharmaceutical applications, [157] catalysis[158] and sensing applications.[82,159] Two enantiomers have the same physical properties but may possess different pharmacological and biological activities.[160] Conventional high-performance liquid chromatography (HPLC) can separate the enantiomers,[161] but this approach involves costly chiral columns. Thus, developing new methods for enantiomeric discrimination is highly interesting for industrial and biomedical applications and is subsequently vital for future discoveries.[162] For example, circular dichroism (CD) and fluorescence,[163–170] monitor absorbance intensity change(s) whereas Nuclear Magnetic Resonance (NMR) proceeds chemically shifted signals;[171–174] these methods rely on host-guest interaction(s), therefore thermodynamic, kinetic parameters and equipment's response time signify method applicability and limitation. In the latter case, methods incorporating chiral templates and ^{1}H-NMR are popular,[175–180] however lately, emphasis is given to developing hetero nuclear-based methods i.e. ^{31}P[173,181] or ^{19}F.[84,182,183]The latter method has the following two advantages: lack of background interference;[182,183] thus applies to large molecules, such as proteins,[84,184] and a broad detection window from -200ppm to +200 ppm depending on the antenna, i.e -CF_3, -OCF_3, -F and so on.[82] Pioneer works from Swager[185,186] and Song[187] establish the principles in using new or modifying already known chiral fluorine-based complexes for discriminating chiral amine based methods (Figure 1.6.2.1). Both methods work in non-coordinating solvents and rely on the host-guest interaction principle; thus, two different peaks appear in the ^{19}F NMR spectrum.

In the latter case, the methods also apply coordinate solvents, and its operational window is 0.21 ppm.

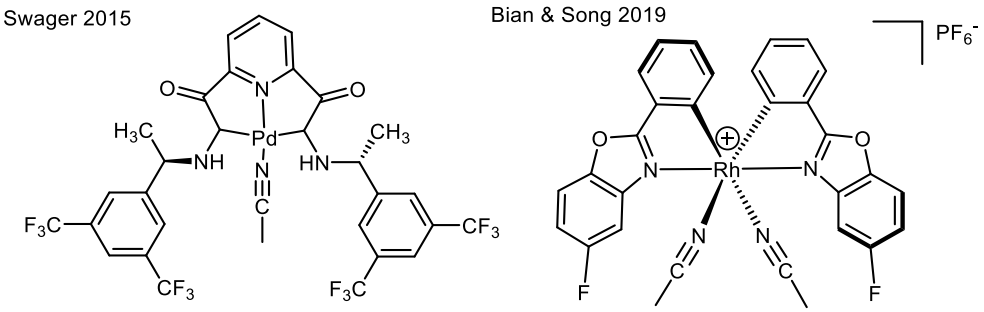

Figure 1.6.2.1. Known complexes used for amine sensing with ^{19}F NMR.

1.6.3. Novel Asymmetric salan fluorescent selective Cu^{2+} sensors.

Recently, there has been a renewed interest in developing fast, sensitive and selective probes for detecting HMPs, including Cu^{2+}. Copper is essential to human health,[188,189] it functions as a necessary co-factor for enzymes due to its redox-active Cu^{+}/Cu^{2+} conversions.[190] However, excess and unregulated copper is very toxic to the human body as it can cause homeostasis, which will lead to severe neurodegenerative diseases like Parkinson's and Alzheimer's disease.[191]

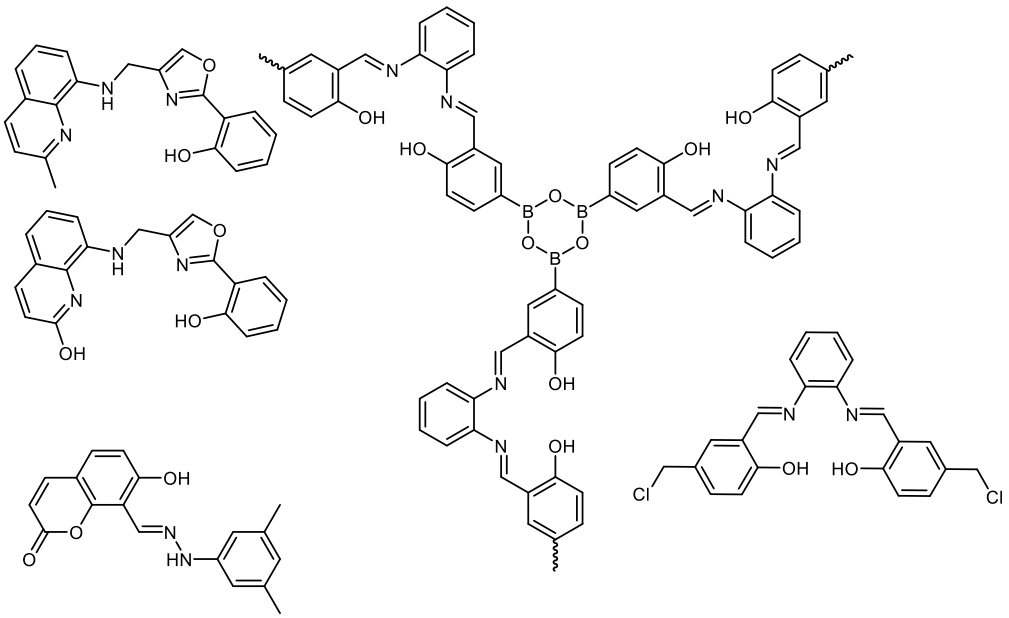

Figure 1.6.3.1. Selected ligands used for sensing Cu^{2+}.

Recent reports suggest that Cu^{2+} is responsible for damaging an infant's liver.[192] Cu is also reported to promote and generate reactive oxygen species (ROS)[193], which cause damage to cell structures[194] and interferes with cellular signalling, inducing apoptosis.[195,196] Copper contamination and its toxic effects on humans continue to pose severe global problems. Hence, its sensing and detection become imperative. They are many reported methods for the detection and sensing of Cu^{2+} ions, which include inductively coupled plasma spectroscopy,[197] atomic absorption spectroscopy,[198] inductively coupled plasma atomic emission spectroscopy (ICP-AES),[199] and electrochemistry.[200]

1.6.4. Heavy metals sensing

HMPs are present at higher than normal and unacceptable levels in aqueous media,[115] due to a faster rate of industrialization and human's quest for a better life. Various methods have been proposed to capture and remove HMPs from aqueous media to overcome this obstacle.[201] These technologies include but are not limited to using porous materials such as Metal-Organic Frameworks (MOFs),[108,202,203] zeolites,[204–206] hydrogels[207,208] sulphur-based nanosheets[209] or silica-based components as the absorbents.[210,211] And the detection methods include atomic absorption spectroscopy (AAS), capillary electrophoreses (CE), UV-Vis spectroscopy, anodic stripping voltammetry (ASV), X-ray fluorescent spectroscopy (XFS), inductively coupled plasma optical emission spectroscopy (ICP-OES)[119] etc. These conventional methods are often characterized by many drawbacks like ambiguity, expensive instrumentation, unsuitable for on-field detection, lack of trained and experienced personnel for operation, lack of selectivity, and time-consuming lab procedures for its preparation.[212] etc. Currently, methods incorporating MOFs as absorbents dominate present-day studies; however, developing an efficient, convenient, selective and practical capture technology in which the capturing mechanism is well understood remains a big challenge.

1.6.5. Neurotransmitters

Studies of the complex functions and understanding of the brain are leading challenges in biomedical research and are now gaining momentum. Neurotransmitters

(NTs, Figure 1.6.5.) are essential chemical messengers that transmit information between the nerve cells,[213] muscles functions and behaviour,[214] organs, and other tissues.[215] NTs are known according to their chemical structures and divided into several groups, including amino acids,[216] biogenic amines, and soluble gaseous transmitters such as nitric oxide, hydrogen sulphide, and peptides.[215,217]

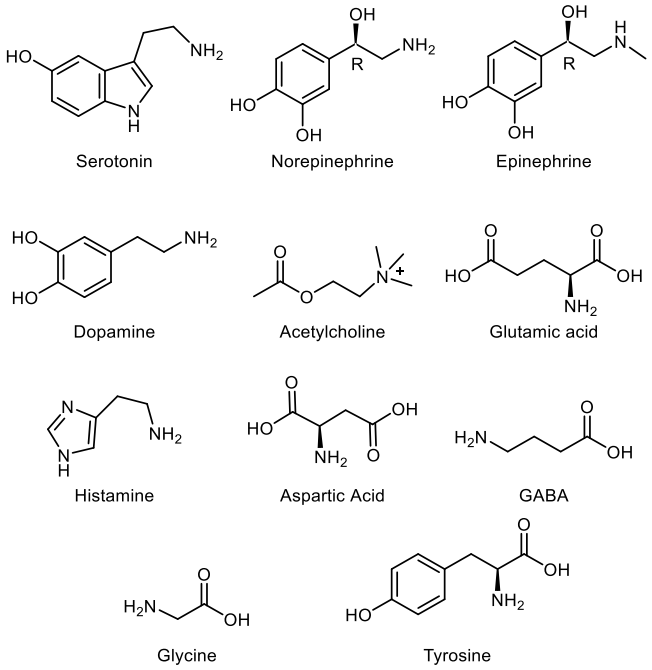

Figure 1.6.5.1. Some known neurotransmitters (NTs).

NTs, control and regulate various body functions, including heartbeat, breathing, behaviour and conjunction, muscle control, digestion, neurological functions, and sensory response.[216] NTs are classified as essential chemicals in human health due to their vast functions; any imbalance in their activities can cause severe disease and mental disorders like Alzheimer's disease, bipolar disorders,[218] schizophrenia,[219] Parkinson's disease, etc. Several factors, such as stress, genetic factors, toxic chemicals, and poor diet,[215] can trigger these imbalances; as such, monitoring the level of NTs in the human body is vital for clinical analysis and medical treatments.[220] Several studies reveal that a single neuron produces different types of NTs,[218] and several methods exist to detect them. The known analytical techniques that can detect NTs include liquid chromatography (LC),[221] microelectrodes, capillary electro-chromatography coupled with UV detection, capillary electrophoresis (CE), electrochemical detection,[222] microdialyses, fast-scan cyclic voltammeter(FSCV),[213] mass spectrophotometer and fluorescence detection.

1.7. Aim of this thesis

The Niger Delta aqueous media region has witnessed contamination over the years, significantly imminently affecting daily livelihood and sustenance,[223,224] and ultimately human security, recreation and fisheries, thus imposing water quality regulations and monitoring methods.[225] Mercury, Lead, Arsenic, Cadmium and Chromium are the contaminants according to the World Health Organization standards.[226] To overcome this obstacle, various methods have been proposed to capture and remove pollutants from aqueous media.[201] These technologies include but are not limited to using porous materials such as Metal-Organic Frameworks (MOFs),[108,202,203] zeolites,[204–206] hydrogels[207,208] sulphur-based nanosheets[209] or silica-based components as the absorbents.[210,211] However, developing an efficient, convenient, selective and practical capture technology in which the capturing mechanism is well understood remains a big challenge.

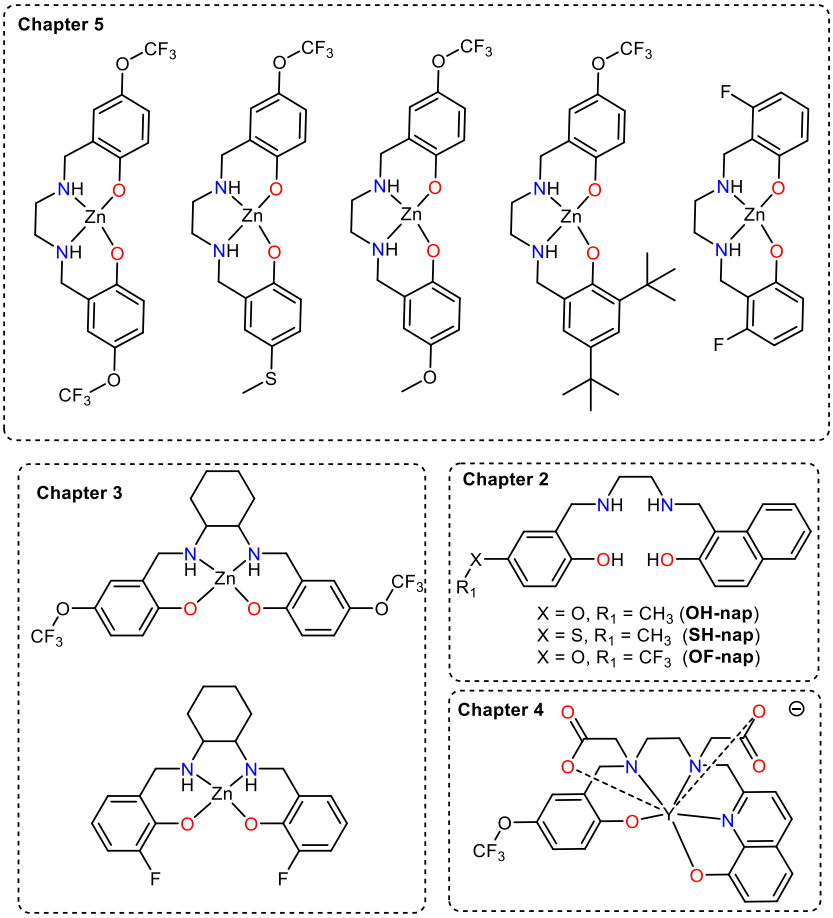

Figure 1.7.1. The molecular entities used in this study.

Salan ligands are easily accessible and modifiable and offer a specific pocket size for coordination; thus, their complexes have inevitably found applications in catalysis, sensing, and medicinal chemistry.[42,227,236–243,228–235] The Kostakis group has recently reported a convenient protocol for asymmetric N_2O_2 salans.[36] This method gives access to numerous ligands and corresponding complexes with chemically modified peripheries which can be used for structural activity relationship studies (SARS). On the basis that these complexes hold the same formula- structure, then the presence of different functional groups becomes a valuable tool and permits chemical mapping of the interaction(s) between the complex and the environment (solvent, analyte, substrates etc) with various techniques such as NMR, IR, UV-Vis, Fluorescence, thus these SARS can extrapolate useful information and underpin mechanisms.

The research activity of this thesis divides into four parts. Salans are well-established tetradentate ligands systems offering a particular pocket to host metals of specific ionic radii, especially 3d transition elements; thus, the first part of the research work focuses on and reports the synthesis of three novel fluorescent asymmetric salans and investigates their sensing ability for 3d transition elements. The second research part reports the synthesis and characterisation of six new chiral salan ligands and their corresponding Zn-salan complexes. In terms of application, this chapter investigates the ability of these molecular entities to sense chiral amines with ^{19}F NMR, the third part of this thesis describes the synthesis of a novel asymmetric heptadentate ligand $H_4oct^{(p\text{-}OCF3)}$salox (Figure 1.7.1, chapter 4) which represents an ideal candidate to provide the corresponding Y^{3+} complex as a non-invasive multimodal sensor for GABA detection and monitoring. The interaction of the Y^{3+}-complex and NTs can be simultaneously monitored with ^1H & ^{19}F NMR, fluorescence and UV-Vis spectroscopic methods, thus providing detailed information to establish a reliable mechanistic pathway. The last part reports synthesising and characterising a family of Zn-salan complexes composed of symmetric and asymmetric ligands and investigates their sensing abilities for Cd^{2+} and Pb^{2+} with ^{19}F NMR. We envisage that underpinning the interaction mechanism of these economically viable molecular entities with HMPs will permit the development of efficient technologies to be applied in the Niger Delta aqueous media region.

2. Chapter 2: Asymmetric salan fluorescent selective Cu^{2+} sensors

Abstract. We report on synthesising three novel fluorescent asymmetric salan ligands and exploring their sensing ability towards first-row transition elements. Secondary coordination sphere alterations impose significant changes in fluorescent sensing responsiveness selectively towards Cu^{2+} ions.

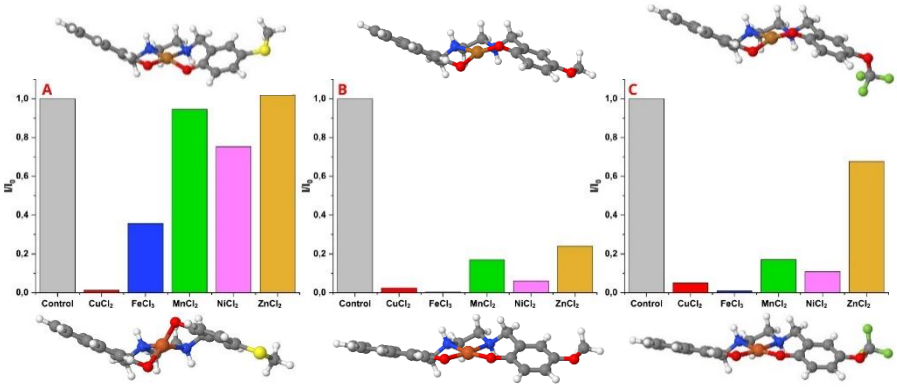

External Contributions: G E. Kostakis performed and evaluated the crystallographic data. D. A. Diamantis, S. D. Katsakos and A. G. Tzakos, performed the systematic fluorescent evaluation. A. Galvácsi and C. Kállay performed solution studies. R. González-Méndez performed and evaluated MS studies. A. Vargas performed theoretical calculations.

2.1. Introduction

Sensors progressively dominate a series of technological applications, mainly focused on the health section, thus, manufacturing smart systems/probes able to simultaneously and/or selectively sense metals, anions, and cations is a research topic that is gaining momentum.[244–246] To develop new smart sensing systems, studying the sensing aptitude of already known or new organic ligands is required. However, establishing a new ligand system is time-consuming, requiring extensive structure reactivity relationship studies to launch the sensing principles and guide future research. Transition elements are essential components of biological systems. Living organisms use them for various processes, including cell signalling, maintaining osmotic pressure, and as cofactors in enzymes.[247,248] In specific, Cu^{2+} is known to affect the self-assembly of amyloid proteins[249,250], generating reactive oxygen species (ROS), and leading to oxidative neuronal damage.[251–253]

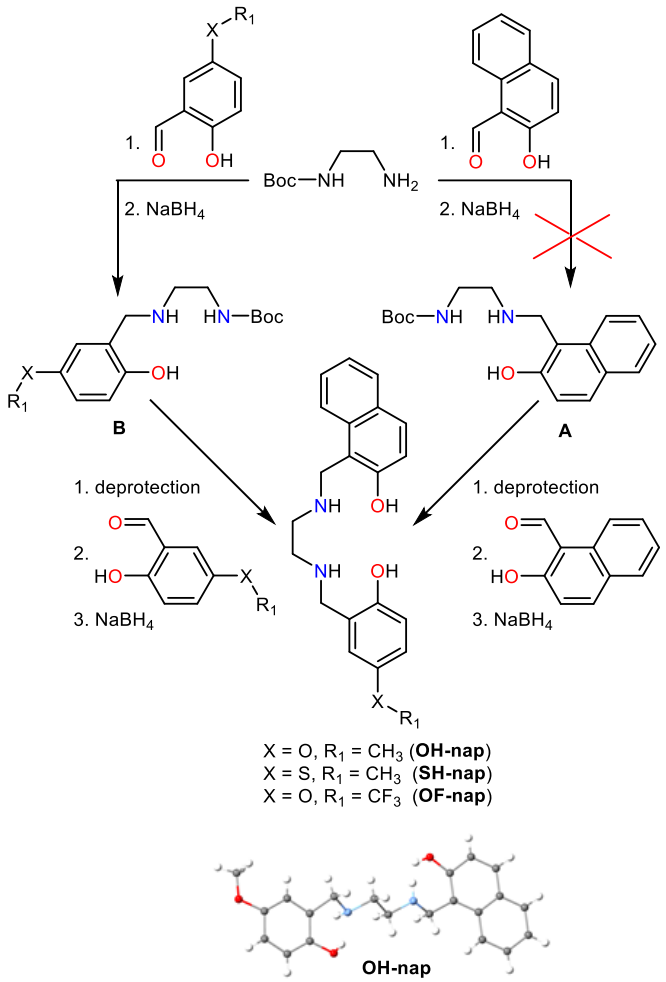

Figure 2.1.1. The five-step synthesis of the chosen asymmetric ligands.

Sala(e)ns are well-established tetradentate (N_2O_2), easy-to-synthesise ligand systems offering a particular pocket to host metals of specific ionic radii, especially 3d transition elements. [149,254–260] Several works examine their naked eye or fluorescent sensing abilities[261,262] At the same time, in terms of stability, these systems are known to be susceptible to hydrolysis (salens) or dehydrogenation (salans).[41,263] We recently established a convenient strategy to design and access asymmetric salans.[36] In our first effort, an asymmetric N_3O salan prevented the redox potential of Cu^{2+} ions which was confirmed by three biological essays.[264] In this work, we hypothesised that retaining the N_2O_2 pocket but introducing into this core a naphtho fluorescent moiety could shape a convenient method to access asymmetric salans (Figure 2.1.1.) that could operate as suitable fluorescent responsive sensors for transition elements. Our choice to alter the heteroatom X and the R= group will impact secondary effects i.e. H-bonding (O vs S), increased lipophilicity (CF_3 vs CH_3), binding (fulfilling or not, the coordination geometry of adjacent moiety), thus allowing us to extrapolate valuable mechanistic evidence. We

envisioned the two-step clockwise route as the more convenient path for precursor A in bulk. However, none of our synthetic efforts was successful, as the reduction step could not proceed. Therefore, we followed the anticlockwise route, synthesising three different precursors **B** before accessing the aimed frameworks. All three ligands were fully characterised with ^{1}H, ^{13}C, ^{19}F NMR, and HRMS, while the crystal structure of **OH-nap** identifies a linear arrangement of the ligand with the hydroxyl groups pointing in opposite directions.

With the ligands in hand and being aware of their poor aqueous solubility, it was necessary to establish the optimum conditions to perform the fluorescent studies. The best solvent for these ligands was a mixture of DMSO/CH_3CN (1:119), and the transition metals were dissolved in double distilled water. Based on the structure of the ligand, the excitation wavelength was set either at 350 nm or 405 nm. Initial fluorescent studies involved ligand incubation with a significant excess of analytes (first-row transition elements Cr, Mn, Fe, Co, Ni, Cu and Zn). We incorporated the weakly binding chloride salts in all studies to avoid the chelation effect (nitrate or acetate).[265] Since the measurements were performed in the open air, we discarded $FeCl_2$ since it is easily susceptible to redox reactions. Based on the literature,[149,254–260] these ligands were anticipated to perform well with transition elements. Indeed, as illustrated in Figure 2.1.2, the fluorescence of all ligands dramatically quenches in the presence of specific transition elements, indicating the *in situ* complex formation. Cu^{2+} and Fe^{3+} samples provide the most intense fluorescent quench.

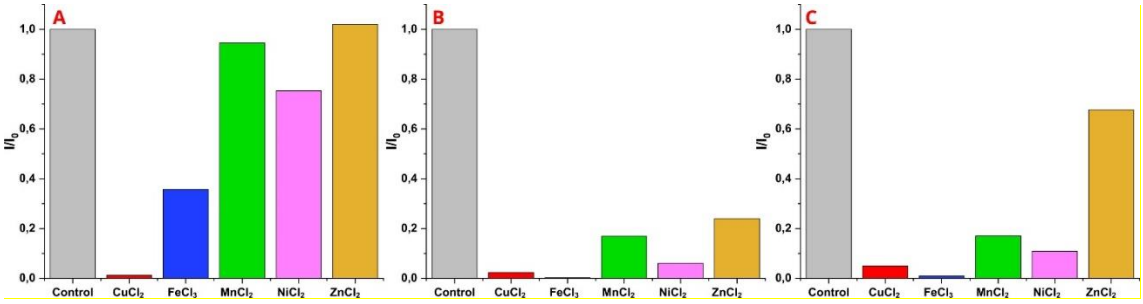

Figure 2.1.2. Normalised fluorescent intensity of the ligands **SH-nap** (A), **OH-nap** (B) and **OF-nap** (C) in excess of different metal ions.

In the next step, we performed fluorescent titration and kinetic studies with Cu^{2+} and Fe^{3+} for the three ligands with substantial structural similarity. The inner core of the organic ligands consists of six atoms possessing sp^3 hybridisation (-CH_2-NH-CH_2-CH_2-NH-

CH_2-), imposing significant flexibility and difficulty in controlling the metal-ligand interaction (Figure 2.3.1. upper). To evaluate the reproducibility of our studies, we recorded three different individual datasets for every ligand, and all showed similar behaviour. As illustrated in Figure 2.1.3, **SH-nap** upon excitation at 405 nm exhibits a broad fluorescence spectrum centered at 575 nm. A distinct decrease of the fluorescence signal was monitored upon the gradual addition of Cu^{2+} and Fe^{3+} (98% and 97%, respectively), accompanied by a ~100 nm blueshift. To determine the interaction between the ligand and these two transition metals, we attempted to apply the Benesi−Hildebrand (B-H) equation (Figures S1-28 & S1-29). Efforts to rationalise a linear behaviour proved ambiguous; however, given the numerous possible ligand configurations and possible metal-ligand interactions, including coordination (Figure 2.3.1. upper), we applied the BH equation in selected data (Figures S1-28) and all data (Figures S1-29) and discarded the use of another fitting model. For the first case, the association constant K_a was evaluated graphically and calculated at 0.384 $x10^4$ and 1.03 $x10^4$ M for Cu^{2+} and Fe^{3+}, respectively (Figures S1-28A &Figures S1-28B). Furthermore, we performed kinetic studies using other equivalents to evaluate the response rate. As illustrated in Figure 2.1.2 (C &D), the detection of Cu^{2+} proceeds faster than Fe^{3+} as a more intense decrease of the fluorescent signal was noticed under the same conditions.

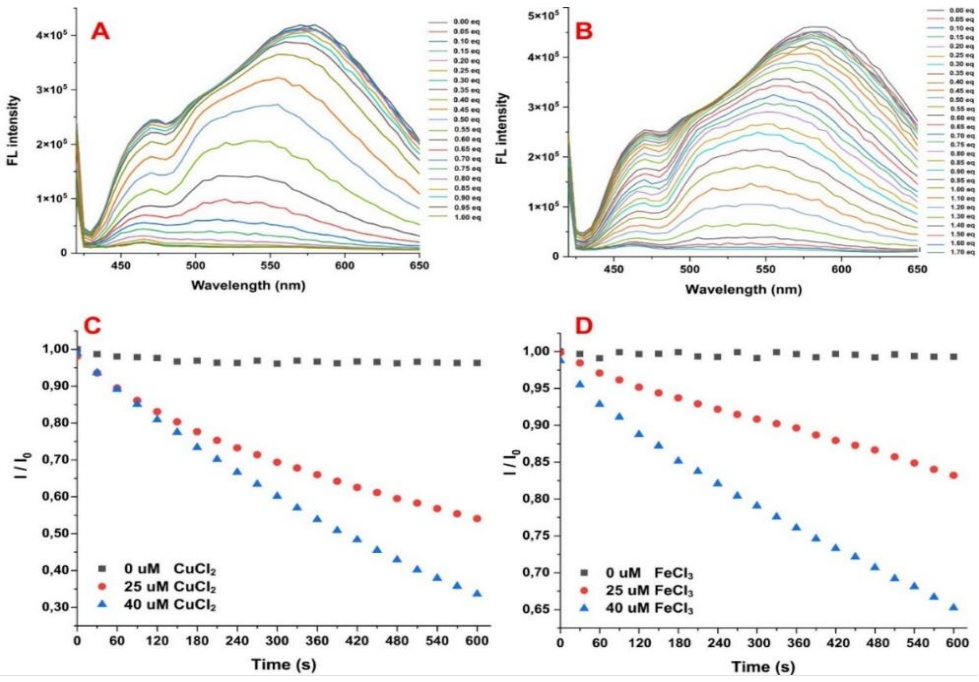

Figure 2.1.3 (A/B) Spectral properties of **SH-nap** (50 µM) in DMSO: ACN (1:119 v/v). (C/D) Time-course alternation of the fluorescent signal at 570 nm of **SH-nap** (50 µM) in DMSO: ACN (1:119 v/v) in the presence of different equivalents of Cu^{2+} and Fe^{3+}.

Then we examined the fluorescent properties of **OH-nap**. As illustrated in Figure 2.1.4, upon excitation at 350 nm, **OH-nap** displays a broad fluorescence spectrum centred at 485 nm. This notable blue shifting in the emission spectrum compared to **SH-nap** could be attributed to the presence of the O-atom instead of the S-atom. Contrary to **SH-nap**, the fluorescent behaviour of **OH-nap** progressively decreases upon the gradual addition of the transition metals, leading to a rare motif until its eventual quenching (83% and 92% decrease, respectively). Concerning the association constants, K_a, the B-H equation extracted them to be equal to $0.278x10^4$ and $3.28x10^5$ M, respectively (Figures S1-28C & Figures S1-28D). Moreover, as illustrated in Figure 2.1.4 (C&D) the response rate of the ligand in the case of Cu^{2+} is highly dependent on the concentration of the metal ion.

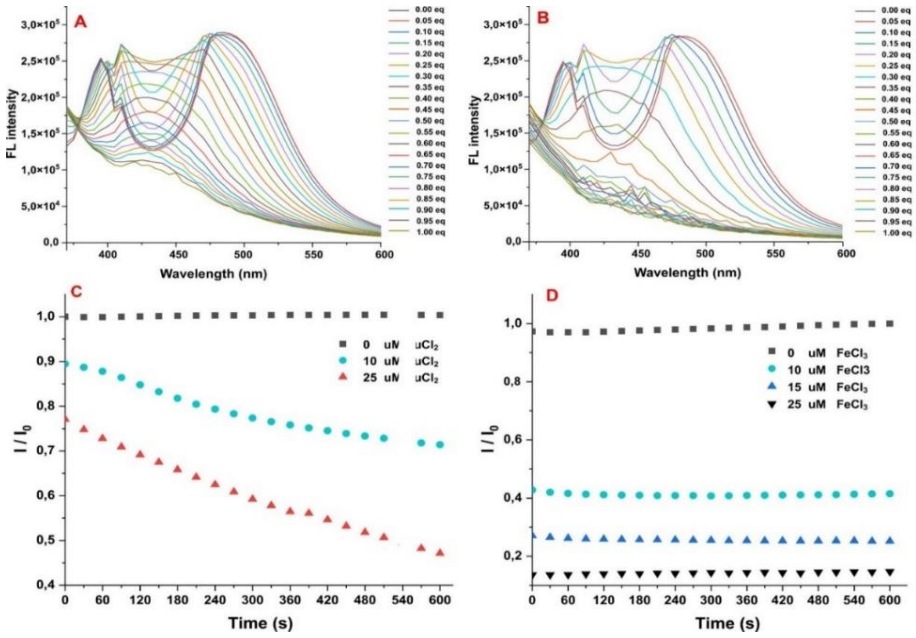

Figure 2.1.4. (A/B) Spectral properties of **OH-nap** (50 µM) in DMSO: ACN (1:119 v/v). (C/D) Time-course alternation of the fluorescent signal at 495 nm of **OH-nap** (50 µM) in DMSO:ACN (1:119 v/v) in the presence of different amounts of Cu^{2+} and Fe^{3+}

OF-nap displays a minor structural difference compared to **OH-nap** (OCH_3 vs OCF_3). However, this modification is vital to the fluorescence behaviour as an electron-withdrawing group replaces an electron-donating group. As illustrated in Figure 2.1.5, it is apparent that **OF-nap**'s fluorescent quenching was more readily achieved than **OH-nap**, independently of the analyte choice. The association constants K_a were calculated to be equal to $0.4772x10^5$ and $0.394x10^5$ M for Cu^{2+} and Fe^{3+}, respectively (Figures S1-28 E& Figures S1-28F). As for the kinetic studies, it is evident, Figure 2.1.5, that fluorescence quenching relies on the concentration of the analyte.

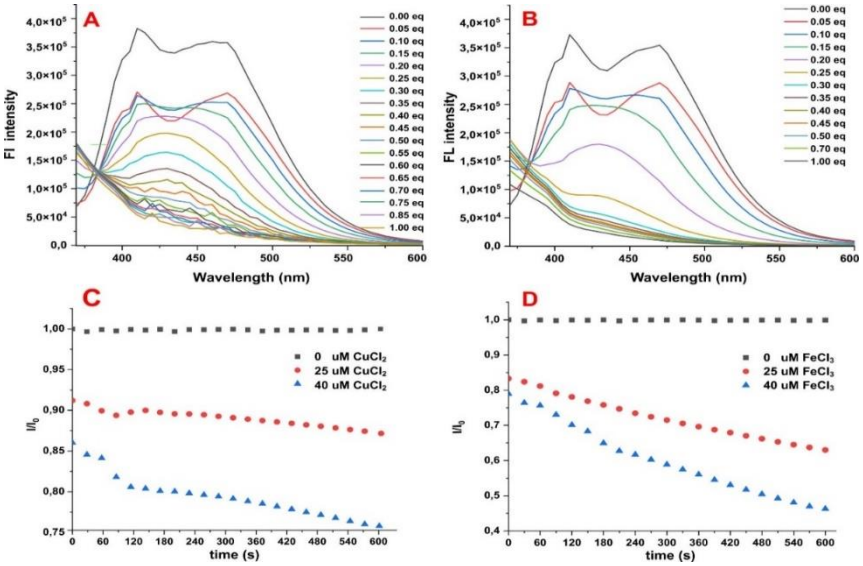

Figure 2.1.5. (A/B) Spectral properties of **OF-nap** (50 µM) in DMSO: ACN (1:119 v/v). (C/D) Time-course alternation of the fluorescent signal at 495 nm of OF-nap (50 µM) in DMSO:ACN (1:119 v/v) in the presence of different amounts of Cu^{2+} and Fe^{3+}.

Lastly, we calculated the limit of detection (LOD) values for both Cu^{2+} and Fe^{3+} for the three ligands. These values are calculated based on the scattered fluorescent intensity at a given wavelength. The results are shown in Table 2.1. and the corresponding Figures can be found in the ESI (Figures S1-30-S1-35). Despite triplicate recordings, values are ambiguous for the latter case (**OF-nap**), possibly due to the increased flexible character of the organic ligands (different ligand configurations and/or coordination) and/or the structural-electronic changes imposed by the lipophilic-electron-withdrawing character of the CF_3 group. The LOD values for **SH-nap** and **OH-nap** are comparable to already existing systems (see chart 1 in ESI[256,258,260,266–272])

Table 2.1. LOD calculated values for all ligands and Cu^{2+} and Fe^{3+}

	Cu^{2+}	**Fe^{3+}**
SH-nap (570nm)	0.1757 µM	0.4638 µM
OH-nap (500nm)	0.4553 µM	0.3157 µM
OF-nap (470nm)	0.2855 µM*	0.0031 µM*

* LOD calculations incorporated only six points despite three repetitions; given the flexible character of the system, we consider these values ambiguous.

2.2. Solution studies.

Given the extraordinary selective sensing process of **SH-nap**, we performed potentiometric studies in a mixed solvent DMSO-H_2O (1:1) system at a millimolar scale (2mM); three orders of magnitude in

higher concentration compared to the titration studies (Figure S1-36). We incorporated DMSO due to ligand insolubility; sadly, efforts to mimic the solvent system of the titration process (DMSO-CH_3CN-H_2O) were impossible. From these studies, we identified four deprotonation constants (Table S1-2); two for the phenolic hydroxyl groups and two for the protonated NH groups. The smallest pK value belongs to the deprotonation of one NH group, the second to one OH group, and the other two deprotonation processes overlap. The interaction of **SH-nap** with Cu^{2+} and Fe^{3+} ions was studied at a 1:1 ligand ratio (Figure S1-37). The fitted titration data define the pH-dependent formation of different species and that complexation proceeds faster for Fe^{3+} at low pH values. For example, at pH 4, only 20% of the Fe^{3+} ions are free; three different species can be identified, while for Cu^{2+}, 30% of the metal remains intact, and only two species can be identified; however, this observation may be irrelevant to the observed difference in quenching for Cu^{2+} over Fe^{3+} (Figure 2.1.2, A), since by increasing the pH, other species are formed. Given that the titration studies were performed in a mixed solvent system without a pH buffer, we cannot suggest which species is dominant during the quenching process.

2.3. Control experiments.

To validate the *in-situ* formation of the complex(es), we recorded ESI-MS data of the titration experiments with Cu^{2+} and Fe^{3+} (Figures S1-38-S1-42). These studies illustrate the formation of the corresponding {ML} specie. However, for the Cu trials, the formation of the dehydrogenated {ML^D} species (-2H) is evident (Figure 2.3.1, A, Figures S1-39 & S1-42), thus perplexing the sensing mechanism. We cannot determine the {ML}/ {MLD} ratio from the ESI-MS studies, while IR studies to identify the C=N bond are inconclusive. For **OH-nap** and **OF-nap**, the fluorescence of both ligands' quenches in the presence of Cu^{2+} or Fe^{3+} ions. It shows similar behaviour to the rest of the transition elements. However, for **SH-nap**, a minor secondary coordination sphere change significantly impacts the fluorescence behaviour. The fluorescence quenches completely for the Cu^{2+} sample but lags for the Fe^{3+} sample. Based on the Hard Soft Acid Base

principles,[46] the formation of the Fe-S bond is favoured; thus, a cluster formation (Figure 2.3.1, B) scenario is doable. [273,274]

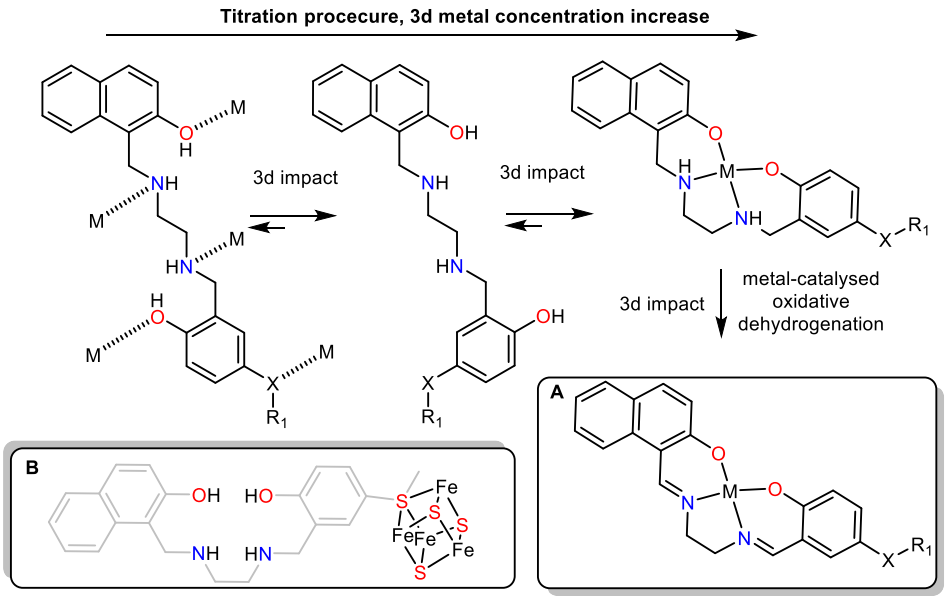

Figure 2.3.1. (Upper, Left to right) Possible configurations the ligand may adopt while metal titration starts, retaining intact the naphtho group for visualising purposes. Possible interactions with metal ions are shown only in the first configuration. SXRD has confirmed the configuration on the left. The last configuration has an ideal pocket for 3d transition elements. Other configurations are possible but not shown (Lower, A) A possible metal-catalysed oxidative dehydrogenation product;[41,263] data observed in ESI-MS studies. (B) A possible Fe-S cluster formation shall explain the Cu^{2+}-Fe^{3+} discrimination observed with **SH-nap**.

2.4. Theory

To gain further insight into the specificity of the complexation and the probable concomitance on fluorescence modulation, we performed computational studies within the Kohn-Sham Density Functional Theory (DFT) at the OLYP-D3/def2-SVP level of theory in the gas phase. We used the so-called ETS-NOCV[275] approach, as implemented in the Multiwfn programme,[276] which allows quantifying the energy of interaction between the metal centre and the ligand in terms of orbital interactions. Furthermore, the methodology allows the visualisation of electron flow upon complexation at the geometry of the most stable structural configuration. To probe the excitation profile, we performed time-dependent DFT calculations on the synthesised **SH-nap**, **OH-nap** and **OF-nap** species and for comparison purposes, we included the hypothetical **SF-nap** species (that is, the organic ligand with the X=S and R_1 = CF_3, Figure 2.1.1.). A straightforward application of ligand-field theory and open-shell DFT formalisms can

rationalise the observed calculated structures (Figure 2.4.1.). A closer inspection indicates that : (a) the ligands are flexible enough to accommodate both the square planar (**sqp**) and tetrahedral (**td**) geometries, (b) the Cu^{2+} S = 1/2 and Fe^{3+} S = 5/2 can be found in either of the two geometries, (c) the observed configuration are functions of both the metal centre and the selection of the X and R^1 groups and (d) there is a facile rotation of the naphtho group. We argue that for the d^9 Cu^{2+} complexes, the **td** geometry is favoured over the Jahn-Teller distorted **sqp** geometry when the metal centre is subject to a large charge induced by the naptho (left) and phenyl (right) groups. This leads to a population of the singly occupied dx^2-y^2 orbital, originating as one of the e^*_g in the OH field, hence the incentive to adopt a lower symmetry is removed. Any axial ligand in the resulting higher symmetry OH would be weakly bound (e.g. solvent species) and, given the oxygen atoms, are relatively large and highly negatively charged, rendering the tetrahedral structure to be preferred.

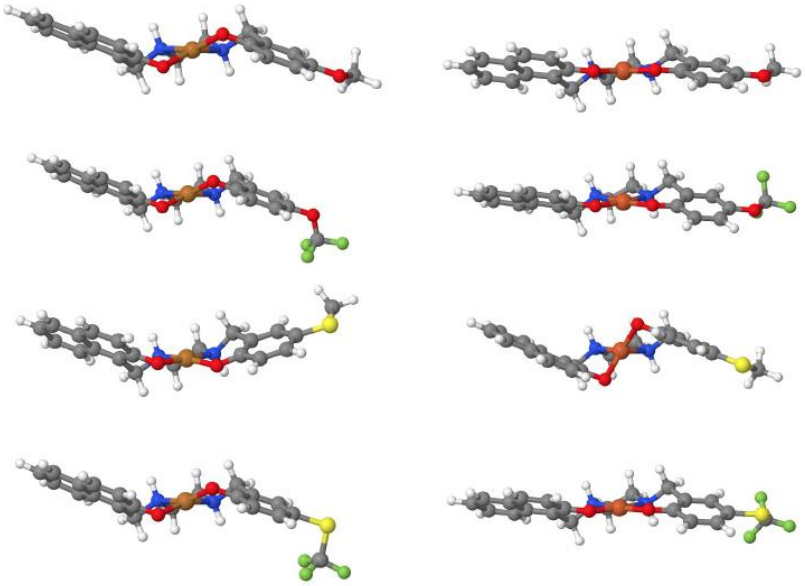

Figure 2.4.1. The calculated structures from top to bottom **OH-nap, OF-nap, SH-nap**, and **SF-nap** (not synthesised) for Cu^{2+} left and Fe^{3+} right.

On the other hand, with an O-Ph-S frame on the right (**SH-nap**), less charge density flows to the Cu centre. It becomes advantageous to go towards the lower symmetry D_{4h} field, given the benefit of having the d_{xy} orbital (originating from the t^2_g group) doubly occupied. Supposedly, this doubly occupied orbital loses one of its electrons (as in the hypothetical case: O-Ph-SCF_3 (**SF-nap**), the incentive is lost, and the **td** is preferred again. The same reasoning can be applied in the case of Fe^{3+}, e.g. the high-spin d^5 configuration

would peremptorily favour the removal of degeneracy towards a lower symmetry field. Our results are given and discussed below (a full and comprehensive study of the interstate *E-e* coupling is beyond the scope of the current manuscript and will be published elsewhere).

Some selected so-called NOCV pairs are shown in Figure 2.4.2 (upper). The direction of charge flux upon complexation is depicted as going from blue to green iso-surfaces. It can be noted that charge influx is both from the two groups flanking the metal centre, showcasing the feature of the ligands. Moreover, the molecular electrostatic potential (MEP) for selected complexes (Figure 2.4.2, lower) visually concludes the considerable charge accumulation interaction between the oxygen atom and the metal centre. This impact increases in the presence of S at the other end, leading to a **td** geometry (see above). It can be noted that the strongest orbital interactions between a given metal and a series of ligands are those found in **SH-nap** for both Cu^{2+} and Fe^{3+} metal centres, values are given in Table S1-3 in the ESI.

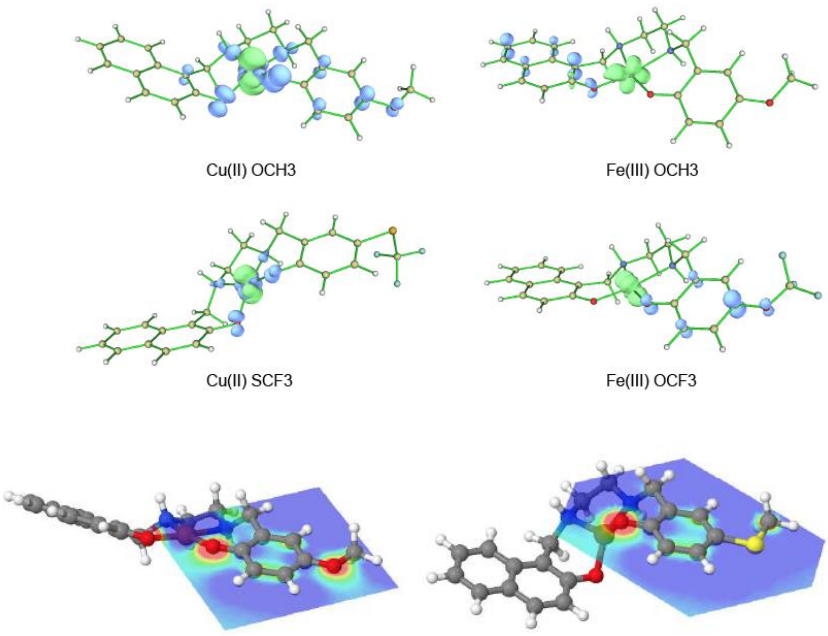

Figure 2.4.2 (upper) Some NOCV pairs (lower) MEPs on **OH-nap** (left) and **SH-nap** (right)

Lastly, we investigated the excitation profile of two specific systems (Figure 2.4.3), and argued that all d-d, MLCT and LMCT transitions mainly contribute to quenching fluorescence. In Figure S1-43, the orbital levels exhibit a connection between the polarisation of a and b electrons profile and the degree of 'electron supply' to the metal

centre, dictating if rearrangements, including Jahn-Teller distortion, would likely take place (see above discussion).

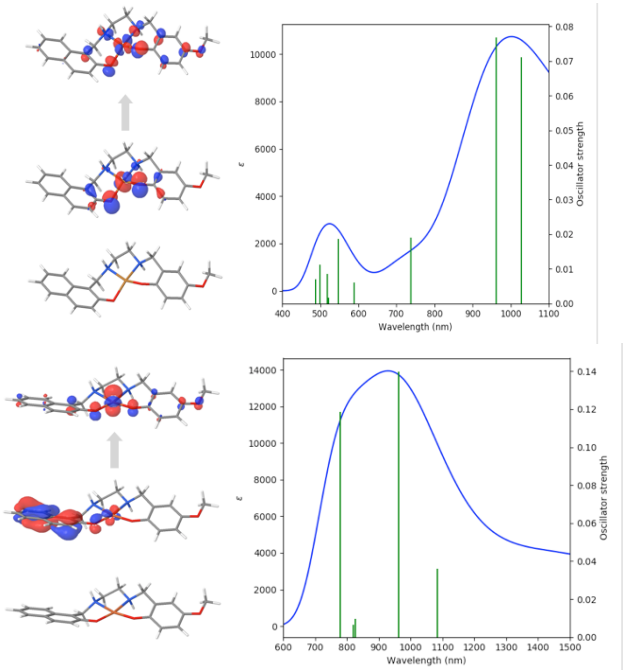

Figure 2.4.3. Calculated excitation profile of Cu^{2+}-**OH-nap** (left) and Fe^{3+}-**OH-nap** (right) and main contributions.

2.5. Conclusions.

We report three novel structurally similar asymmetric salans and investigate their ability to operate as fluorescent sensors for first-row transition elements. These flexible and difficult-to-control ligands bear selectivity towards Cu^{2+} and Fe^{3+}. Secondary coordination sphere alterations prove vital; **SH-nap** is solely selective towards Cu^{2+}. Control experiments and solution studies are controversial; however, computational studies fully rationalise the observed geometries and explicitly explaining the unique and exploitable features of the present systems, despite the ligand flexibility, charge redirection and the presence of modulation and characteristic excitations. Structural arrangements are necessary to improve the performance and solubility of these species, and this work is under investigation in our laboratory.

3 Chapter 3: Fluorine-based Zn complexes for amine sensing

Abstract We synthesised and characterised the racemic and chiral versions of two Zn^{2+} salan fluorine-based complexes from commercially available materials. The complexes are susceptible to absorbing H_2O from the atmosphere. In solution (DMSO-H_2O) and at the millimolar level, experimental and theoretical studies identify that these complexes exist in a dimeric-monomeric equilibrium. We also investigated the ability of these complexes to sense chiral amines via ^{19}F NMR. In $CDCl_3$ or d^6-DMSO, strongly coordinating molecules (H_2O or DMSO) are the limiting factor in using these easy-to-make complexes as chemosensory platforms since their exchange with analytes requires a high excess of the latter.

External Contributions: G.E. Kostakis, G. J. Tizzard and S. J. Coles performed and evaluated the crystallographic data. A. Galvácsi and C. Kállay performed solution studies. Y. Al-Hilaly performed and helped with the evaluation of circular dichroism studies. R. González-Méndez performed and evaluated MS studies. G. R. Akien performed diffusion ^{19}F NMR studies. Maria Besora performed theoretical calculations. All other authors contributed to the success and preparation of the articles.

3.1. Introduction

A compound is considered chiral when it exists in two or more asymmetric forms with non-superimposable mirror images without changing its bond orders, atom-atom connections, and atomic compositions and these forms are called enantiomers.[277] Nature is full of chiral components such as amino acids, saccharides, peptides, enzymes, and proteins,[94] while many chiral compounds in the pharmaceutical industry and material sciences possess biological activity.[278,279] The enantiomeric synthesis of asymmetric compounds has rapidly increased over the years[280], and more complicated and sophisticated systems have been developed.[159] For example, enzymes are used as catalysts to promote organic transformations,[281] chiral compounds are used in different stages of drug discovery [282, 283] and amino acids are used as building blocks for larger molecules i.e. protein, nucleic acid, and components of food and beverages.[284]

Two enantiomers have the same physical properties but may possess different pharmacological and biological activities.[160] Conventional high-performance liquid

chromatography (HPLC) can separate the enantiomers,[161] but this approach involves costly chiral columns. Thus, developing new methods for enantiomeric discrimination is highly interesting for industrial and biomedical applications and is subsequently vital for future discoveries.[162] For example, circular dichroism (CD) and fluorescence,[163–170] monitor absorbance intensity change(s) whereas Nuclear Magnetic Resonance (NMR) proceeds chemically shifted signals;[171–174] these methods rely on host-guest interaction(s); therefore thermodynamic and kinetic parameters and equipment's response time signify method applicability and limitation. In the latter case, methods incorporating chiral templates and ^{1}H-NMR are popular,[175–180] however lately, emphasis is given to developing hetero nuclear-based methods i.e. ^{31}P[173,181] or ^{19}F.[84,182,183]The latter method has the following two advantages: lack of background interference;[182,183] thus applies to large molecules, such as proteins,[84,184] and a broad detection window from -200ppm to +200 ppm depending the antenna, i.e -CF_3, -OCF_3, -F and so on.[82] Pioneer works from Swager[185,186] and Song[187] establish the principles in using new or modifying already known chiral fluorine-based complexes for discriminating chiral amine based methods. Both methods work in non-coordinating solvents and rely on the host-guest interaction principle; thus, two different peaks appear in the ^{19}F NMR spectrum. In the latter case, the methods also apply coordinate solvents, and its operational window is 0.21 ppm.

The condensation reaction of salicylic aldehyde and ethylenediamine yields the well-known versatile salen framework (Figure 3.1.1 upper), which has been extensively used to produce complexes with applications in catalysis, and sensing.[227,228,237–241,229–236] From the synthetic perspective, the corresponding Zn^{2+} complexes crystallise as dimers; however, in solution, they either form monomers in coordinating solvents or the presence of a base, or aggregates, non-coordinating solvents. The former process is well discussed and recently reviewed by Di Bella.[233] In this review, the coordination number that the metal centre adopts depends on the solvent system and the presence (absence) of substrates, varying from four to six. Notably, the reduced version of salen, which means salan ligands (Figure 3.1.1, upper right) and their corresponding Zn^{2+} complexes, have been less investigated.[285–292] These compounds are susceptible to oxidative dehydrogenation, depending on the solvent medium.[36,41] Only 31 crystal structures have been deposited in the CSD.[293] The sp^3 carbon atoms of the salan framework impose flexibility and, consequently, possible alterations in the geometry of the metal centre, deviating from the dominant square planar and/or square pyramidal conformation.

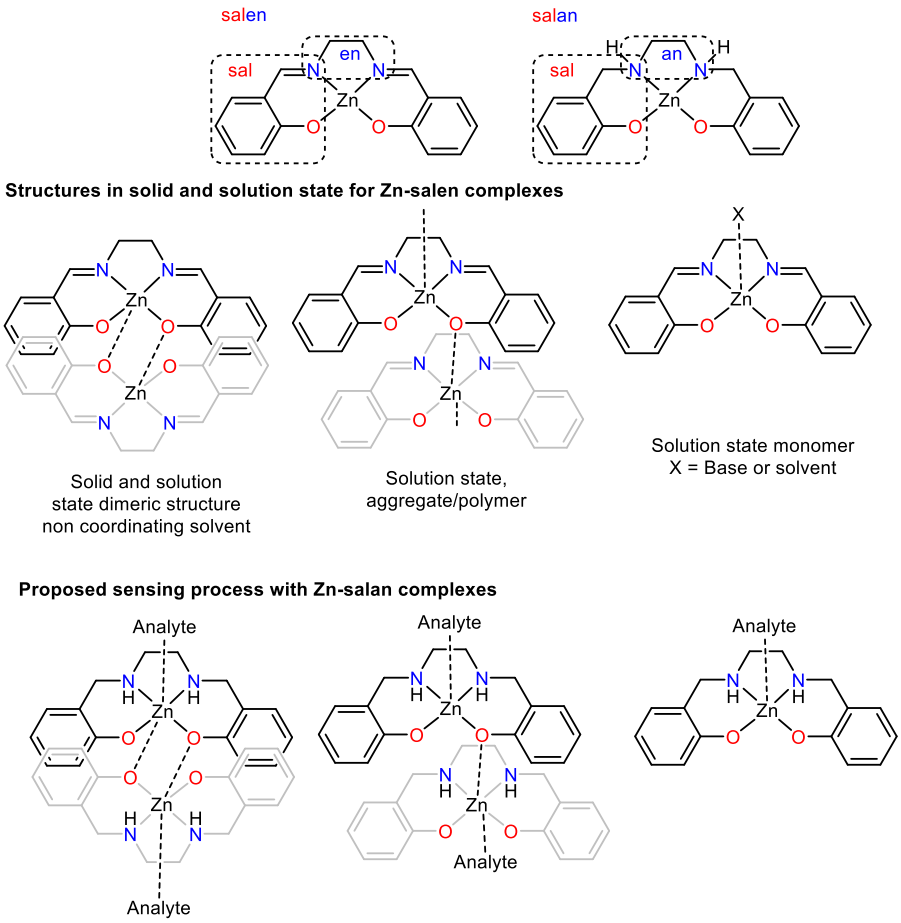

Figure 3.1.1. (Upper) The differentiation of salen and salan framework (middle) possible structures in solid and solution (lower) possible sensing processes.

Previous studies identify the ability of Zn^{2+} complexes to sense biologically important small molecules[153] such as amino acids,[294, 295] amines, saccharides[296,137] and ribonucleosides[297] using fluorescent spectroscopy. Recently Zhao suggested that Zn^{2+} salen complexes, ideal models for catalysis, are inappropriate for sensing purposes because the structural changes (dimer-monomer, solvent monomerization, Figure 3.1.1, above) interfere chronically with the sensing process, thereby averaging the ^{19}F NMR signals of the interconverting species.[298]

With all these in mind, we embarked on a project examining the sensing ability of chiral Zn salan complexes with ^{19}F NMR. We detail our ligand-complex design criteria for this purpose (Figure 3.1.2). The use of salan frameworks will increase the flexibility of the organic framework and consequently affect the coordination geometry of the metal centre. However, incorporating the rigid cyclohexane backbone instead of the en moiety will impede the flexible character. Next, we wanted to investigate the impact of the different antennae (F vs OCF_3) but also varying its position, adjacent or away from

the sensing point (metal centre). Thirdly, we investigated if altering the chirality of the host will impact the sensing process. Lastly, we envisaged these complexes existing as dimers in the solid state and possibly in the solution state; therefore, we wondered if highly saturated analyte solutions will favour the sole {Figure 3.1.1 lower} formation, thus advancing a new sensing process.

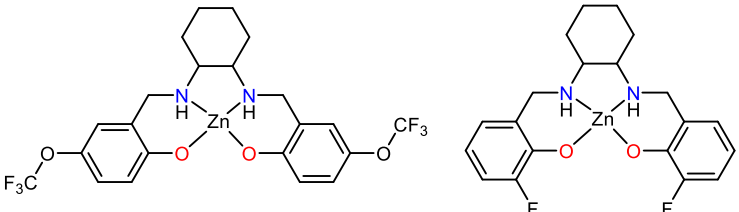

Figure 3.1.2. The selected two frameworks for this study.

3.2. Results

3.2.1. Synthesis of the ligands.

All ligands can be synthesised using commercially available chemicals in two high-yielding steps, avoiding column chromatography (Figure 3.2.1.1). The ligands have been characterised by NMR (^{1}H, ^{13}C, ^{19}F), IR, UV-Vis, and HR-MS (with ESI as an ion source). The chirality of each species has been determined by Circular Dichroism (CD) (Figure 3.2.1.2), observing the opposite enantiomer. The total yield for the ligands varies between 78 – 98%.

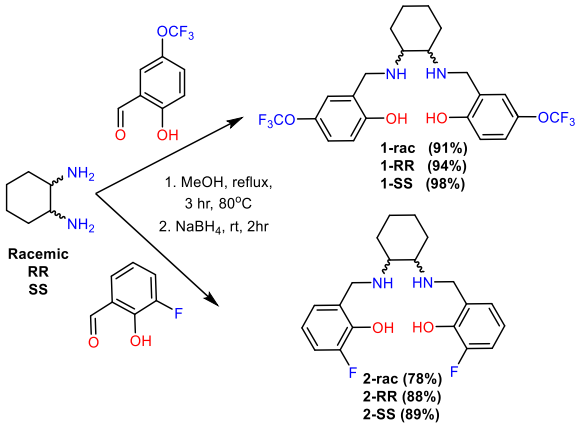

Figure 3.2.1.1. A simplified version of the synthetic routes to yield all ligands.

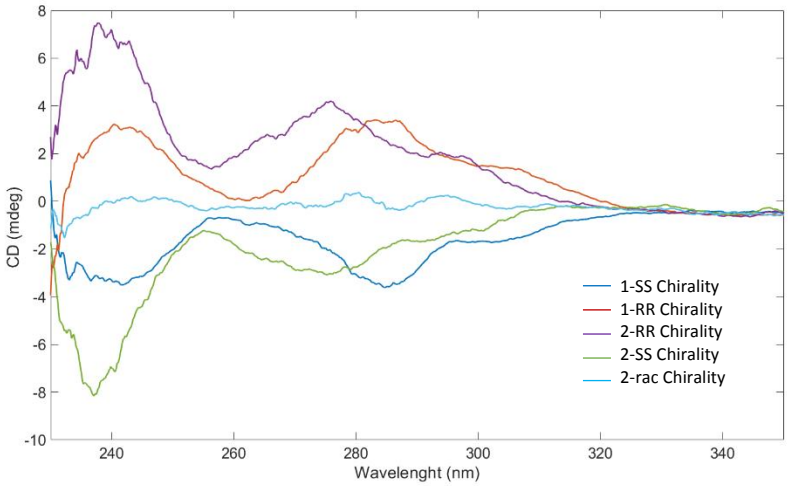

Figure 3.2.1.2. The Circular Dichroism spectra for the ligands (solvent, MeOH, concentration $1x10^{-3}$ M, temperature 298K)

3.2.2. Complex synthesis.

With the ligands in hand and bulk, we performed several reactions for synthesising the corresponding Zn^{2+} complexes. We screened several parameters such as metal salt ($Zn(NO_3)_2$ $6(H_2O)$, $ZnCl_2$, $Zn(OTf)_2$, $Zn(BF_4)_2$, $Zn(ClO_4)_2$, solvent (MeOH, CH_2Cl_2, EtOH, CH_3CN), metal : ligand ratio (3:1 to 1:3), temperature (25°C, 50°C, 75°C), base (Et_3N, Na_2CO_3, K_2CO_3) and identified the optimum conditions as : $Zn(NO_3)_2$ $6(H_2O)$: Ligand : Na_2CO_3 in a molar ratio 1:1:1, on a mixture of solvents MeOH/H_2O (10/2mL). The metal salt and ligand were dissolved in methanol, and the solution turned milky upon adding an aqueous Na_2CO_3 solution. After 1 hr of reflux, the solution was filtered, and the filtrate was kept for slow evaporation. Shiny block-shaped colourless crystals were collected in good to moderate yields between four to fourteen days.

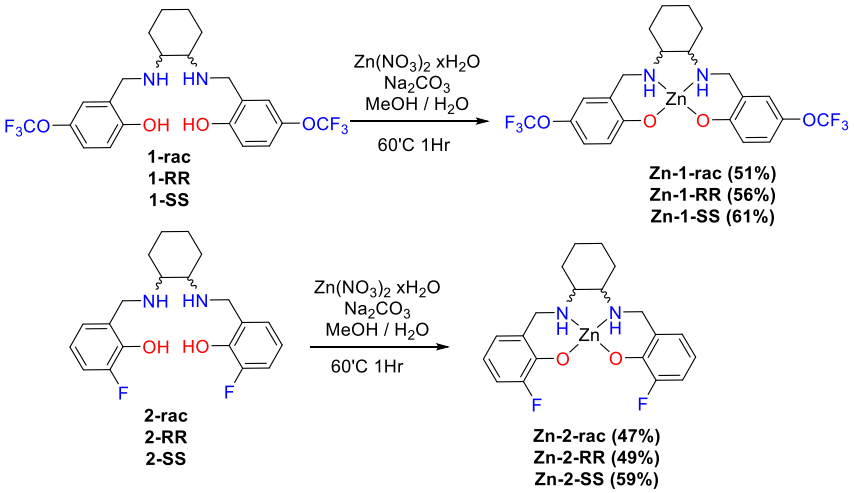

Figure 3.2.2.1 The synthetic procedure for the synthesis of **Zn-1** and **Zn-2** families.

3.2.3. Characterisation in the solid state.

Single crystal X-Ray diffraction studies (Table S2-1) for **Zn-1** and **Zn-2** families identified the formation of dimers for all cases; however, minor differentiations could be identified in the crystallised lattice molecules for **Zn-1-RR** and **Zn-1-SS**. No lattice molecules could be determined for compound **Zn-1-rac**, however the actual formula for **Zn-1-RR** is [ZnL 1(CH_3OH) 0.375(H_2O)] and for **Zn-1-SS** is [ZnL 2(CH_3OH)]. For the **Zn-2** family, all compounds crystallise as [ZnL 2(H_2O)]. All lattice molecules form hydrogen bonding interactions with the metalloligand (ZnL) moieties. **Zn-1-rac** and **Zn-2-rac** crystallise in achiral space groups ($P2_1/n$ and $P\bar{1}$), while the remaining four complexes crystallise in chiral space groups. The Zn centre inclines to adopt a trigonal bipyramidal geometry (Figure S2-49 & Table 3.2.3.1.). Notably, for the chiral species, two different indexes could be determined; however, their average is close to the index calculated for the non-chiral species (Table 3.2.3.1.). In all species, the C–N bond is within the range of single bond values, discarding the occurrence of oxidative dehydrogenation,[41,263] while the phenoxide C–O bond is within the range of a single bond value. The Flack parameter value (Table S2-1) for all four compounds is close to zero, thus determining enantiomeric purity. The compounds were further characterised by Thermogravimetric (TG) and elemental (CHN) analysis, which slightly deviated from the expected calculated values. They are consistent with additional lattice solvent molecules. (Figure S2-50).

Table 3.2.3.1. Selected Bond distances for all complexes and trigonality index

	Zn-O1	Zn-O2	Zn-O3	Zn-N1	Zn-N2	Trigonality index (τ)[299]
Zn-1-*rac*	2.057(3)	2.068(3)	1.963(3)	2.110(4)	2.141(3)	0.68
Zn-1-*RR*	2.079(7)	1.987(7)	1.990(8)	2.132(8)	2.186(8)	0.61
	1.985(8)	2.108(7)	1.987(7)	2.101(8)	2.189(8)	0.65
Zn-1-*SS*	2.088(5)	2.002(5)	1.981(6)	2.132(7)	2.190(6)	0.61
	1.995(5)	2.086(5)	1.966(6)	2.194(7)	2.126(8)	0.60
Zn-2-*rac*	1.959(4)	2.049(4)	2.101(4)	2.141(5)	2.093(5)	0.61
Zn-2-*RR*	1.959(4)	2.095(5)	2.040(4)	2.149(5)	2.109(5)	0.74
	2.051(4)	2.099(5)	1.950(4)	2.115(5)	2.133(5)	0.50
Zn-2-*SS*	1.954(5)	2.099(6)	2.051(5)	2.133(7)	2.111(6)	0.50
	2.046(5)	2.097(6)	1.959(5)	2.111(6)	2.152(7)	0.74

Trigonality index indicates the geometry of the coordination center.[299] When τ = 0 the geometry corresponds to square pyramidal, when τ= 1 corresponds to trigonal bipyramidal.

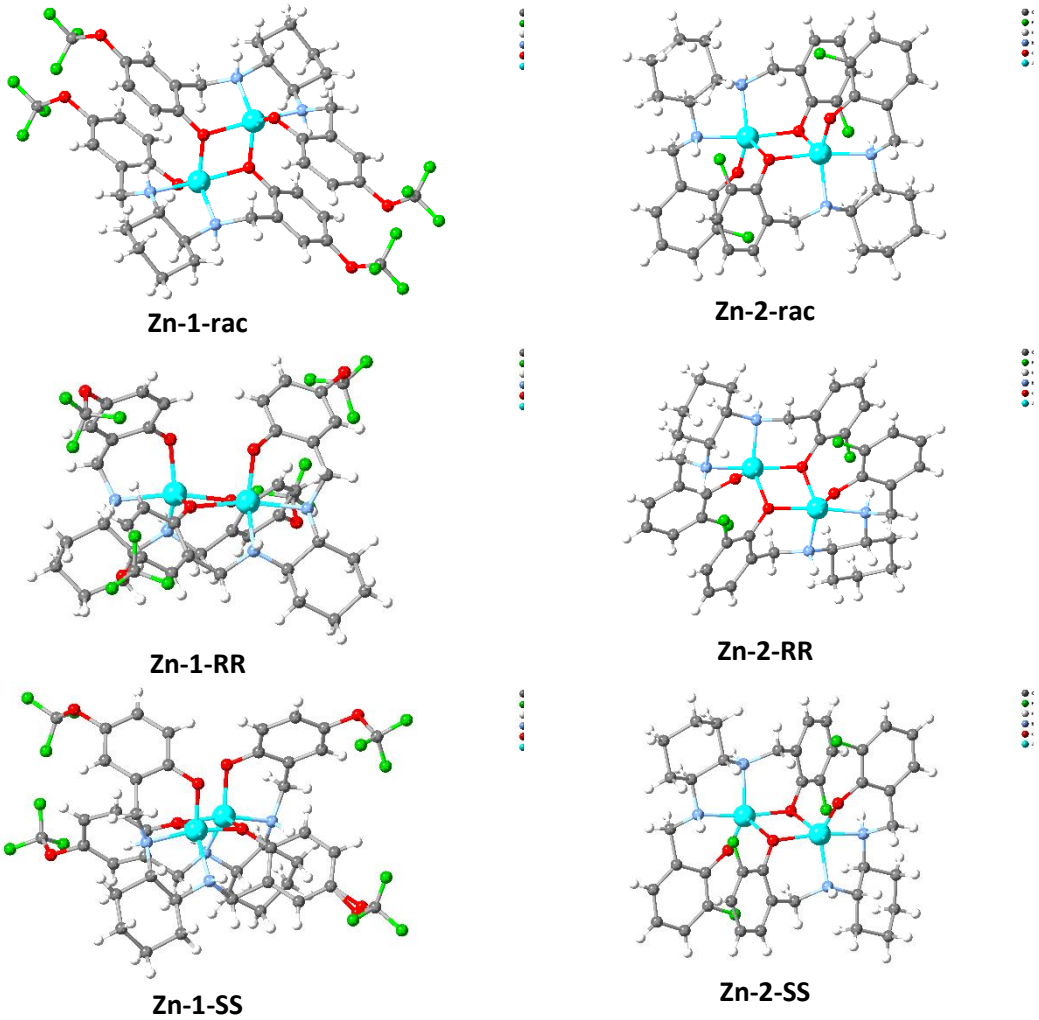

Figure 3.2.3.1. Crystallographic representation of **Zn-1** (left)and **Zn-2** (right) families. Lattice solvent molecules have been omitted for clarity. Colour code; Zn (light blue), O (red), N (blue), C (grey), H(white), F (green).

3.2.4. Characterisation in solution state.

With the complexes in hand, we attempted to elucidate if they retain their structure in solution; therefore, we recorded ^{1}H and ^{19}F NMR, CD and ESI-MS. The ESI-MS data for **Zn-1-RR** (Fig S2-51) validate the formation of monomeric and dimeric species; a characteristic peak with corresponding isotropic distribution can be identified for both species. CD studies of selected samples in DMSO validate the retention of the enantiomeric form (Figure 3.2.4.1. A). Then, we recorded ^{1}H and ^{19}F NMR data using a coordinating solvent (d^{6}-DMSO) and compared them with the free ligands (Figure 3.2.4.1. B&C and ESI). From these data, complexation is evident; characteristic peaks in the aromatic and cyclohexane backbone regions shift at different values in ^{1}H NMR. In ^{19}F NMR the sole peak shifts by 0.1 ppm (Fig 3.2.4.1.C), whereas for the **Zn-2** family, the peak shifts almost by 1 ppm (0.87ppm, Figure S2-53). Minor peaks can be observed in

the ^{1}H NMR of **Zn-1-SS**; however, this may be attributed to different species formed in solution (see Figure 3.1.1), rather than impurities since the ^{19}F NMR data suggests the presence of only one species. To validate the existence of a monomeric or a dimeric species, we performed ^{19}F NMR diffusion studies (Figure 3.2.4.1. D). However, the data was inconclusive as the apparent molecular weight was intermediate between the putative monomeric and dimeric species.[300]

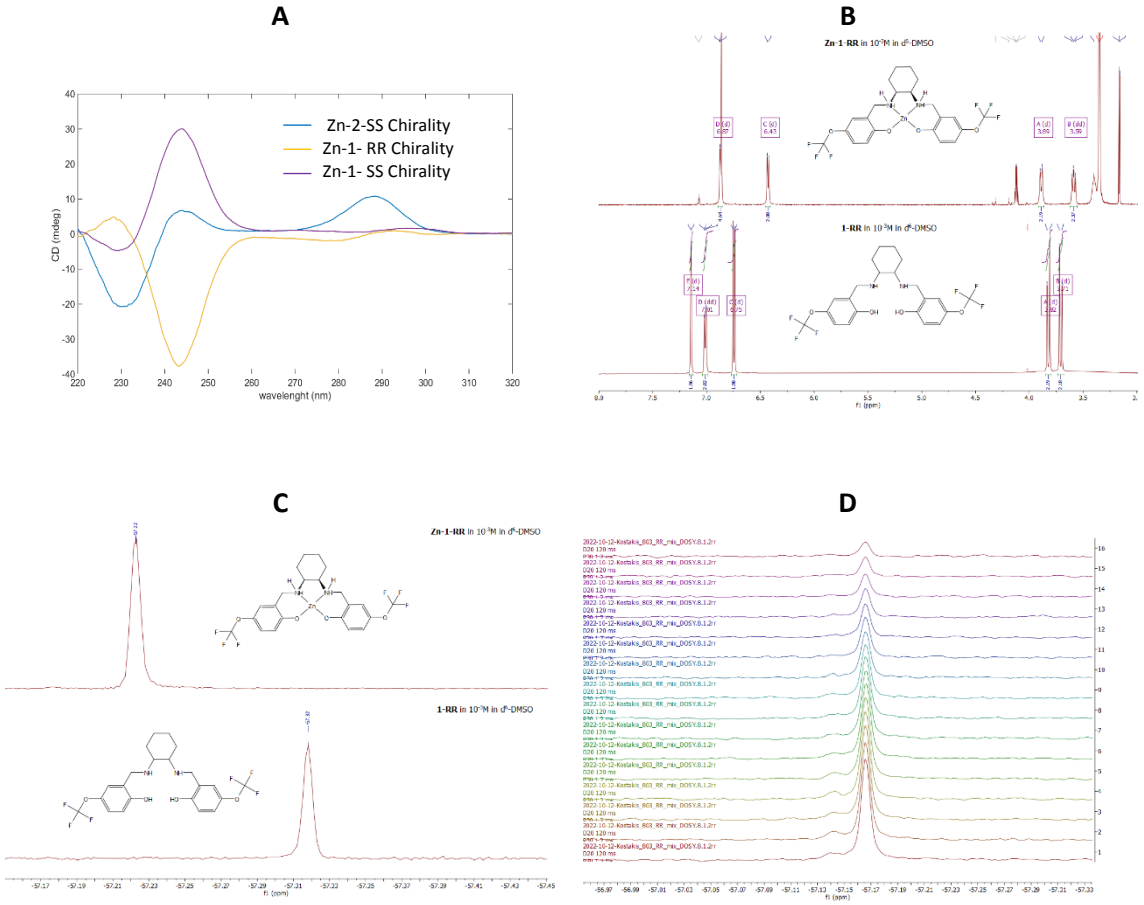

Figure 3.2.4.1. (A) The Circular Dichroism spectra for selected complexes **Zn-1-RR, Zn-1-SS** and **Zn-2-SS**. (concentration 1x10^{-3} M) (B&C) ^{1}H and ^{19}F NMR comparison of **1-RR** and **Zn-1-RR** in d^{6}-DMSO. (D) ^{19}F NMR diffusion studies

We performed potentiometric studies for **2-rac** and its corresponding **Zn-2-rac** complex at a millimolar level in two concentrations (0.2 and 1.2 mM). Four deprotonation constants can be calculated for the two phenolic OH and two NH groups. The lowest pK value belongs to the deprotonation of one NH group, while the other deprotonation processes overlap. The lowest pK values in all measurements agree with each other; however, the basic pH range values slightly differ in the samples with different ligand concentrations. The solution at 1.2 mM concentration becomes turbid above pH 9, prohibiting further evaluation. The higher pK values were set from the

0.2mM measurements. The interaction of the ligand with Zn^{2+} was studied at a 1:2 metal-to-ligand ratio in 0.2 and 1.2 mM (for the ligand) solutions; the data were evaluated considering the monomeric and dimeric species (Figure 3.2.4.2). From the distribution curves (Table 3.2.4.1), we note that (a) the higher ligand concentration shifts the complex formation to lower pH, and (b) the formation of the deprotonated dimeric complex in the 1.2 mM solution is favoured. Notably, upon ligand concentration increase, the data fitting improves with the dimeric model, and at a concentration of 1.2 mM, the formation of the dimeric complex is more favourable.

Table 3.2.4.1. Protonation constants (logβ) and pK values of **2-rac** in solutions of different concentrations (I = 0.2 M, T = 298 K, standard deviations are in parentheses)

Ligand	**2-rac**			
c[mM]	0.2		1.2	
	logβ	pK	logβ	pK
HL	10.99(4)	10.99(4)	10.99*	10.99*
H_2L	20.49(6)	9.50(6)	20.49*	9.50*
H_3L	27.83(8)	7.34(8)	27.89(2)	7.40(2)
H_4L	32.1(9)	4.27(9)	31.94(3)	4.05(3)

* originates from the pK calculation of the 0.2 M solution

Ligand	**2-rac**			
c[mM]	0.2		1.2	
ZnLH	19.20(12)	Fitting: 5.33E-04	19.47 (12)	Fitting: 1.96E-03
ZnL	14.00(2)		13.49(11)	
$Zn_2L_2H_2$	-	Fitting: 6.98E-04	41.97 (18)	Fitting: 5.02E-04
Zn_2L_2H	38.18(5)		36.9(3)	
Zn_2L_2	31.96(6)		27.96(11)	

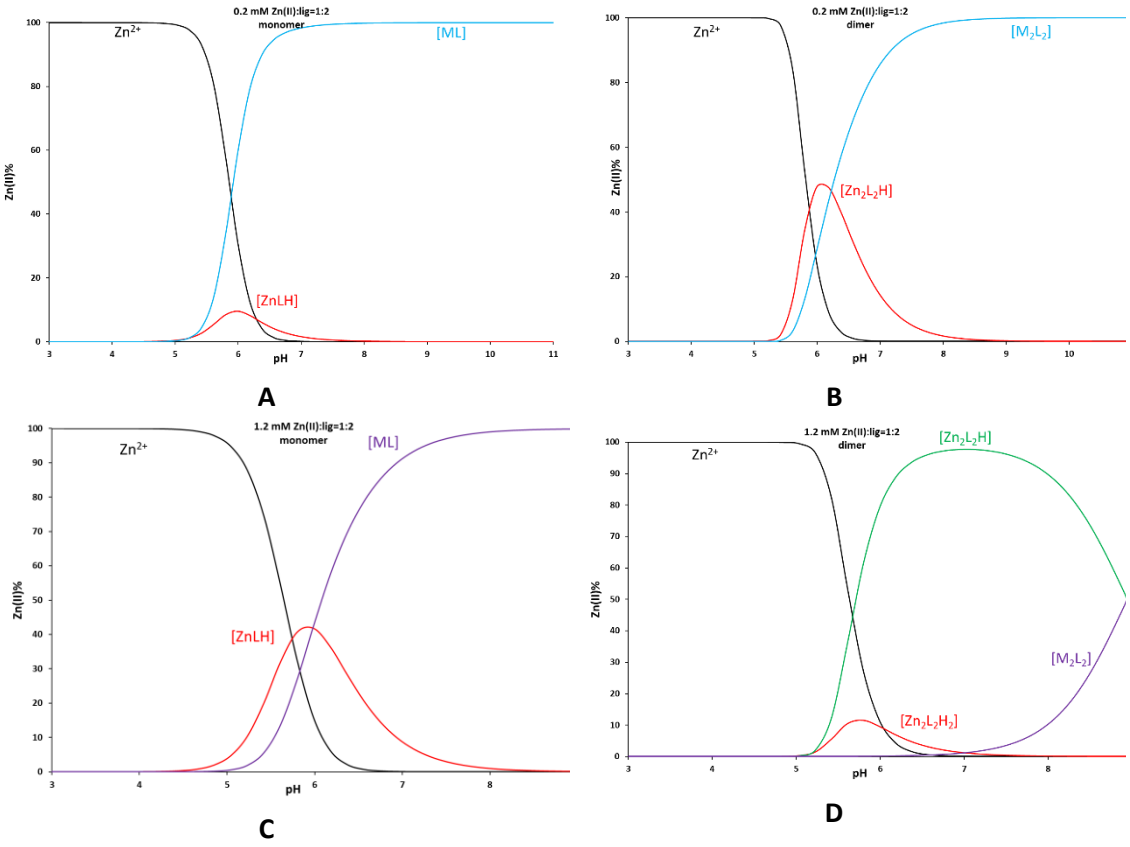

Figure 3.2.4.2. Species distribution for the **Zn-2-rac** system at different concentrations (0.2mM, **A**, **B**; 1.2mM, **C**,**D**) with monomeric (**A**,**C**) and dimeric (**B**,**D**) models.

3.2.5. Sensing studies.

With the complexes in hand, we attempted to identify the best solvent system for the sensing process, with $CDCl_3$ being our first choice. The data presented herein are the outcome of mixing the analyte and the complex within the NMR tube, avoiding stirring or sonication for prolonged periods; the reason for this choice is our aim to develop an efficient, convenient and rapid sensing system. Our first trial for **Zn-1RR** (Figure S2-54), identifies that this non-coordinating solvent system levies monomeric-dimeric competition,[233] therefore, we discarded its use. Then we used a binary solvent system ($CDCl_3$-DMSO) in different ratios. However, the same behaviour was observed again (results are not presented). Thus, we concluded that DMSO would be the ideal system to perform the sensing process. The ^{19}F NMR data of the complexes (Figure 3.2.5.1) identify a single broad peak, indicating an equilibrium (monomer vs dimer) is favoured, or different types of interactions occur.[184] Titrations of **Zn-1RR** and **Zn-1SS** at millimolar scale with phenylglycinol in ratios (1:5 to 1:50) show minimal differences, thus prohibiting us to further continue with this study. Given that we incorporated a strongly

coordinating solvent (DMSO) which may occupy the coordinating site on the Zn centre, we tried experiments with 1:100 and 1:150 ratio to favour the DMSO-analyte exchange. The latter experiment (1:150) possibly suggests that a ligand (**1-RR** vs analyte) exchange process starts taking place (Figure 3.1.1, lower).

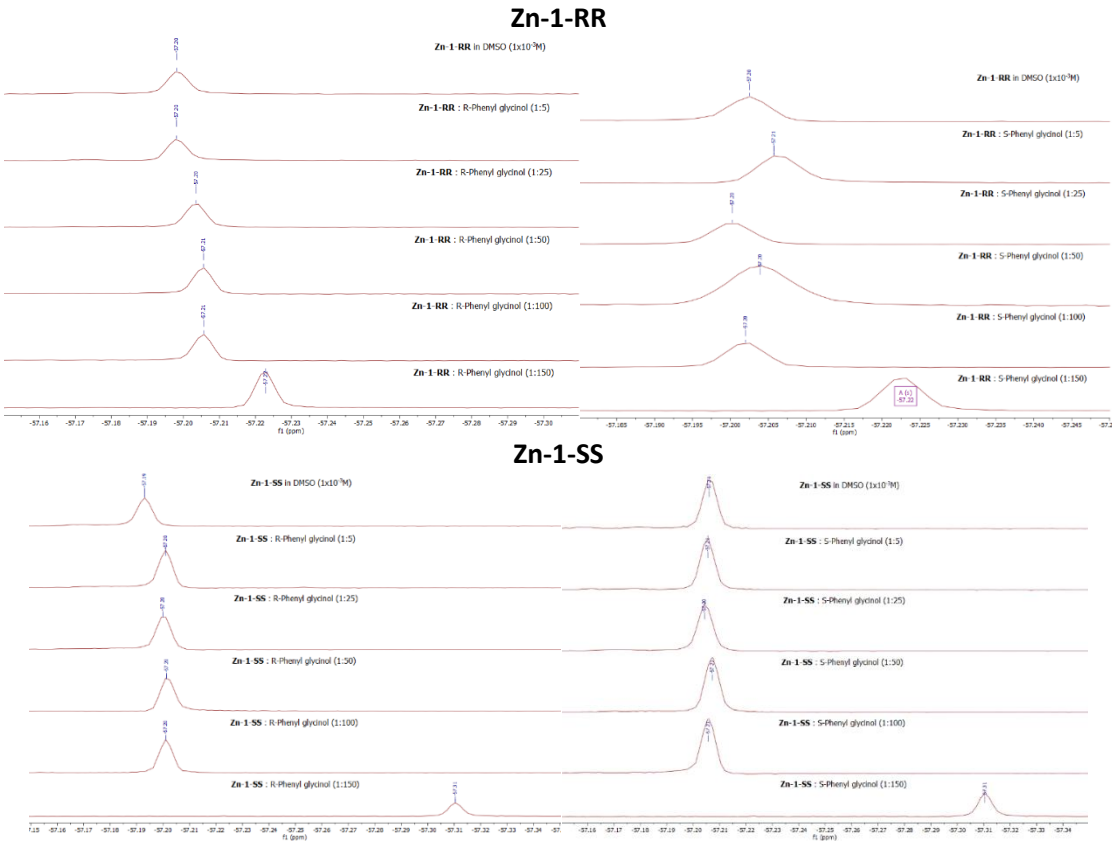

Figure 3.2.5.1. ^{19}F NMR data of **Zn-1RR** and **Zn-1SS** with phenylglycinol. Concentration 10^{-3} M, temperature 303K.

Then we studied the sensing ability of **Zn-1RR** with other analytes and **Zn-2RR** with phenylglycinol (Figure 3.2.5.1). Our first choice was to incorporate a diamine as the analyte at different ratios (1:20, 1:50 and 1:100). The data from the first trial shows the main peak, slightly shifted, and two minor peaks, which could be indicative of the formation of the complex+analyte species, however, given that none of the two peaks is of the same intensity or integral with the main peak, we discarded this set of experiments from future studies. We also tried a different diamine as an analyte. However, we noted a slight shift in the principal peak and the appearance of a minor peak. The same observation was noted when an amino acid was incorporated as an analyte. Last, we used **Zn-2RR** and phenyl glycinol at high complex analyte ratios (1:100 and 1:150), but again, one single peak could be observed.

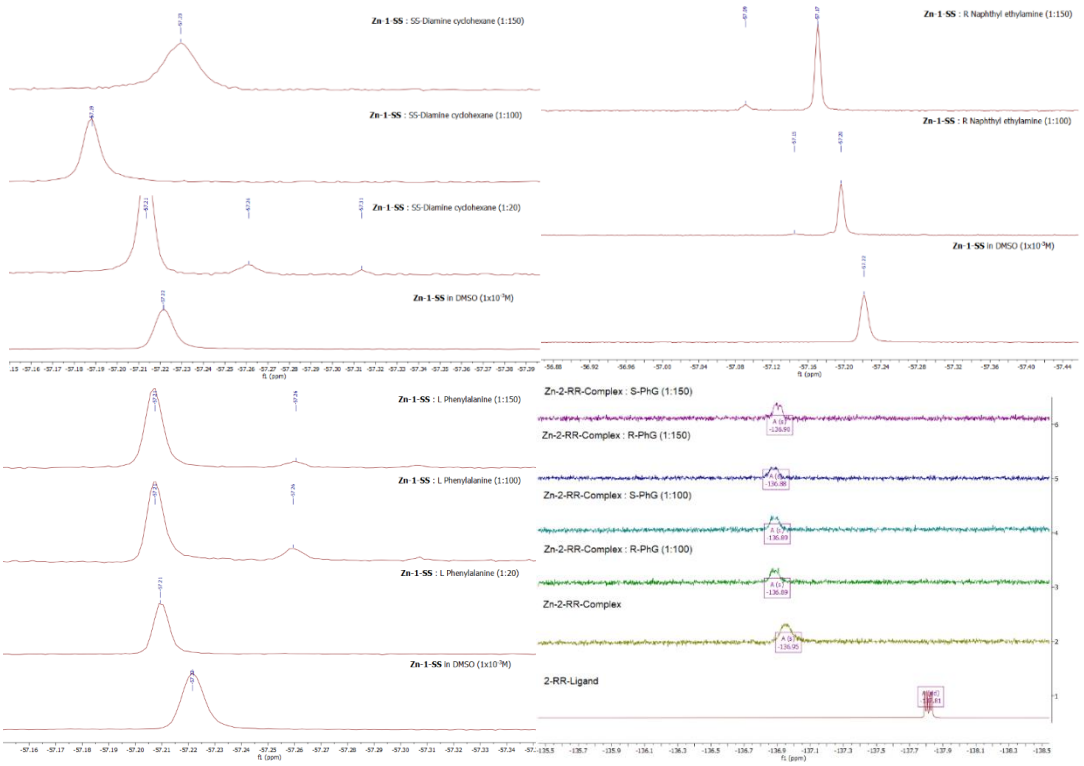

Figure 3.2.5.2. ^{19}F NMR data of Zn-1RR with various analytes and Zn-2RR with phenylglycinol. Concentration 10^{-3}M, temperature 308K.

3.3. DFT studies.

We performed a DFT study to investigate the species of **Zn-1-RR** formed in solution, to support the interpretation of the observed experimental signals. Calculations were carried out to model the system in a non-coordinating solvent (chloroform) and a coordinating one (DMSO). To find the most relevant species, we screened the conformational space using CREST,[301] and re-optimised in Gaussian[302] the lowest and most representative minima at the B3LYP[303–305]-D3[306]/6-31g(d,p)[307,308] & SDD[309] level. The solvent (chloroform or DMSO) was modelled as a continuum media using PCM[310,311], in some calculations, up to two DMSO explicit molecules were included (see Computational Details in ESI). Results in chloroform show that without an analyte or coordinating solvent, the **Zn-1-RR** optimised structure resembles that (**Dimer)** defined by single X-Ray diffraction. The **Dimer** is thermodynamically stable compared to two molecules of the corresponding **Monomer** by 20.5 kcal.mol^{-1}, suggesting the absence of the **Monomer** species in these conditions. However, two distinctive signals can be observed in the ^{19}F NMR experimentally. For this reason, we decided to reinvestigate the system, considering the possible presence of some water molecules. Different

conformers of the **Monomer** and **Dimer** were optimised with the presence of one, two or three coordinating water molecules. When one water molecule coordinates with the **Dimer**, it produces an intermediate species **Dimer(H_2O)** which is 7.8 kcal.mol^{-1} more stable; hence water coordination is favoured. For the **Monomer**, the **Monomer(H_2O)** is favoured by 13.8 kcal.mol^{-1}. However, the significant instability of the **Monomer** compared to the **Dimer**, makes **Monomer(H_2O)** less stable than **Dimer(H_2O)** by 14.5 kcal.mol$^{-1;}$ hence this species could neither be experimentally observed. Calculations accounting for two coordinating water molecules result in **Dimer(H_2O)$_2$** and **Monomer(H_2O)$_2$** with relative energies of -16.0 and -8.6 kcal.mol$^{-1,}$ respectively from the **Dimer**. The coordination of this second water molecule reduces the difference between monomeric and dimeric species. However, the dimer is still preferred by 7.4 kcal.mol^{-1}. The most stable isomer of **Monomer(H_2O)$_2$** presents a geometry with a water molecule coordinated to Zn and the other, forming a bridge between the oxygen of the ligand and the coordinated water. The geometry of this species suggests that a strong interaction with a third water molecule could be favoured. Calculations including a third water molecule yield **Dimer(H_2O)$_3$** and **Monomer(H_2O)$_3$** with relative energies of -24.2 and -21.9 kcal.mol^{-1}, respectively respect to **Dimer**, see Figure 3.3.1.

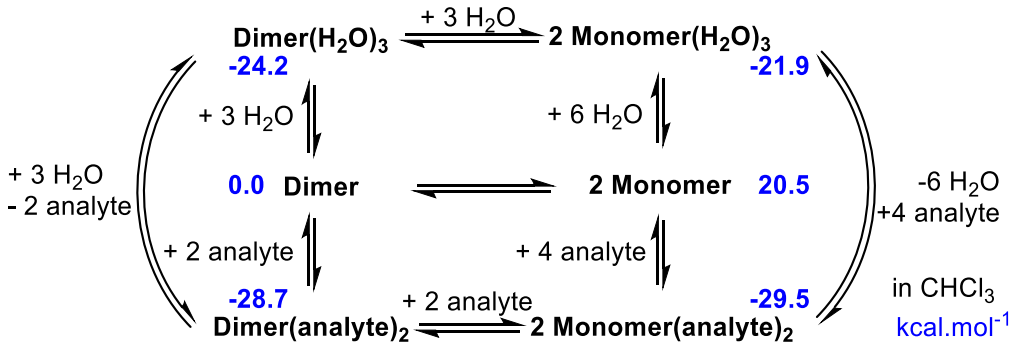

Figure 3.3.1. Schematic representation of a simplified reaction network of the most relevant species and their relative free energies in chloroform and kcal.mol^{-1}.

The difference between monomeric and dimeric species is small (2.3 kcal.mol^{-1}), and depending on the water's concentration, both species could be observed. Please note that computational free energies reported corresponding to the 1 M Standard State. If we have concentrations significantly different from 1 M the energies alone cannot predict the formed species, and concentrations must be considered.[312] The overall equilibrium between these two species is governed by the chemical equation

Dimer(H_2O)$_3$ + 3 H_2O ⇌ 2 **Monomer(H_2O)$_3$**, this means that K_{eq} = [**Monomer(H_2O)$_3$**]^2/([**Dimer(H_2O)$_3$**][H_2O]^3) = 8.3. Hence at concentrations of water above [H_2O] = ([**Monomer(H_2O)$_3$**]^2/([**Dimer(H_2O)$_3$**]K_{eq})$^{1/3}$, the monomer will be observed while below the dimer will be observed assuming there is enough water to form **Dimer(H_2O)$_3$.** We checked the monomer to total ratio as m/t = [**Monomer(H_2O)$_3$**]/[**Dimer**]$_0$x100 at different concentrations of water, where [**Dimer**]$_0$ is the initial concentration of dimer.

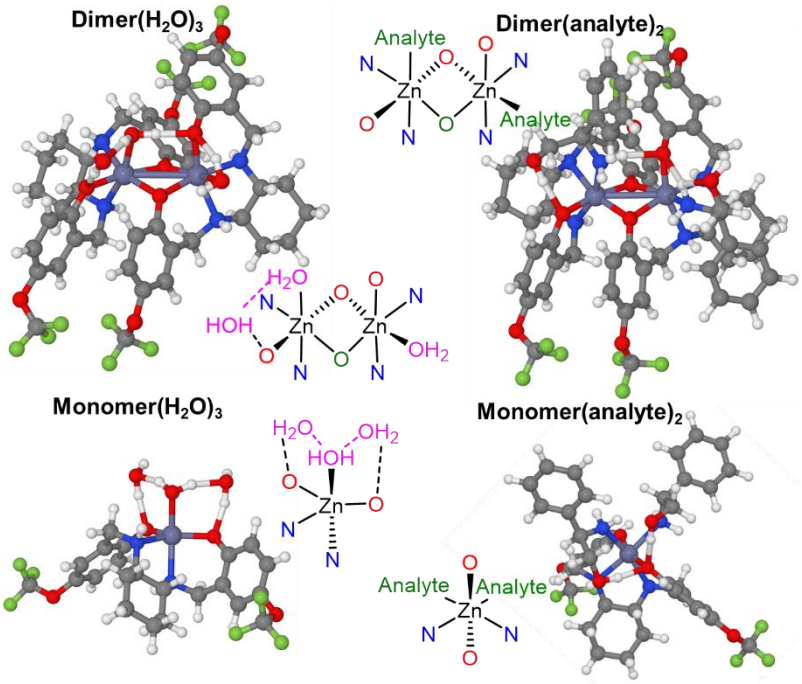

Figure 3.3.2.: Ball stick representation of the calculated structures of the **Dimer(H_2O)$_3$**, **Dimer(analyte)$_2$**, **Monomer(H_2O)$_3$** and **Monomer(analyte)$_2$**, in chloroform.

For initial concentrations of water [H_2O]$_0$= 0.01, 0.1, 0.25 and 0.5 M, the predicted m/t ratio is 0.3%, 14 %, 50% and 110%, suggesting that indeed in the reaction media **Dimer(H_2O)$_3$** and **Monomer(H_2O)$_3$** could be present at the same time. Please note that as small errors in computational free energies will impact the equilibrium constants, we can only provide a qualitative explanation. The monomer-dimer equilibrium observed for initial water concentrations between 0.1 and 0.5 M could be at concentrations lower or higher.[313] The geometries of **Dimer(H_2O)$_3$** and **Monomer(H_2O)$_3$** are presented in Figure 3.2.5.2. The most stable dimeric species presents a water molecule strongly coordinated to one of the Zn and another weakly coordinated to the other Zn, forming hydrogen bonds with the ligand (Zn-O distances 2.21 and 2.60 Å). The third water

molecule bridges the strongly coordinated water molecule and one of the ligand's oxygens ((OH--O distances are 1.61 and 1.74 Å). In the monomer, the structure presents one water molecule coordinated to the Zn and the other two bridges between the coordinated water and two oxygens of the ligand (OH--O(lig) distances are 1.69 and 1.65 Å and ZnO(H)H--O 1.71 and 1.72 Å). Adding more water molecules has not been considered as more strong interactions seem unlikely, and conformational complexity increases.

We also searched the structures related to analyte sensing. In this case, we considered the coordination of one and two analyte molecules, (R) 2-Phenylglycinol, to the monomer and the dimer. We found that **Dimer(analyte)**, **Monomer(analyte)** are located at -13.3 and -6.7 kcal.mol^{-1} and **Dimer(analyte)$_2$**, and **Monomer(analyte)$_2$** at -28.7 and -29.5 kcal.mol^{-1}, respectively; see Figures 3.3.1 and Figure 3.2.5.2. In this case, there is no space for the coordination of a third analyte molecule. Formation of **Monomer(analyte)$_2$** species is primarily favoured. The practical difficulties for sensing analytes at low concentrations seem to be due to the need for water–analyte exchange. The main chemical equations of the equilibria, in this case, are **Dimer(H$_2$O)$_3$** + 4 analyte ⇌ 2 **Monomer(analyte)$_2$** + 3 H_2O and **Monomer(H$_2$O)$_3$** + 2 analyte ⇌ 2 **Monomer(analyte)$_2$** + 3 H_2O. The energy difference between the aqua and analyte species is significant, 5.3 kcal.mol^{-1} and 3.8 kcal.mol^{-1}, respectively. In both cases, the expressions depend upon the concentration of water and analyte. The two equilibriums are related, as well as to the previously mentioned species. Hence, a system of 12 equations needs to be solved to find the concentration of all species at equilibrium (see SI). Using the concentration of water 0.5 M (an approximate value according to the results above), we tested the a/t ratio = [**Monomer(analyte)$_2$**]/([**Dimer**]$_0$)×100 at the [analyte]$_0$ = [**Dimer**]$_0$, 10×[**Dimer**]$_0$ and 100×[**Dimer**]$_0$; the respective a/t ratios are 0.5 %, 29 % and 178 % (please note the relation between dimer and monomer is 1 to 2). These results show that the relationship between water/analyte concentrations impacts the sensing ability of the complexes.

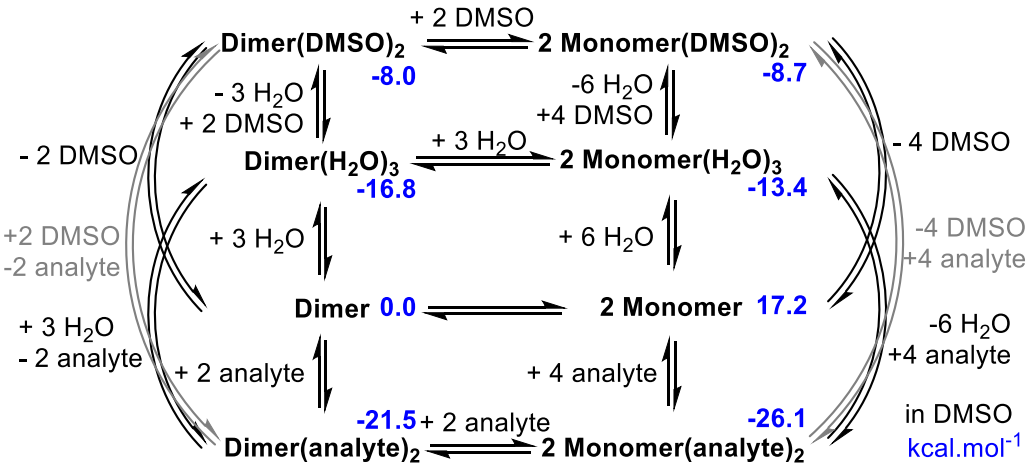

Figure 3.3.3. Schematic representation of a simplified reaction network of the most relevant species and their relative free energies in DMSO and in kcal.mol^{-1}.

Following experimental results, we explored the equilibria in DMSO. The above-presented minima were computationally reoptimised using DMSO as the solvent, and the results are presented in Figure 3.3.3. The different conformers for the dimeric and monomeric species with one and two DMSO molecules coordinated were also searched. We found that coordination of a DMSO molecule to form **Dimer(DMSO)** is favoured by -5.7 kcal.mol^{-1} and the inclusion of a second DMSO molecule slightly stabilises the resulting **Dimer(DMSO)$_2$** to -8.0 kcal.mol^{-1} respect to **Dimer**. The most stable conformer for **Dimer(DMSO)$_2$** is presented in Figure 3.3.4, DMSO coordinates through the oxygen. Each **Monomer** is also stabilised by the coordination of DMSO molecules, the first DMSO stabilises the monomer in 7.6 kcal.mol^{-1} and the second 5.4 kcal.mol^{-1} more (see, Figures 3.3.3 and Figure 3.3.4). Hence, two **Monomer(DMSO)$_2$** molecules have similar energy as one **Dimer(DMSO)$_2$** (two monomers are 0.7 kcal.mol^{-1} more stable). However, both are significantly less stable than the complexes with water or analyte molecules coordinated. Indeed, the most stable minimum is that of the **Monomer(analyte)$_2$**, however the concentration of DMSO is several orders of magnitude larger than that of the analyte. The chemical equations, corresponding equilibrium constants, and mass balances were written to predict the concentration of all species at equilibria. Concentrations were obtained by solving a system of 19 equations and 19 unknown variables considering initial concentrations 14.06 M DMSO, 0.50 M water, 1 10^{-3} M Dimer, no concentration of the rest of species except for the analyte for which we considered 0, 1 10^{-3}, 1 10^{-2} and 0.1 M. At none or low concentration of analyte, the most abundant species is **Mono(DMSO)$_2$**. Although this complex is less stable than the complexes with analyte

and water, the large concentration of DMSO concerning the rest of the coordinating molecules (< 0.5 M) makes the equilibria shift towards its formation. It is also interesting to note that although the stability of **Mono(DMSO)$_2$** and **Dimer(DMSO)$_2$** is similar the chemical equation **Dimer(DMSO)$_2$** + 2 DMSO ⇌ 2 **Monomer(DMSO)$_2$** is also displaced towards the formation of **Monomer(DMSO)$_2$** for the same reason. At an increasing analyte concentration, the most abundant species becomes **Monomer(analyte)$_2$**. The computational a/t ratio = [**Monomer(analyte)$_2$**]/([**Dimer**]$_0$)×100 and d/t ratio = [**Monomer(DMSO)$_2$**]/([**Dimer**]$_0$)×100 at different initial concentrations of the analyte [analyte]$_0$ = 0.0, 1 10^{-3}, 1 10^{-2} and 0.1 M are a/t = 0%, 2 %, 87 % and 198 % and d/t = 192 %, 190 %, 108 %, 2 % explaining the difficulties associated to analyte sensing. Please note that in DMSO the concentration of water has an effect; decreasing the water concentration does not have a significant impact (i.e. [H_2O]$_0$ = 0.05 M results in a/t = 0%, 2 %, 89 % and 198 % and d/t = 200 %, 198 %, 110 %, 2 % respectively for [analyte]$_0$ = 0.0, 1 10^{-3}, 1 10^{-2} and 0.1 M), but if the concentration of water is higher **Monomer(H_2O)$_3$** would be formed instead of **Monomer(DMSO)$_2$**. For instance, considering [H_2O]$_0$ = 5 M and [analyte]$_0$ = 1 10^{-2} M **Monomer(H_2O)$_3$** is formed and is more difficult to sense the analyte as the a/t, d/t, and m/t ratios are 7 %, 6 % and 186%. Increasing the concentration of analyte and considering [H_2O]$_0$ = 5 M and [analyte]$_0$ = 0.1 M **Monomer(analyte)$_2$** species is formed. These ratios change to a/t, d/t, and m/t 154 %, 1 % and 45 %, respectively.

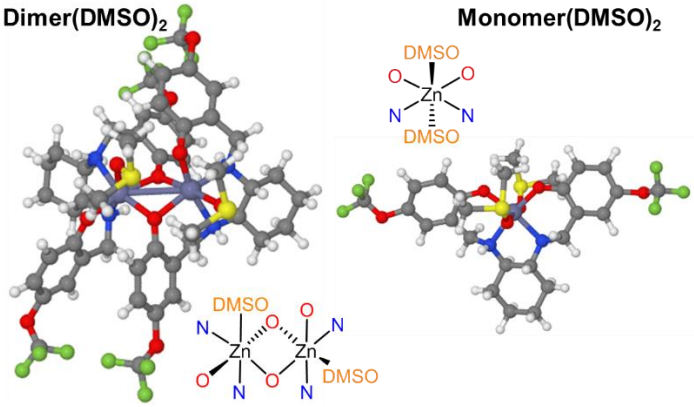

Figure 3.3.4: Ball stick representation of the calculated structures of the **Dimer(DMSO)$_2$** and **Monomer(DMSO)$_2$**, in DMSO.

3.4. Conclusions.

We examined for the first time the ability of fluorine-based Zn^{2+}-salan complexes to sense chiral amines with ^{19}F NMR. These compounds are isolated as dimers and exist in a dimer-monomer equilibrium in solution at a millimolar level favouring the former when coordinating solvents are used, in contrast to known Zn^{2+}-salen complexes as monomers.[233] These coordinating solvents occupy vacant positions in the Zn^{2+} coordination sphere, thus, their exchange with analytes requires an excess of the latter for a second peak to appear in the ^{19}F NMR spectrum. This procedure proves challenging and possibly suitable for limited and specific analytes. Theoretical calculations support this notion, indicating that the presence of strongly coordinating molecules is the critical parameter that prohibits the development of a new sensing process at low concentrations. Future synthetic efforts will focus on altering the organic framework and having the antenna close to the metal centre to ease the sensing process in non-coordinating solvents.

4 Chapter 4: Multimodal molecular γ-aminobutyric acid (GABA) sensor

Abstract We successfully synthesized a novel water-soluble ligand($H_4oct^{(p\text{-}OCF3)}salox.$) and characterised including the molecular entity $[Yoct^{(p\text{-}OCF3)}salox]^-$ that can be used for multimodal monitoring purposes of GABA NT. And *In vitro* monitoring with UV-Vis, ^{19}F NMR and fluorescence and DFT calculations allow mapping complex/NT interaction and rationalising a possible selective sensing mechanism at a specific concentration.

External Contributions: Harry Carpenter has a critical input in ligand synthesis. Y. Al-Hilaly performed and helped with the evaluation of fluorescent studies. A. Galvácsi and C. Kállay performed solution studies. J. Lai-Morrice and C. Pubill Ulldemolins performed theoretical calculations. All other authors contributed to the preparation of the article.

4.1 Introduction

Neurotransmitters (NTs) are small organic molecules serving as chemical messengers and transmitting signals between nerve and target cells throughout the body via the nervous system.[314,315] This action proceeds in the synapses. A neuron releases an NT, which then passes the synapses and triggers the receiving neuron, causing impulses throughout the nervous system.[316,317] The human body has several NTs with different functions, separated into excitatory and inhibitory NTs, neuromodulators and neurohormones. γ-aminobutyric acid (GABA) is the main inhibitory NT of the brain. GABA binds to receptors on the receiving cell and prevents triggering information. By doing this, GABA subsequently controls various physiological processes, i.e. heart rate and psychological activity. Its imbalance has been linked with pathological damages such as epilepsy, hypersomnia and Alzheimer's. Aiming to shed light on its impact on these pathological conditions, detecting levels of GABA within the body and developing methods to monitor it *in vivo* and *in vitro* become vital.

Various methods of sensing GABA have been developed.[215,315,318,319] For example, the real-time detection levels of GABA with electrochemical processes are doable with excellent sensitivity levels ($36\pm2.5\ pA\mu M^{-1}cm^{-2}$).[320] Looger et al developed a genetically encoded fluorescent glutamate receptor iGluSnFR sensor for in vivo imaging of GABA.[321] Johnson et al developed GABA-Snifit, a semisynthetic fusion protein containing the $GABA_B$ receptor, SNAP- and CLIP-tag, a synthetic fluorophore and a fluorescent $GABA_B$

receptor antagonist.[322] Moreover, a method of acquiring ^{1}H-NMR for GABA detection in the human brain has been successful.[323] However, coordination chemistry has been the driving force in developing a vast library of Gd^{3+} complexes as Magnetic Resonance Imaging (MRI) contrast agents;[172,324–326] and repurposing their use to sense GABA and other NTs with NMR has been successful.[327–331] In most of these studies, the use of a) a polydentate cyclic ligand that confines the coordination geometry around the Gd centre, thus eliminating its interaction with the environment, b) an adjacent cyclic framework to act as a template to the neighbouring NT and the Gd moieties to allow their interaction (Figure 4.1.1, A) and c) ^{1}H NMR, mainly, and ^{19}F NMR[327] as detection method are preferred however developing ligand systems, and their subsequent complexes, for improved imaging purposes remains a significant challenge.

Angelovski and Tóth set the principles for developing ^{19}F NMR probes; the absence of background signal in most tissues facilitates the observation of exogenous ^{19}F probes *in vivo*; however, relatively high concentrations are required compared to classical relaxation agents.[332] The ^{19}F chemical shifts and the relaxation rates are susceptible to changes in the microenvironment which can be exploited for the sensing of various biomarkers, such as pO_2, metal ions or pH.[332] In principle, ^{19}F probes are excellent candidates to produce NT-dependent signal changes *in vitro*, though *in vivo* translation seems complicated due to sensitivity limits.[332]

Yttrium is a transition element, but when it adopts the oxidation state, III has ionic radii and possesses properties similar to Ho^{3+} and Dy^{3+}; thus, it can be considered pseudo-lanthanide. Yttrium salts prove to be toxic,[333] however, diamagnetic Y^{3+} complexes, built from multidentate ligands to exhibit high thermodynamic stability and be kinetically inert,[334] can provide a route to multimodal imaging; i.e. the same ligands can be coordinated to ^{86}Y and used for PET, ^{90}Y and radiotherapy, and ^{89}Y and HP-MRI, with ^{89}Y chemical shifts extremely sensitive to the molecular environment.[334,335] In a nutshell, Y^{3+} complexes are ideal candidates for NMR and MRI applications. However, their design should be carefully evaluated after considering the denticity, type/number of heteroatoms of several known polydentate ligands.[334] Pioneer work by Orvig has set the ground for developing this type of polydentate ligand. For example, the octadentate ligands H_4octapa[336] (Figure 4.1.1, B) and H_4octox[337] (Figure 4.1.1, C), have proven suitable to form the corresponding Y complexes with significantly increased stabilities in aqueous media.

Having all these in mind, we considered that the asymmetric heptadentate ligand $H_4oct^{(p\text{-}OCF3)}salox$ (Figure 4.1.1, D) represents an ideal candidate to providing the corresponding Y^{3+} complex as a non-invasive multimodal sensor for GABA detection and monitoring, for the following reasons : i) given that Y^{3+} has a slightly lower ionic radii compared to Gd^{3+}, the heptadentate ligand, upon complexation, will partially fulfil the geometry of the Y^{3+} thus facilitating ligand exchange (H_2O vs GABA) and allowing a variety of binding(s) modes: monodentate (N or O), bidentate (O/O) and chelate (N/O); ii) the antenna ^{19}F probe group (p-OCF_3) is not directly adjacent to the Y^{3+} centre; thus, the observed ^{19}F chemical shifts will be subjected to changes to the microenvironment of the whole complex with the NT, iii) the presence of the quinoline group ensures the ability to monitor interactions with fluorescence at lower concentrations, iv) interactions of the Y^{3+}-complex and NTs can be simultaneously monitored with ^{1}H & ^{19}F NMR, fluorescence and UV-Vis spectroscopic methods thus providing detailed information to establish a reliable mechanistic pathway [332,338] and v) the calculated pharmacokinetic properties and druglike nature of the ligand identify a proper framework allowing usage for *in vivo* monitoring.[339]

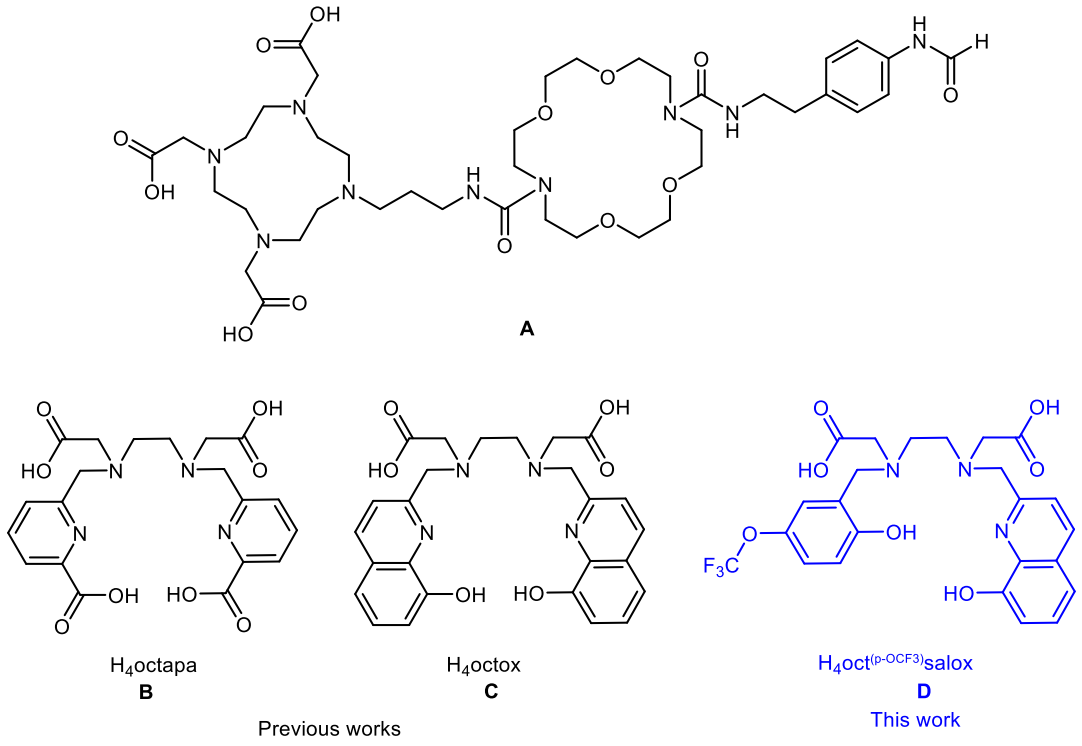

Figure 4.1.1. (Upper) Known framework for NT sensing with NMR (lower) Known frameworks for Y complexes and our work

4.2. Results and Discussion.

4.2.1. Ligand synthesis.

The asymmetric heptandatate ligand 2-((2-((carboxymethyl)((8-hydroxyquinolin-2-yl) methyl) amino) ethyl) (2-hydroxy-5-(trifluoromethoxy)benzyl) amino) acetic acid, $H_4oct^{(p\text{-}OCF3)}salox$ can be synthesised via different synthetic paths, as shown and highlighted in Figure 4.2.1.1.

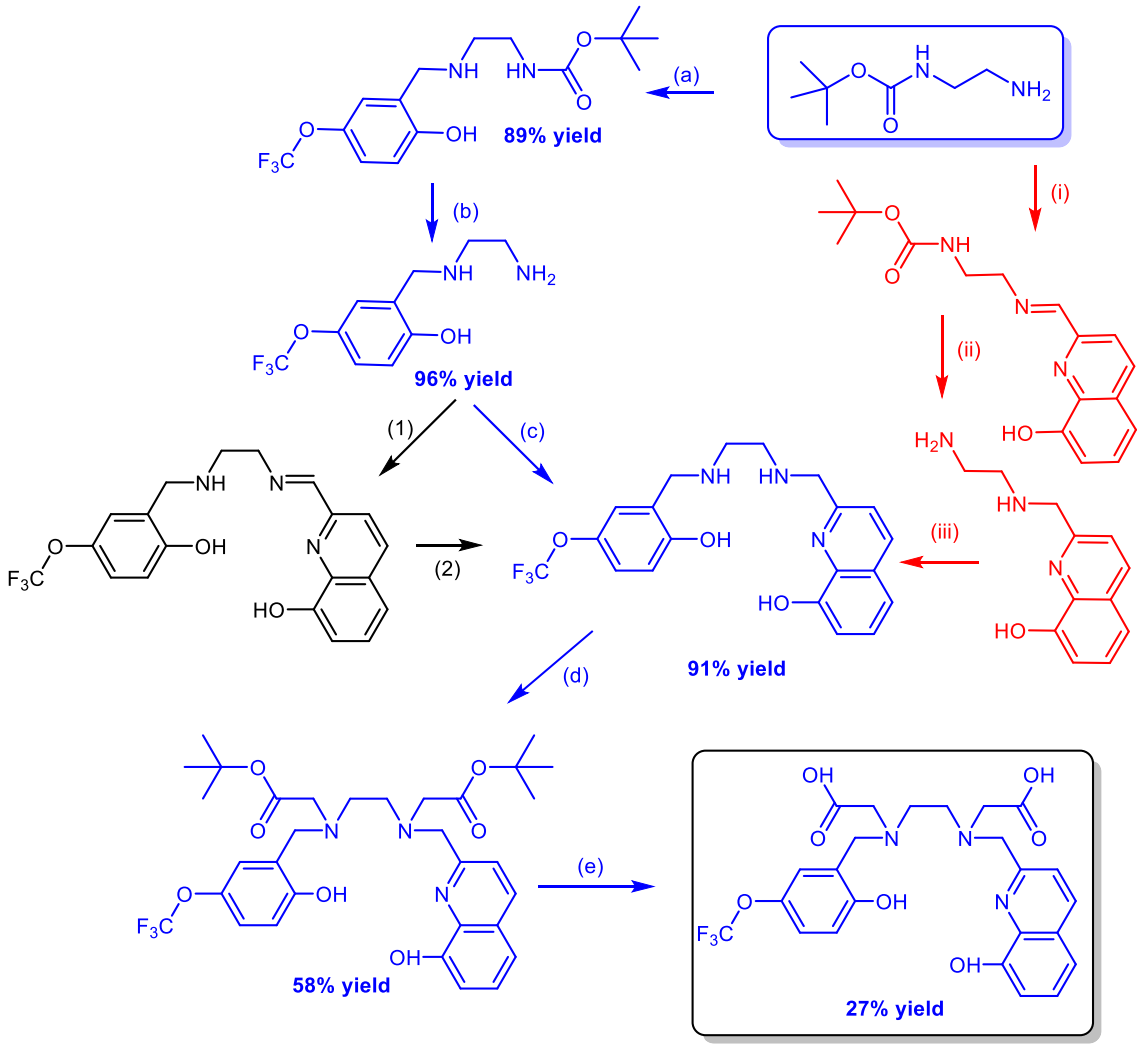

Figure 4.2.1.1. The three interlinked, synthetic pathways to afford $H_4oct^{(p\text{-}OCF3)}salox$. (a) 2-hydroxy-5-trifluoromethoxy benzaldehyde (1eq), MeOH, reflux (24hr), $NaBH_4$ (3eq), 2 hr (89%); (b) 4NHCl in Dioxane/CH_2Cl_2, 24 hr, (96%); (c) 8-Hydroxyquinoline-2-carbaldehyde (1eq), Et_3N (2eq), MeOH, reflux, 0.1gr molecular sieves, 2hr, $NaBH_4$ (4eq) 2hr (91%); (d) CH_3CN, Tert-butyl bromoacetate(3eq), N,N'-Diisopropylamine (2.2eq) RT, under N_2, overnight, (58%); (e) Hexane 6:2 TFA, overnight, rt, DCM/HCl(6N). (27%); (i) 8-Hydroxyquinoline-2-carbaldehyde (1eq), MeOH, reflux (24hr) (75%), (ii) (b) 4NHCl in Dioxane/CH_2Cl_2, 24 hr, 38%); 2-hydroxy-5-trifluoromethoxy benzaldehyde (1eq), Et_3N (2eq), MeOH, reflux, 0.1gr molecular sieves, 2hr, $NaBH_4$ (4eq) 2hr (31%); (1) 8-Hydroxyquinoline-2-carbaldehyde (1eq), Et_3N (2eq), MeOH, 0.1gr molecular sieves, reflux, 24hr (88%); (2) $NaBH_4$ (4eq), 2hr, (27%);

The anticlockwise synthetic part can be exhaustive; however, the shorter path proves to be convenient. We also attempted to synthesise the ligand by following the red path, however, the reactions yield was low, and the precursor became unstable; therefore, we abandoned this pathway. It is worth noting that the final step, deprotection of the tert-butyl groups, affords the acidic version of [H_4oct$^{(p\text{-}OCF3)}$salox 3TFA]; however, ^{19}F NMR data (Figures S3-1); therefore, an additional step to replace TFA with HCl is required. The reasons for this additional step are a) to ensure the interaction of the ligand with the Y^{3+} salts is not impacted by the presence of other anions, b) to certify the formation of the sole [Yoct$^{(p\text{-}OCF3)}$salox]- complex and c) to allow better evaluation of the ^{19}F NMR data (see below). The purity of the ligand has been confirmed via LC-MS (96%) and has been characterised via ^{1}H, ^{13}C, ^{19}F NMR, IR, UV-Vis and ESI-MS (Figures S3-2-S3-17). Following the short path, despite the very good to excellent yields in the first steps, the cumulative yield of the ligand is ~ 28%. The last two steps, deprotection, prove complicated losing the material on column chromatography; however, the ligand can be obtained in almost a gram scale. The synthetic tunability of this framework and the low synthetic cost of the starting materials imply the significance of these asymmetric H_4octsalox derivatives.

4.2.2. Ligand characterisation.

pH-dependent UV-Vis studies suggest stepwise deprotonation of the ligand evidenced by the different spectra at pH 4.0 and 8.0 (Figure 4.2.2.1. A). The ESI MS of the ligand provides the accurate mass (Figure S3-17). In the ^{1}H-NMR data, there are two distinct regions. The first one ranges between 3.00 – 4.70 ppm in which the six methylenic groups can be found, while the aromatic protons span between 6.35 – 8.73 ppm. The ^{19}F NMR of the ligand in D_2O at 25^{o}C identifies two peaks within the range of an OCF_3 group;[182,340,341] the major at -58.56 ppm and the minor at -58.49 ppm and their appearance may be attributed to the existence of different protonated ligand species (Figure 4.2.2.1. B). For this reason, we performed solution studies to determine the pKa values of the ligand. pH-dependent UV-Vis studies assisted in determining the protonation constants (Figure 4.2.2.1. C); calculated by using the SuperQuad[342] program and are summarised in Table 4.2.3.1. pH-dependent UV-Vis studies suggest stepwise deprotonation of the ligand evidenced by the change of the spectra around pH 3.5 and

8.0. At physiological pH values, the ligand is fully deprotonated, however at pH 5.0, two different species exist, therefore this can explain the appearance of the two peaks at ^{19}F NMR. Finally, as anticipated, the ligand is fluorescent (Figure 4.2.2.1. D) at 320nm.

(A)

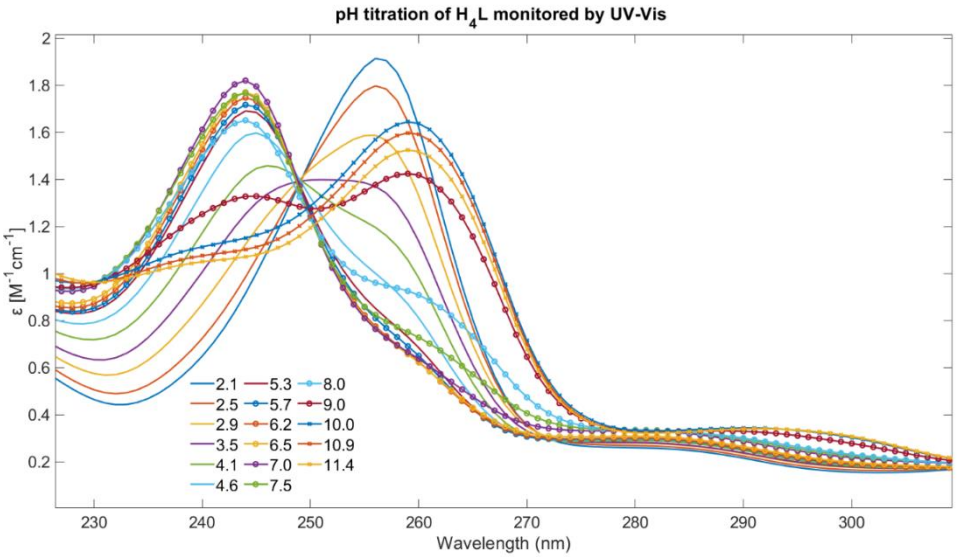

(B)

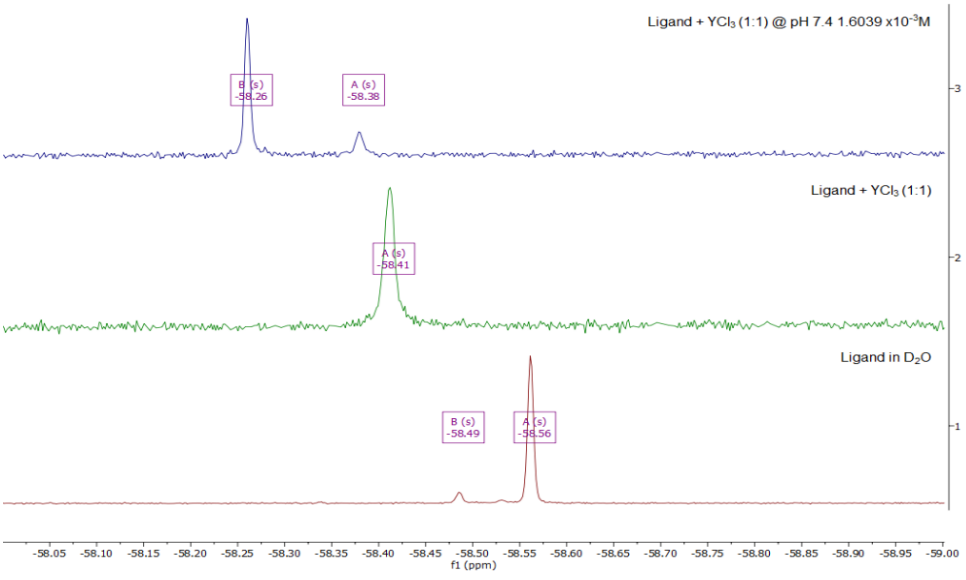

(C)

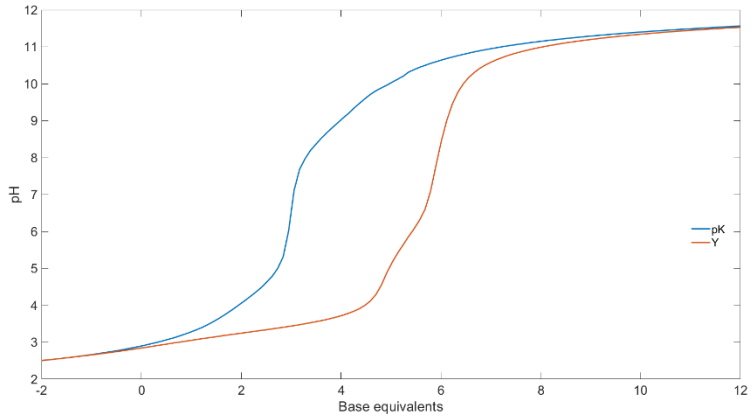

(D)

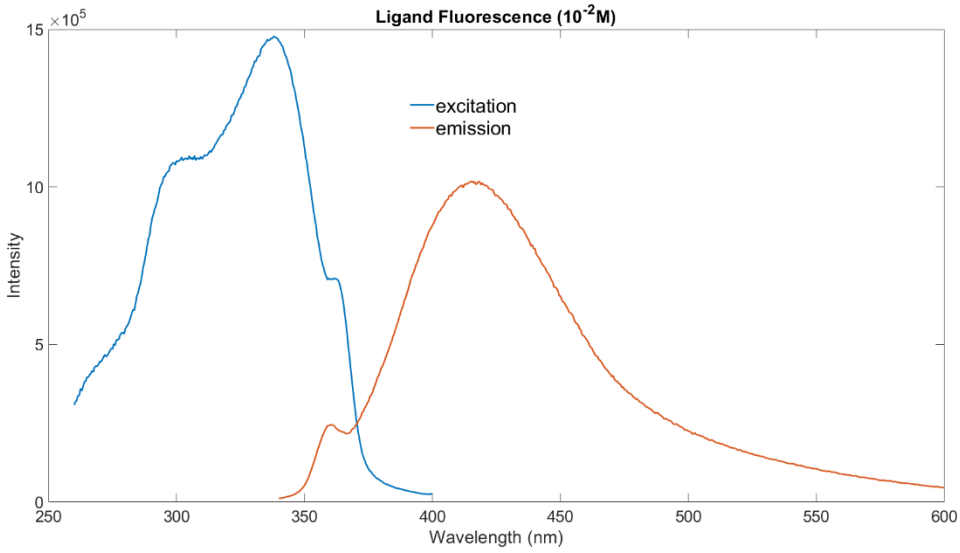

Figure 4.2.2.1. Ligand characterisation, (A) pH-dependent UV-Vis studies, (B) ^{19}F NMR data in D_2O, (C) determine pKa values, and (D) fluorescent data.

4.2.3. Complexation

With the ligand in hand, we directly mixed the ligand and YCl_3 $6H_2O$ in a (1:1) ratio and adjusted the pH to 7.4 with NaOH. It is worth noting that we excluded the use of phosphate buffer to avoid complexation competition (phosphate vs ligand). The complexation is confirmed by comparing the ^1H (Figure 4.2.3.1. A), ^{19}F NMR (Figure 4.2.2.1. B), UV-Vis, maximum at 263nm (Figure 4.2.3.1. B) and ESI-MS (Figure 4.2.3.1. C), suggesting the presence of only one species, thus validating the findings of solution studies. From the ^1H NMR data, two fingerprint areas can be distinguished that show significant changes; the doublet peak at 6.39ppm, shifts at 6.57ppm, while the peak at 8.73ppm, shifts at a lower value at 8.18ppm. Notably, given the asymmetric character

of the ligand, different isomeric forms of the anionic species would be expected to appear; however, the ^{19}F data clearly identify the presence of only one isomer. Then the complexation of the ligand and YCl_3, provides a spectrum with only one single peak at -58.41ppm, significantly shifted compared to the free ligand, while when we adjusted the pH to 7.4, the peak further shifted toat -58.26ppm (0.30 ppm difference compared to the free ligand). Notably, a second minor peak appears at -58.36 ppm; however, this peak may correspond to a differently deprotonated YL complex species (see solution studies species distribution below) or to a different isomer of the targeted [Yoct$^{(p\text{-}OCF3)}$salox]$^-$ complex. Efforts to crystallise the major specie with vapour diffusion of an aqueous solution with acetone produced after four months of a weakly diffracting crystalline material, sensitive to solvent loss; therefore, we were unable to obtain evidence via single crystal X-Ray diffraction.

(A)

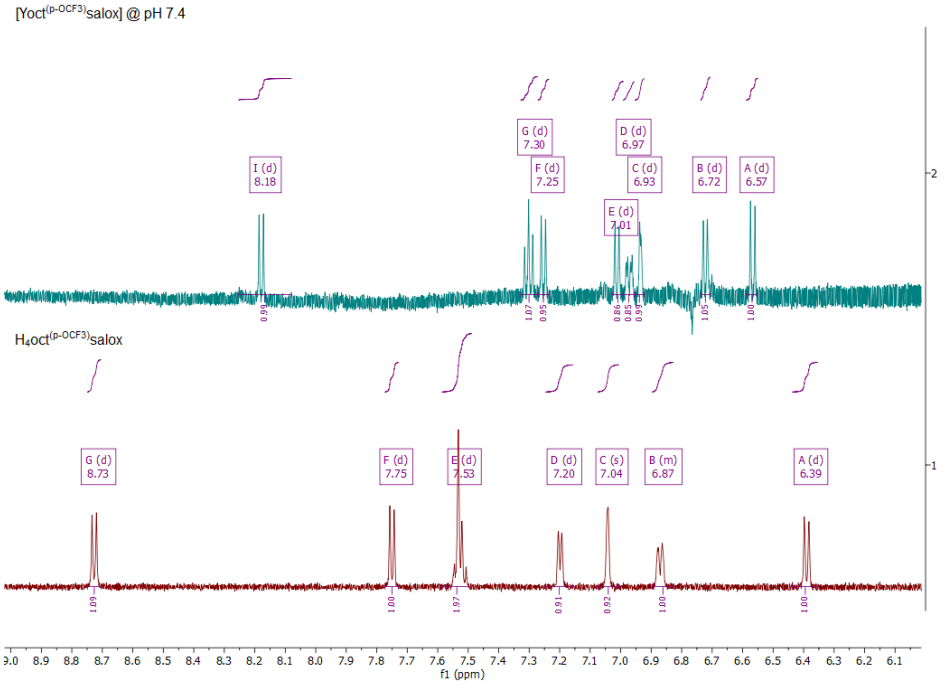

(B)

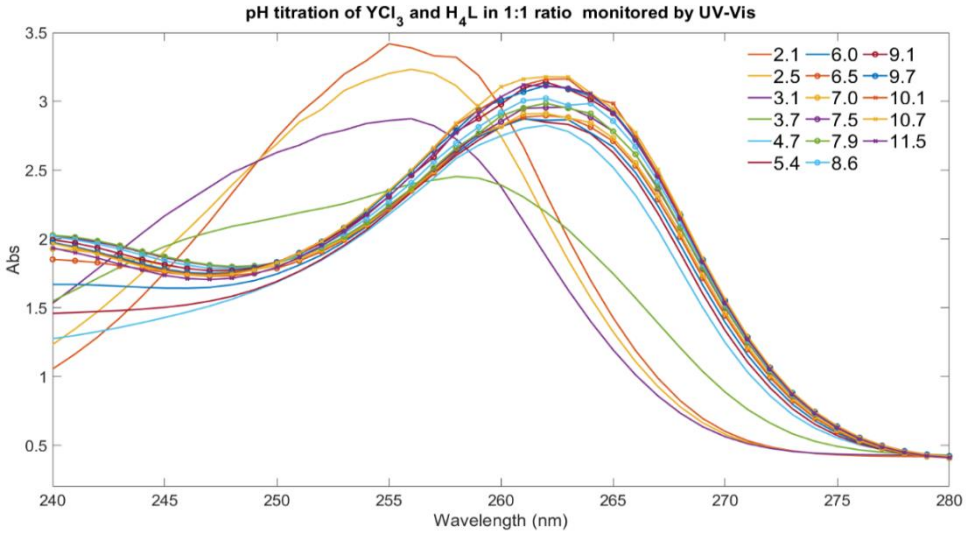

Figure 4.2.3.1. (A) ^{1}H NMR data comparison of the ligands and the [Yoct$^{(p\text{-}OCF3)}$salox]$^{-}$ complex at pH 7.4. (B) pH-dependent UV-Vis studies of the H_4oct$^{(p\text{-}OCF3)}$salox and YCl_3

DFT calculations for structure determination. All calculations were performed using the Gaussian 16 package (Revision C.01).[302] Full geometry optimisations were carried out using the B3LYP hybrid functional[305,343,344] in aqueous solution using the polarisable continuum model (PCM).[345] Geometry optimisations were carried out using the Ahlrichs and co-workers basis set of triple-ζ quality with polarisation functions (Def2TZVP) on all atoms along with corresponding ECP for Yttrium.[346–349] No constraints on symmetry were imposed during the geometry optimisation. The resulting geometries showed no imaginary frequencies and thus were confirmed to be minima on the potential energy surfaces. The same functional, basis set, ECP, and solvent effects were employed for the subsequent NMR calculation using the GIAO method.[350] Calculated ^{19}F absolute shielding constants were converted into ^{19}F NMR chemical shifts scale referenced to C_6H_5F (δ, ppm) using the equation (1), as recommended by the International Union of Pure and Applied Chemistry (IUPAC).[351] From these calculations (Tables 4.2.3.1.-4.2.3.3) it is evident that the axial structure has additional intramolecular hydrogen bonding interactions which could be stabilising the structure more than the equatorial conformation (Figure 4.2.3.2.).

$$\delta = ((\sigma_{C6H5F} - 113.15) - \sigma)/(1 - 10^{-6}(\sigma_{C6H5F} - 113.15)) \quad (1)$$

Where σ_{C6H5F} equals to the absolute shielding constant and -113.15 ppm is the reference value for C_6H_5F. For $CFCl_3$ it would be 0, therefore the equation would be $\delta = ((\sigma_{CFCl3} - 0) - \sigma)/(1 - 10^{-6}(\sigma_{CFCl3} - 0))$.

Screening of DFT methods

Table 4.2.3.1. Screening of basis set[a]

Functional	Basis Set	Solvent	Average %Error[b]
B3LYP	SDD	None	82.0%
B3LYP	SDD	D_2O	76.0%
B3LYP	6-311+G(d,p)//LANL2DZ	D_2O	11.0%
B3LYP	**Def2TZVP**	**D_2O**	**2.0%**
B3LYP	Def2TZVP-D	D_2O	2.2%

a) NMR reference, C_6H_5F, was calculated using the same method in each case. 6-311+G(d,p)//LANL2DZ: The 6-311+G(d,p) basis set was used on first- and second-row elements and the Los Alamos effect core potential (ECP) and valence basis set of double-ζ quality (LANL2DZ) on the Yttrium atom. b) Average %Error is across 8 compounds. The axial and equatorial structures of $H_4oct^{(p\text{-}OCF3)}salox$, $[Yoct^{(p\text{-}OCF3)}salox]^-$ with H_2O, $[Yoct^{(p\text{-}OCF3)}salox]^-$ with GABA amine coordinated, and $[Yoct^{(p\text{-}OCF3)}salox]^-$ with GABA carboxylate coordinated

Table 4.2.3.2. Screening of functionals[a]

Functional	Basis Set	Solvent	Average %Error[b]
B3LYP	Def2TZVP	D_2O	1.97%
BP86	Def2TZVP	D_2O	6.02%
M06	Def2TZVP	D_2O	14.64%
M062X	Def2TZVP	D_2O	2.04%
TPSSh	Def2TZVP	D_2O	11.53%
wB97XD	**Def2TZVP**	**D_2O**	**1.61%**

a) NMR reference, C_6H_5F, was calculated using the same method in each case. b) Average %Error is for the 3 fluorine atoms in the axial structure of $[Yoct^{(p\text{-}OCF3)}salox]^-$ with H_2O.

Table 4.2.3.3. The computed relative stability of axial and equatorial complexes.

Structure	Axial/Equatorial	Analyte[a]	Energy (kJ.mol^{-1})[b]	Difference (eq-ax, kJ.mol^{-1})
$H_4oct^{(p\text{-}OCF3)}salox$	ax	None	-5041447.7	+5.7
$H_4oct^{(p\text{-}OCF3)}salox$	eq	None	-5041442.0	
$[Y(oct^{(p\text{-}OCF3)}salox)]^-$	ax	H_2O	-5337765.9	-7.2
$[Y(oct^{(p\text{-}OCF3)}salox)]^-$	eq	H_2O	-5337773.2	
$[Y(oct^{(p\text{-}OCF3)}salox)]^-$	ax	GABA-O	**-6090624.4**	-3.8
$[Y(oct^{(p\text{-}OCF3)}salox)]^-$	eq	GABA-O	-6090628.2	
$[Y(oct^{(p\text{-}OCF3)}salox)]^-$	ax	GABA-N	-6090626.7	-8.2
$[Y(oct^{(p\text{-}OCF3)}salox)]^-$	eq	GABA-N	**-6090634.9**	

a) GABA-O: GABA coordinated at the carboxylate. GABA-N: GABA coordinated the amine. b) B3LYP/Def2TZVP theory level was used for optimisation, frequency and NMR calculations.

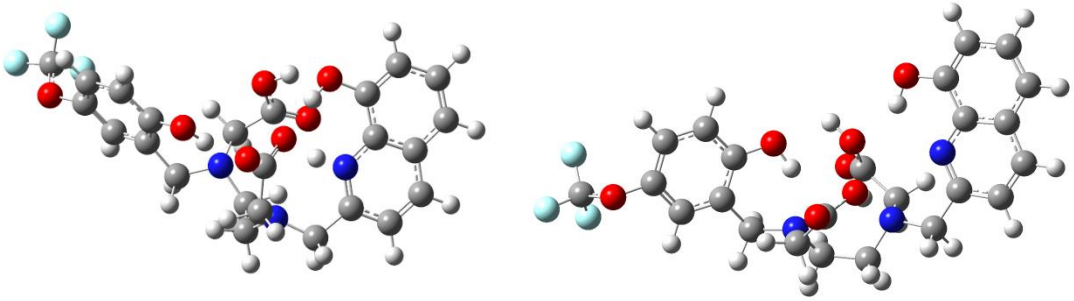

$H_4oct^{(p\text{-}OCF3)}salox$, axial **$H_4oct^{(p\text{-}OCF3)}salox$, equatorial**

Figure 4.2.3.2. Ball stick representation of the two computationally optimised structures at the B3LYP/Def2TZVP theory level for the **$H_4oct^{(p\text{-}OCF3)}salox$**; axial (left) and equatorial (right).

Table 4.2.3.4. Calculated bond distances for both possible conformations of **$H_4oct^{(p\text{-}OCF3)}$salox**. The ligand is shown and numbered.

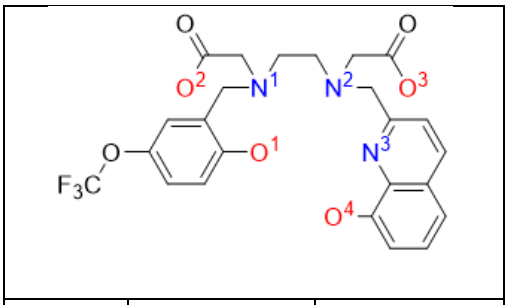

	Distance (ax)	Distance (eq)
O1H-N1	1.8679	1.9316
O2H-O4	1.9757	-
O3H-N3	1.0688	-
O4H-O3	1.6338	2.2462
O2H-N2	-	1.8084

Then we performed DFT studies to elucidate a possible structure for the complex (Figure 4.2.3.3, Table 4.2.3.5). These studies suggest that the equatorial conformation is more stable but also provide evidence that in both structures, the coordination sphere of the Yttrium centre is totally fulfilled by the ligand (coordination number 7), since one lattice water molecule forms hydrogen bonds with oxygen atoms of the ligand.

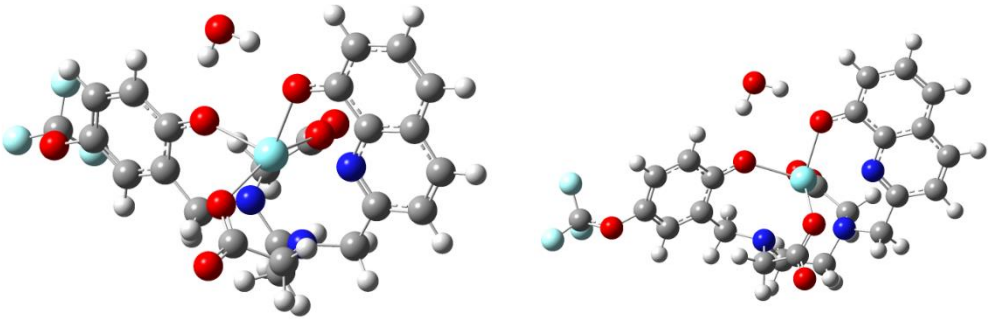

$[Y(oct^{(p\text{-}OCF3)}salox)]^-$, equatorial, H_2O **$[Y(oct^{(p\text{-}OCF3)}salox)]^-$, axial, H_2O**

Figure 4.2.3.3. Ball stick representation of optimised structures at the B3LYP/Def2TZVP theory level for the two **$[Y(oct^{(p\text{-}OCF3)}salox)]^-$, H_2O**, axial (right) and equatorial (left) complexes.

Table 4.2.3.5. Calculated bond distances for both possible conformations of the **[Y(oct$^{(p\text{-}OCF3)}$salox)]$^{-}$** complex. The ligand is shown and numbered to help understand the complexation process and explain the geometry (coordination number 7)

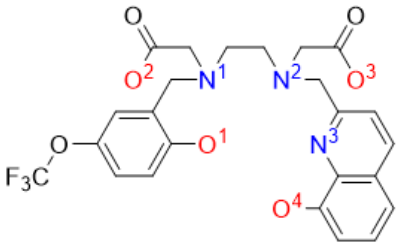

Bond	Distance (ax)	Distance (eq)
Y-N1	2.6218	2.6579
Y-N2	2.6545	2.6976
Y-N3	2.5100	2.5147
Y-O1	2.2296	2.2382
Y-O2	2.2869	2.2662
Y-O3	2.2934	2.2548
Y-O4	2.3036	2.3088
Y….OH_2	3.8278	3.9308

4.2.4. Solution studies.

To identify the stability of the (Yoct$^{(p\text{-}OCF3)}$salox)$^{-}$ complex, we conducted solution studies at different pH values and determined the stability of the monoanionic complex (Table 4.2.4.1). The solution studies were performed by mixing the ligand and $YCl_3\,6H_2O$ in an equimolar ratio. At physiological pH values the monoanionic (Y oct$^{(p\text{-}OCF3)}$salox)$^{-}$ specie is dominant (Figure 4.2.4.1.). UV-Vis, pH-dependant studies of the ligand and the complex confirm the structural changes due to deprotonation but also determine that only one species is formed at physiological pH values. Notably the ^{19}F NMR data (Figure 4.2.2.1B) at pH 5.5. and 7.4 signify a significant difference, possibly due to the existence of complexes with different deprotonated ligands.

Table 4.2.4.1. Protonation constants (logβ) and logK values of the ligand $H_4oct^{(p\text{-}OCF3)}salox$ (I=0.2 M, T=298 K, cL=1 mM, standard deviations are in parentheses) and H_4Octox^{337} for comparison

	$H_4oct^{(p\text{-}OCF3)}salox$		H_4Octox^{337}	
	lgβ	**logK**	**lgβ**	**logK**
HL	10.84(2)	10.84(2)	10.65(1)	10.65
H_2L	20.53(3)	9.69(3)	20.67(1)	10.02
H_3L	28.95(4)	8.42(4)	29.60(1)	9.03
H_4L	33.48(4)	4.53(4)	34.78(1)	5.15
H_5L	36.80(3)	3.32(3)	37.83(1)	3.05
H_6L	38.86(4)	2.06(4)	39.86(2)	2.03
H_7L	n/a	n/a	39.55(8)	-0.31
H_8L	n/a	n/a	38.88(7)	-0.67

Table 4.2.4.2. Stability constants of the complexes formed in the Y^{3+}-$H_4oct^{(p\text{-}OCF3)}salox$ and Y^{3+}-H_4Octox systems (I=0.2 M, T=298 K, cL=1 mM, standard deviations are in parentheses)

	$H_4oct^{(p\text{-}OCF3)}salox$	H_4Octox^{337}
YH_2L	30.05(1)	32.98
YHL	26.70(1)	29.27
YL	20.58(3)	23.78
$YH_{-1}L$		13.17

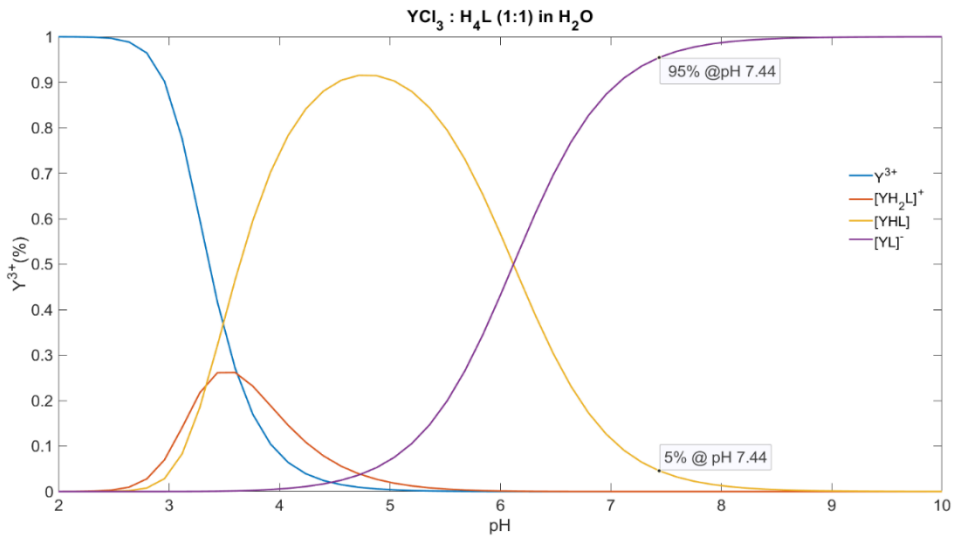

Figure 4.2.4.1. Distribution curves for Y^{3+}- $H_4oct^{(p\text{-}OCF3)}salox$ complex, $[Y^{3+}]$ = $[H_4oct^{(p\text{-}OCF3)}salox]$ = = 1×10^{-3}M.

To identify the bimodal sensing character of the $(Yoct^{(p\text{-}OCF3)}salox)^-$, we attempted to elucidate its fluorescence response in aqueous media at different concentrations. Different fluorescent mechanisms (photoinduced proton or electron transfer) are well

established for the hydroxyquinoline group,[352,353]; however, the chelation-enhanced fluorescence (CHEF) of the corresponding Y^{3+}complex has been observed in Orvig's pioneer work.[337] Notably, from our data, a CHEF fluorescent mechanism is in place, providing a clearly impacted spectrum with a peak maximum of 550nm. (Figure 4.2.4.2.). Bearing in mind that monitoring should occur at lower concentrations, we recorded the fluorescent data up to three orders of magnitude less concentrated solutions.

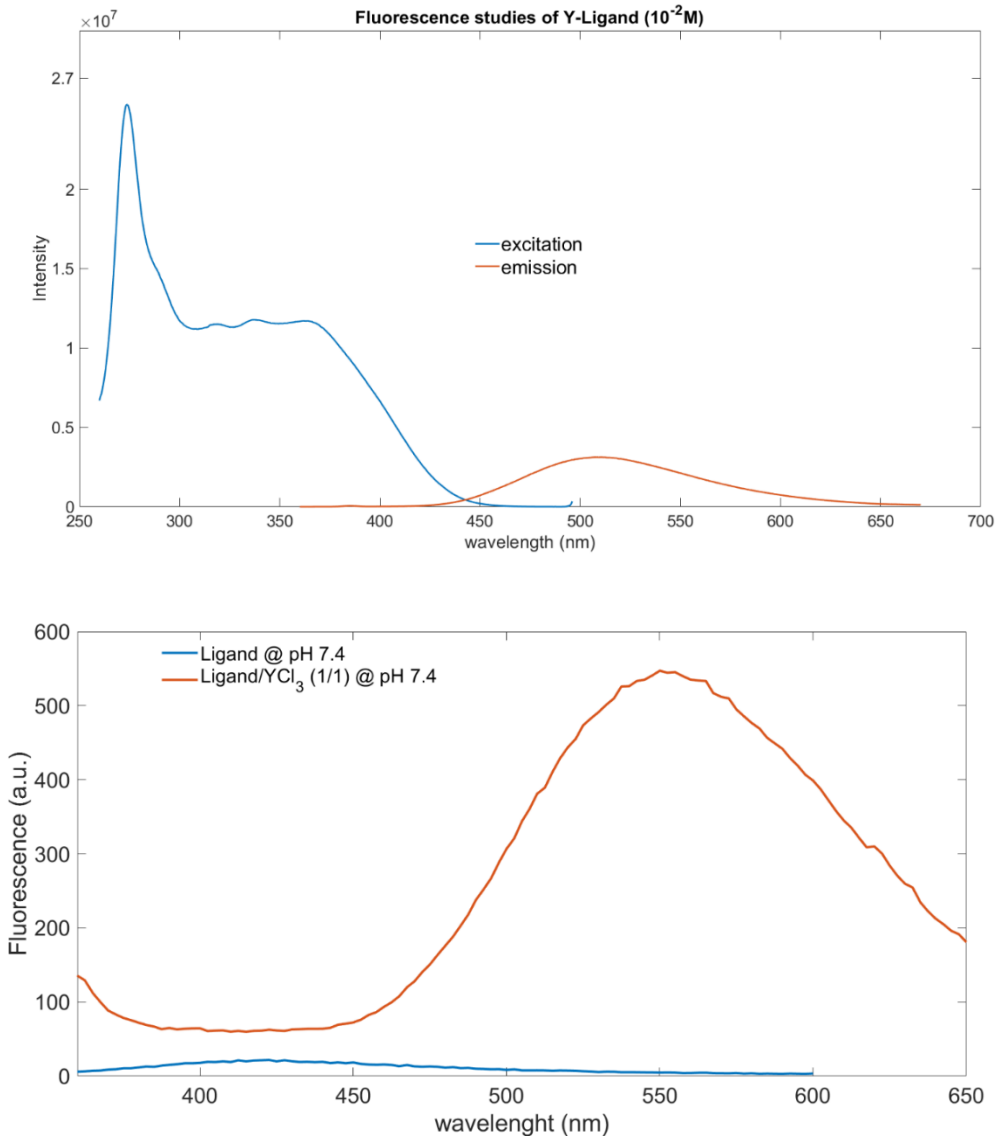

Figure 4.2.4.2. (up) Excitation and emission spectra of $(Yoct^{(p\text{-}OCF3)}salox)^-$ complex at pH = 7.4 (λ_{exc} = 320 nm, at 1.6039×10^{-2} M). (down) Emision spectra of $H_4oct^{(p\text{-}OCF3)}salox$ and $(Yoct^{(p\text{-}OCF3)}salox)^-$ complex at pH = 7.4 (λ_{exc} = 320 nm, at 1.6039×10^{-3} M).

4.2. 5.. In vitro GABA sensing

After completing the characterisation of the $(Yoct^{(p\text{-}OCF3)}salox)^-$ complex and evaluated its toxicity, we started titration experiments with GABA varying the ratio from 1:1 to 1:500. A stock solution of $(Yoct^{(p\text{-}OCF3)}salox)^-$ with a known concentration (1.63069×10^{-3}M) was used to prepare the corresponding samples and the plausible $(Yoct^{(p\text{-}OCF3)}salox)^-$/GaBA interaction(s) was monitored with ^1H (Fig 4.2.5.1 A) and ^{19}F NMR (Fig 4.2.5.1. B), UV-Vis (Fig 4.2.5.1. C) and fluorescence (Fig 4.2.5.1. D). As anticipated, the ^1H NMR data (Fig 4.2.5.1. A) are inconclusive without noticing a significant shift, however, they validate the stability of the complex during these titrations. By varying the temperature of the experiment no further modifications are observed. The ^{19}F NMR data were recorded at 37°C (Fig 4.2.5.1. B). These data show that the complex retains its stability during titrations, and interaction occurs between the complex and GABA, as the unique fluorine peak broadens. This peak broadening has been seen in other biological-related examples[184] and has been suggested that different types of interactions occur. The excess of GABA (1:500) results, possibly in forming a Y-GABA complex, as the peak shifts to -58.40 ppm. The UV-Vis studies identify the disappearance of the second peak at 263nm upon GABA addition; however, these data cannot provide further mechanistic evidence. Last, titration studies to monitor the impact of GABA with fluorescence identify, to our delight, a partial (42%) quench of the prominent peak (max 550nm) at a ratio of 1:1. Upon GABA increase (1:150) the quenching decreases by (30%).

(A)

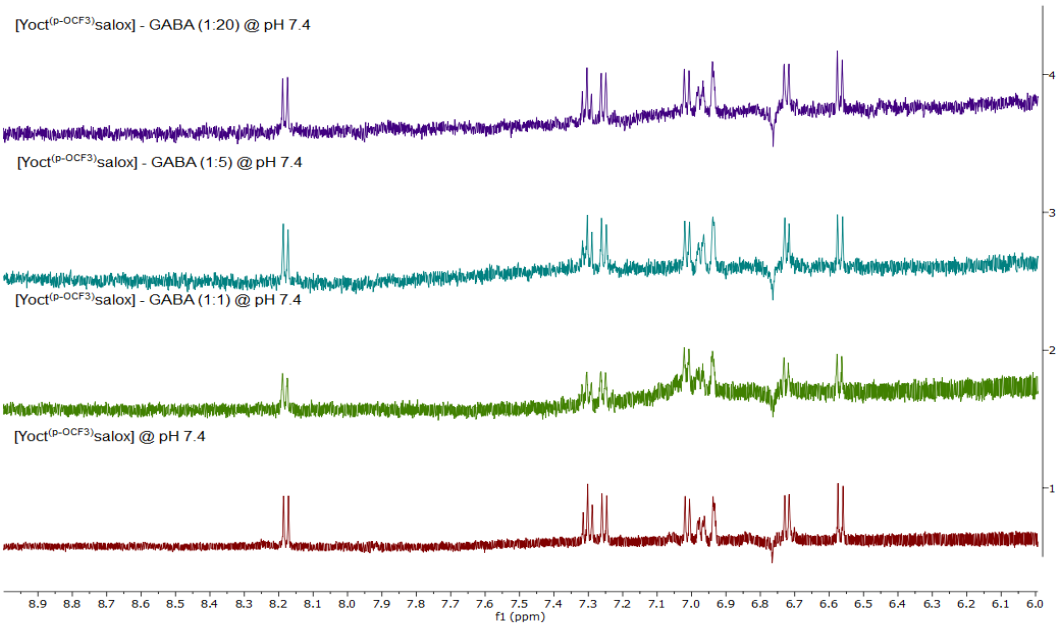

(B)

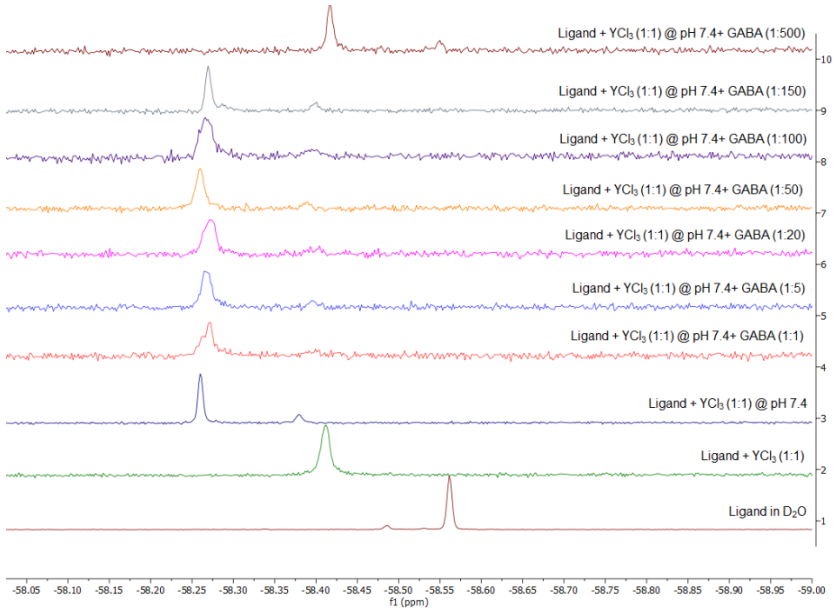

(C)

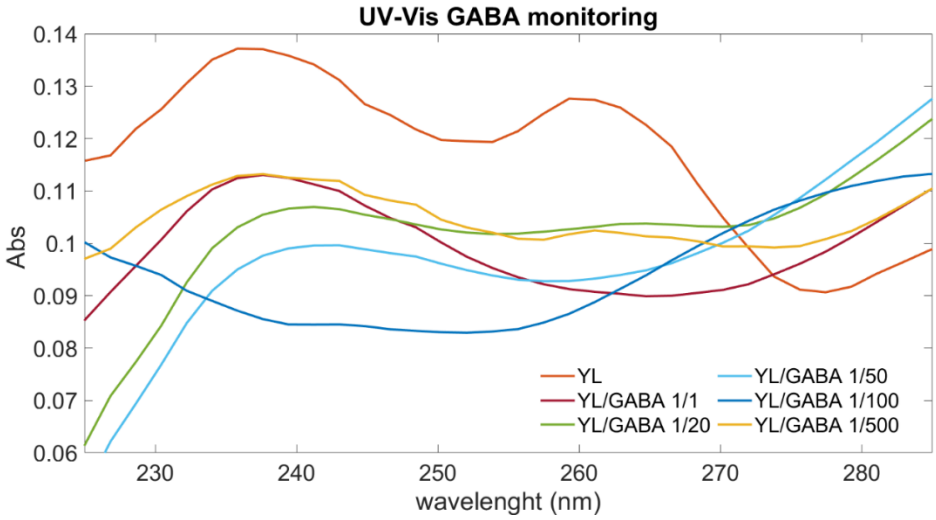

(D)

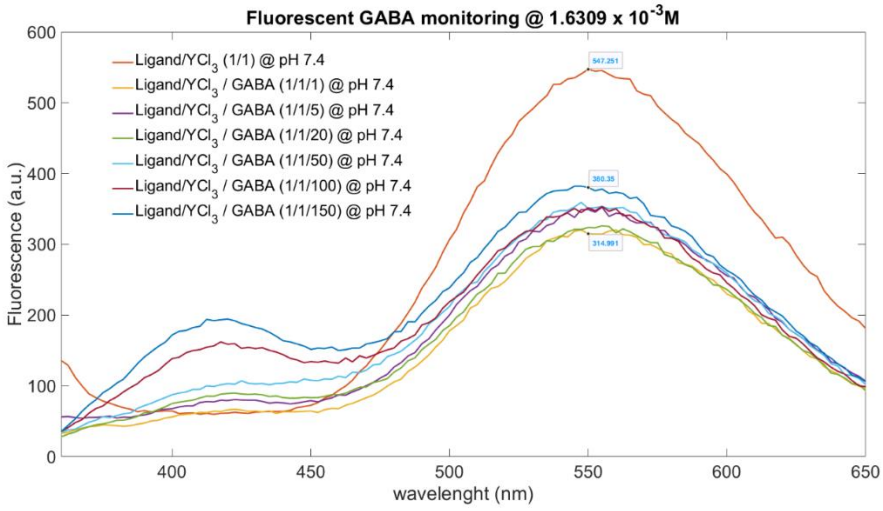

Figure 4.2.5.1. $(Yoct^{(p\text{-}OCF3)}salox)^-$ / GABA interaction monitoring with (A) ^1H NMR data in D_2O, (B) ^{19}F NMR data in D_2O, (C) UV-Vis (D) fluorescent data (λ_{exc} = 320 nm). All measurements were performed at a specific concentration of 1.6039×10^{-3} M.

4.2.6. Other NT sensing

We performed additional studies with other NTs of similar (acetylcholine, AC) or completely different (serotonin, SER) frameworks to understand the nature of the (Yoct$^{(p\text{-}OCF3)}$salox)$^{-}$ / GABA interaction (Figure 4.2.6.). Different behaviour is observed from these data; for AC and SER, the ^{19}F NMR peak remains sharp, while a second minor peak appears at -58.40ppm. The fluorescence data identify different types of interaction(s); for SER, the spectrum is oversaturated (320-400nm), thus, a different excitation wavelength or less concentrated solutions are required, while for AC, an enhanced quenching is observed. At less concentrated solutions, though, the oversaturated behaviour for the SER sample remains. In contrast, a similar quenching is observed for the GABA and AC data, indicating that at these low concentration levels (Yoct$^{(p\text{-}OCF3)}$salox)$^{-}$ is not selective towards GABA.

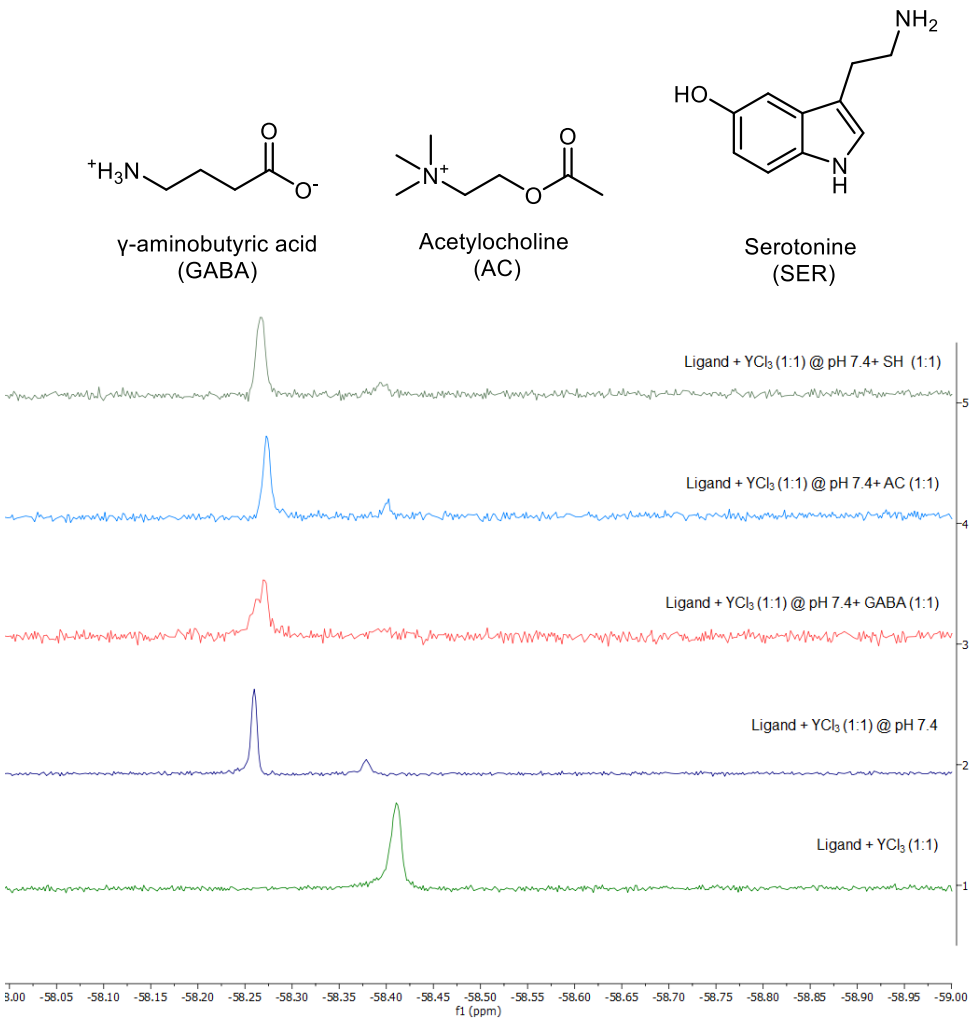

Figure 4.2.6. ^{19}F-NMR sensing of complex and NTs at pH = 7.4

4.2.7. DFT studies for ^{19}F NMR data

To explain the exciting findings in the ^{19}F NMR titration studies, we performed DFT calculations to identify the favourable complex-GABA conformation. We accounted for two different ways that $(Yoct^{(p\text{-}OCF3)}salox)^-$ could interact with GABA. The first considers the covalent bonding of the complex with the oxygen atoms of the carboxylate group, and the second covalent bonding with the N atom of the NH_3 group. For both scenarios, we performed calculations for both conformations (axial and equatorial). The data suggest that the equatorial structures are more stable (Table 4.2.3.3.). For the first scenario, in the axial structure (Figure 4.2.7.1. A), NH_3 of GABA forms one H-bond, which forces the complex into a twisted structure where the two aromatic rings do not lie along the same plane. The same finding could be observed in the equatorial structure (Figure 4.2.7.1. B). However, deviation from flatness is to a lesser degree. The GABA analyte curls back on itself and is more stable according to calculations than the GABA analyte extended away from the complex. For the second scenario, the NH_3 from GABA does not form a covalent bond but forms two hydrogen bonds instead. According to this data (Table 4.2.3.3), the structure in which the analyte (NH_3) forms hydrogen bonding interactions with the complex (Figure 4.2.7.1. D) is the most stable. However, when we account for the calculations for the observed ^{19}F NMR data (Table 4.2.3.5.), then the interaction of the complex with GABA via covalent bonding (Y-O, formation) is closer to the observed data -58.27ppm (-57.28ppm calculated). The calculated shifts for the remaining three interactions are near (-57.14 and -57.11ppm). Calculations at B3LYP/wB97XD level, which account for intramolecular interactions, may improve the accuracy of the present data; however, given that the average error is small, we may propose that the observed difference in the ^{19}F NMR data is due to the H-bonding interaction of the NH_3 group with the complex (Figure 4.2.7.1, lower right). This indicates that the interaction of the complex and GABA at physiological conditions (pH 7.4) in aqueous media is via hydrogen bonding and not covalent bonding (Figure 4.2.7.1, lower left).

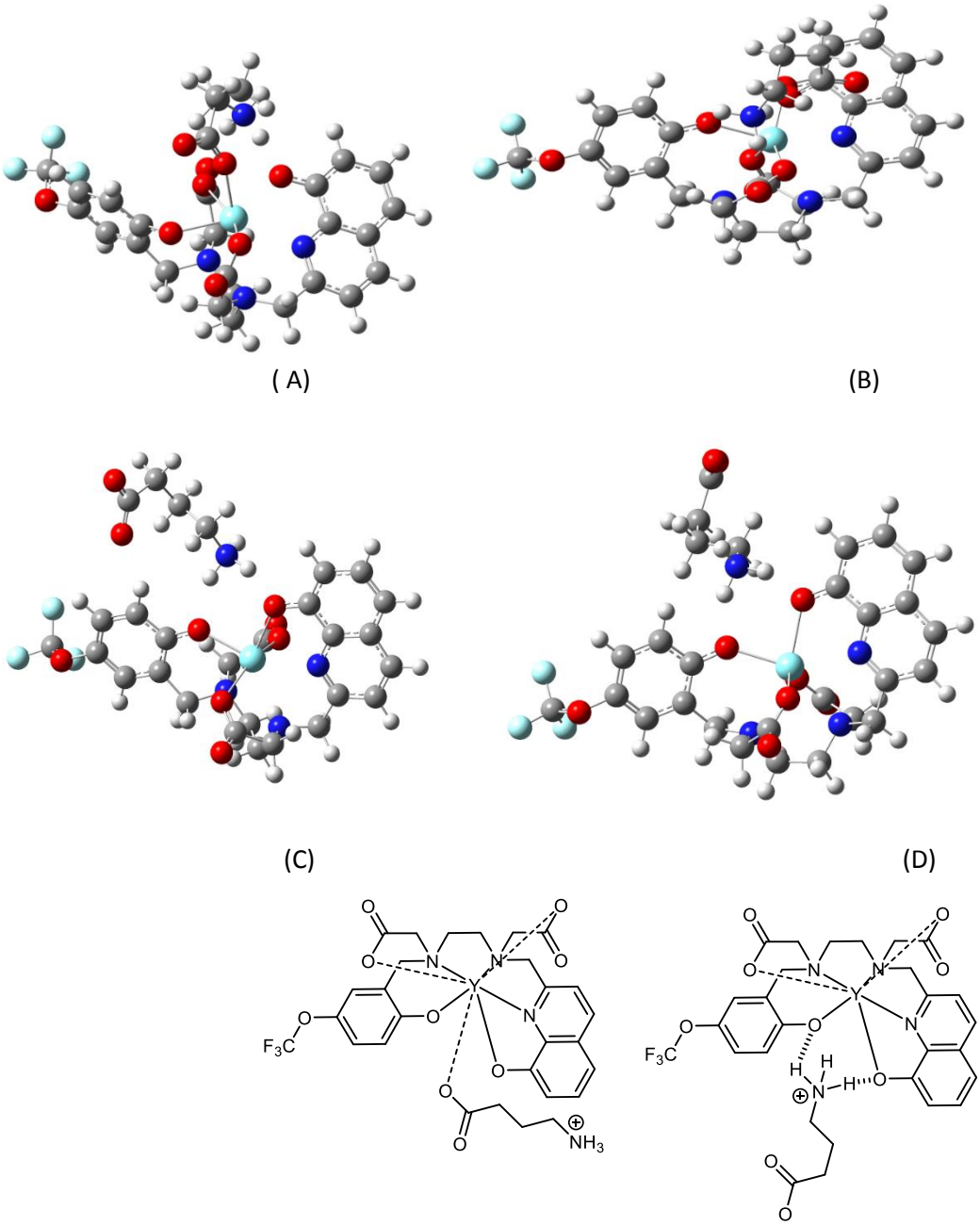

Figure 4.2.7.1. Ball stick representation of optimized structures at the B3LYP/Def2TZVP theory level for **[Y(oct$^{(p\text{-}OCF3)}$salox)]$^{-}$, axial, GABA-O** (A) and **[Y(oct$^{(p\text{-}OCF3)}$salox)]$^{-}$, equatorial, GABA-O** (B) **[Y(oct$^{(p\text{-}OCF3)}$salox)]$^{-}$, axial, GABA-N** (C) and **[Y(oct$^{(p\text{-}OCF3)}$salox)]$^{-}$, equatorial, GABA-N** (D). (Lower) Chemical drawing explaining the interaction of the complex with GABA

Table 4.2.7.1. Calculated bond distances for both possible conformations of **Y(oct$^{(p\text{-}OCF3)}$salox)]$^-$, axial, GABA-O** and **[Y(oct$^{(p\text{-}OCF3)}$salox)]$^-$, equatorial, GABA-O**. The ligand is shown and numbered

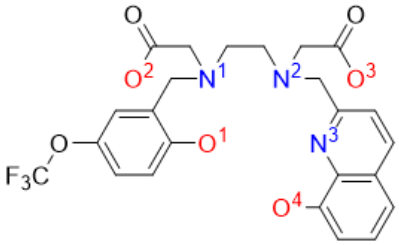

	GABA-O		GABA-N	
Bond	**Distance (ax)**	**Distance (eq)**	**Distance (ax)**	**Distance (eq)**
Y-N1	2.7654	2.8394	2.5851	2.6477
Y-N2	2.8245	2.7321	2.6248	2.6718
Y-N3	2.6483	2.5203	2.4925	2.5075
Y-O1	2.2596	2.2003	2.2392	2.2689
Y-O2	2.3463	2.3586	2.2854	2.2560
Y-O3	2.3364	2.3077	2.2929	2.2501
Y-O4	2.4408	2.3265	2.3212	2.3288
Y-Analyte-X	2.2757	2.5101	3.7707	3.9232

Table 4.2.7.2. Computed ^{19}F NMR chemical shifts.

Structure	Axial/Equatorial	Analyte[a]	Experimental Shift (ppm)	Calculated Shift (ppm)[b]	Average Error (ppm)	Average % Error
H_4oct$^{(p\text{-}OCF3)}$salox	ax	None	-58.56	-57.15	1.41	2.4 %
H_4oct$^{(p\text{-}OCF3)}$salox	eq	None	-58.56	-57.20	1.36	2.3 %
[Y(oct$^{(p\text{-}OCF3)}$salox)]$^-$	ax	H_2O	-58.26	-57.11	1.15	2.0 %
[Y(oct$^{(p\text{-}OCF3)}$salox)]$^-$	eq	H_2O	-58.26	-57.20	1.06	1.8 %
[Y(oct$^{(p\text{-}OCF3)}$salox)]$^-$	ax	GABA-O	-58.27	-57.28	0.99	1.7 %
[Y(oct$^{(p\text{-}OCF3)}$salox)]$^-$	eq	GABA-O	-58.27	-57.14	1.13	1.9 %
[Y(oct$^{(p\text{-}OCF3)}$salox)]$^-$	ax	GABA-N	-58.27	-57.11	1.16	2.0 %
[Y(oct$^{(p\text{-}OCF3)}$salox)]$^-$	eq	GABA-N	-58.27	-57.14	1.13	1.9 %
				Average:	**1.18**	**2.0 %**

a) GABA-O: GABA coordinated at the carboxylate. GABA-N: GABA coordinated the amine.
b) B3LYP/Def2TZVP theory level used for optimisation, frequency and NMR calculations. NMR reference, C_6H_5F, was calculated using the same method.

Lastly, to identify the limitations of each spectroscopic technique for monitoring, we recorded ^{19}F NMR data of further diluted samples (1.6039×10^{-4} M and 1.6039×10^{-5} M) and, as anticipated, at deficient concentrations, no signal can be observed (Figure 4.2.7.2).

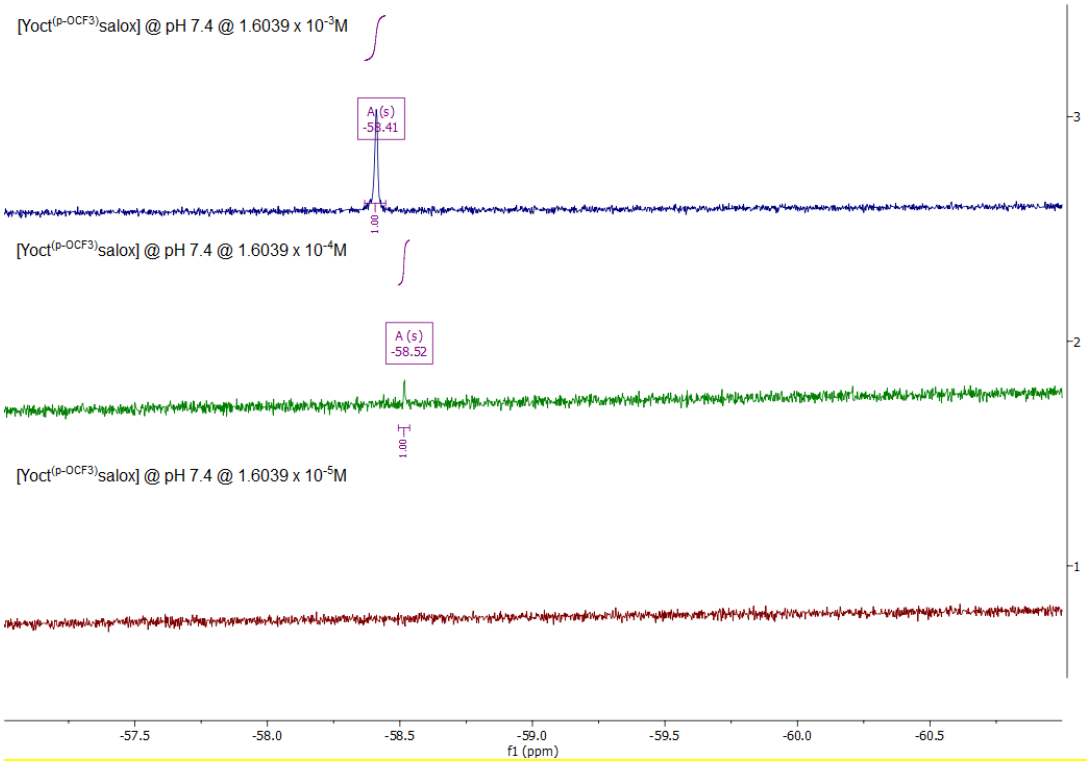

Figure 4.2.7.2. ^{19}F NMR data of $(Yoct^{(p\text{-}OCF3)}salox)^-$ / GABA in ratio 1:1 at different concentrations.

4.3. Conclusions

The facile and inexpensive heptandentate $H_4oct^{(p\text{-}OCF3)}salox$ ligand provides access to a molecular entity $[Yoct^{(p\text{-}OCF3)}salox]^-$ that can be used for multimodal monitoring purposes of GABA NT. *In vitro* monitoring with UV-Vis, ^{19}F NMR and fluorescence and DFT calculations allow for mapping complex/NT interaction and rationalising a possible selective sensing mechanism at a specific concentration. This work opens new research directions in coordination and bioinorganic chemistry by introducing a molecular sensor with immediate application in neuroscience.

5 Chapter 5: Molecular fluorine-based probes for heavy metals ion detection

Abstract. We report an array of novel symmetric and asymmetric ligands with their fluorine-based Zn-salan complexes to sense HMIs with ^{19}F NMR. Investigations shows that Cd^{2+} and Pb^{2+} ions can be sensed and detected using DMSO-H_20 media.

External Contributions: A. Galvácsi and C. Kállay performed solution studies and ^{19} F NMR titration measurements with HMIs.G E. Kostakis performed and evaluated the crystallographic data. Maria Besora performed theoretical calculations. All authors contributed to the preparation of the article.

5.1. Introduction

The Niger Delta aqueous media region has witnessed contamination over the years, significantly imminently affecting daily livelihood and sustenance,[223,224] and ultimately human security, recreation and fisheries, thus imposing water quality regulations and monitoring methods.[225] Mercury, Lead, Arsenic, Cadmium and Chromium are the predominant heavy metal ions (HMIs) contaminants according to the World Health Organization (WHO) standards.[226] To overcome this obstacle, various methods have been proposed to capture and remove HMIS from aqueous media.[201] These technologies include but are not limited to using porous materials such as Metal-Organic Frameworks (MOFs),[108,202,203] zeolites,[204–206] biological matter like sorghum and maize waste,[354,355] hydrogels[207,208] sulphur-based nanosheets[209] or silica-based components as the absorbents.[210,211] Currently, methods incorporating MOFs as absorbents dominate these studies; however, developing an efficient, convenient, selective and practical capture technology in which the capturing mechanism is well understood remains a big challenge.

Salan ligands are the reduced version of the organic framework produced by the condensation reaction between salicylaldehyde and ethylenediamine (Figure 5.1.1, left). These ligands are easily accessible and modifiable and offer a specific pocket size for coordination; thus, their complexes have inevitably found applications in catalysis, sensing, and medicinal chemistry.[42,227,236–243,228–235] Salan-based MOFs have found application in catalysis,[356–358]; however, they have never been used to sense or remove HMIs. The majority of these scaffolds impose a tetradentate N_2O_2 pocket, and only a few

paradigms of asymmetric N_2O_2 ligands and their corresponding complexes are known.[36,359–361] We recently reported a convenient protocol for asymmetric N_2O_2 salans.[36] This method gives access to numerous ligands and corresponding complexes with chemically modified peripheries which can be used for structural activity relationship studies (SARS). On the basis that these complexes hold the same formula-structure, then the presence of different functional groups becomes a valuable tool and permits chemical mapping of the interaction(s) between the complex and the environment (solvent, analyte, substrates etc.) with various techniques such as NMR, IR, UV-Vis, Fluorescence, thus these SARS can extrapolate useful information and underpin mechanisms.

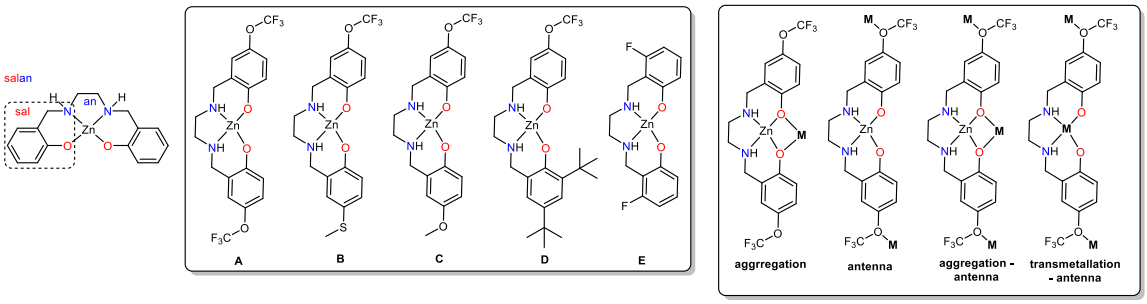

Figure 5.1.1. (left) The salan framework, (middle) the targeted A- E complexes, (right) possible HMIs-complex interactions.

Nuclear Magnetic Resonance (NMR) is a spectroscopic technique that observes local magnetic fields around atomic nuclei. ^{1}H and ^{19}F NMR are the most common techniques used for kinetic studies; however, in the latter case, the environment (solvent, ligands, substrates etc.) is silent unless it contains F atoms. Therefore, its use to monitor interaction(s) between complexes and the environment becomes convenient. Taking all these into account, we envisaged that salan-based molecules would be an economically viable and convenient method to remove HMIs. However, given the currently limited information and before attempting to anchor the metallo-salan frame within a MOF entity, we hypothesised that SARS monitored by ^{19}F NMR of a family of symmetric and asymmetric Zn-salan complexes (**A** to **E**, Figure 5.1.1. middle) and HMPs would underpin their interaction(s). We detailed herein our selection criteria for these sets on the basis that these compounds will exist as monomers in aqueous media. Set **A** is designed to be sensing and monitoring from both sides. Set **B** will permit monitoring from one side, whereas the S heteroatom imposes the removal of H-bonding interactions. Set **C**

provides the same frame as **A**, but only one side can be used for monitoring. Set **D** incorporates bulky groups imposing steric effects; thus, possible interactions can be excluded. Last, set **E** consists of a different antenna, position, and group (F vs OCF_3), and a different monitoring process is subsequently anticipated. The interaction between the complex and HMPs may occur via the following, but not limited to, methods: coordination (aggregation, antenna, aggregation–antenna) and transmetallation (Figure 5.1.1, right). These complexes are envisaged to crystallize as dimers and adopt different structures in solution, especially those built from the asymmetric salan ligands (Figure 5.1.2), as Di Bella has explicitly described in this process.[233] These different forms and their equilibrium may interfere chronically with the sensing process. This work aims to validate or discard this notion, and the results of this SARS are presented herein.

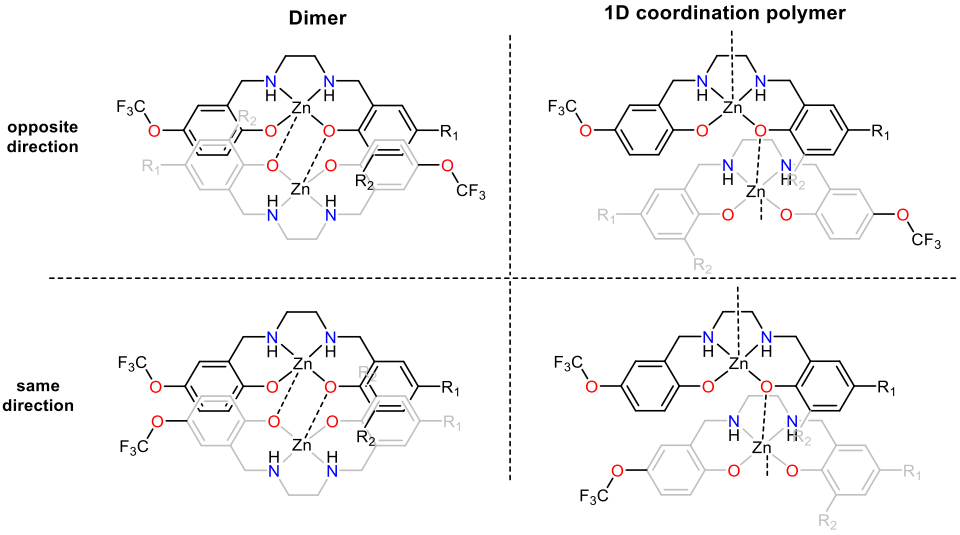

Figure 5.1.2. Possible structures and orientations for asymmetric Zn-salan complexes.

5.2. Results and Discussion

The symmetric ligands (**A** and **E**) can be synthesised in one step, with yields of 96% and 82%, respectively, that involves the condensation reaction of ethylenediamine and the corresponding salicylic aldehyde, followed by reduction with $NaBH_4$. In contrast, the asymmetric ligands can be synthesised via a three-step synthesis. The latter involves the synthesis of the OCF_3 precursor in a multigram scale followed by condensation and reductive amination. The OCF_3/OCF_3 ligand (**A**) can be obtained with both methods; however, method (g) is convenient. All ligands can be obtained in high yields. The total yield for ligand **B** (SCH_3/OCF_3) is 53%, for **C** (OCF_3/OCH_3) is 54% and for **D** (OCF_3/BisBut) is 40%.

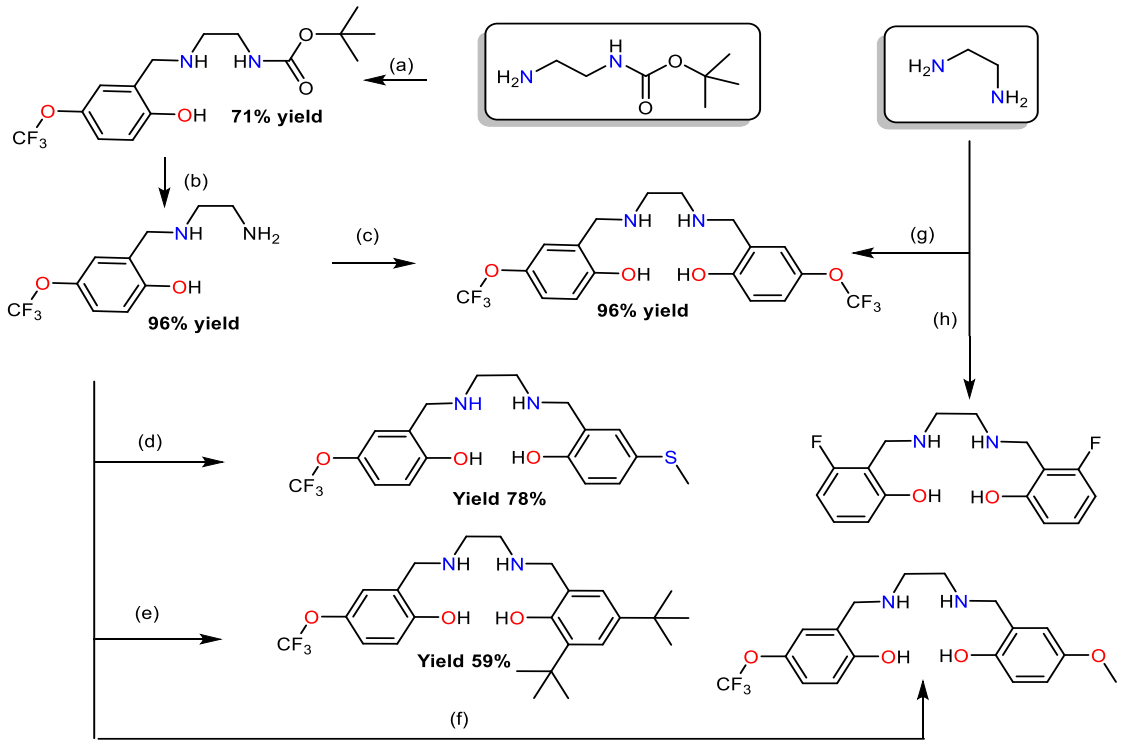

Figure 5.2.1. A general procedure for the synthesis of the asymmetric and symmetric N_2O_2 ligands. **(a)** 2-hydroxy-5-trifluoromethoxy benzaldehyde (1eq), MeOH and adding tertiary butyl carbamate (1eq) reflux (24hr), $NaBH_4$ (3eq), 2 hr (89%); **(b)** 4NHCl in Dioxane/CH_2Cl_2, 24 hr, (96%); **(c)** (b) (1eq), MeOH, 2-hydroxy-5-trifluoromethoxy benzaldehyde (1eq), reflux(2hrs),0.1g molecular sieves, $NaBH_4$ (3eq) 2hr (96%); **(d)** 4-methyl thiol phenol(1eq), paraformaldehyde(6.75eq), anhydrous magnesium chloride(1.5eq) and Et_3N (3.75eq), CH_3CN, reflux,(24hrs), column chromatography(Hex 8: Ethyl acetate 2), Combine with (b)(1eq), MeOH,0.1g molecular sieves, 2hr, $NaBH_4$ (3eq) 2hr (78%); **(e)** (b) (1eq), MeOH, 3,5-Di-Tertiary Butyl-2-hydroxybenzaldehyde(1eq), reflux(2hrs),0.1g molecular sieves, $NaBH_4$ (3eq) 2hr (59%); **(f)** (b) (1eq), 2-hydroxy,5-methoxybenzaldehyde(1eq),), reflux(2hrs),0.1g molecular sieves, $NaBH_4$ (3eq) 2hr (89%); **(g)** 2-hydroxy-5-trifluoro methoxy benzaldehyde (2eq), MeOH, ethylenediamine(1eq), reflux (2hrs), $NaBH_4$ (3eq), 2 hr (96%); **(h)** 6-Fluro,2-hydroxybenzaldehyde(2eq), MeOH, ethylenediamine(1eq), reflux (2hrs), $NaBH_4$ (3eq), 2 hr (82%);

With the ligands in hand and bulk, we performed several reactions for synthesising the corresponding Zn^{2+} complexes. We screened several parameters such as metal salts $Zn(NO_3)_2$ $6(H_2O)$, $ZnCl_2$, $Zn(OTf)_2$, $Zn(BF_4)_2$, $Zn(ClO_4)_2$, solvents (MeOH, CH_2Cl_2, EtOH, CH_3CN), metal : ligand ratio (2:1 to 1:2), temperature (25°C & 75°C), base (Et_3N, Na_2CO_3, K_2CO_3) and identified the optimum conditions as : $Zn(NO_3)_2$ $6(H_2O)$: Ligand : Na_2CO_3 in a molar ratio 1:1:1 on a mixture of solvents MeOH/H_2O (10/2mL). The metal salt and ligand were dissolved in methanol, and the solution turned milky upon adding an aqueous Na_2CO_3 solution. After 1 hr of reflux, the solution was filtered, and

the filtrate was kept for slow evaporation; shiny block-shaped colourless crystals were obtained between two and five days. The yield of the complexation reaction varies between 39 to 53%.

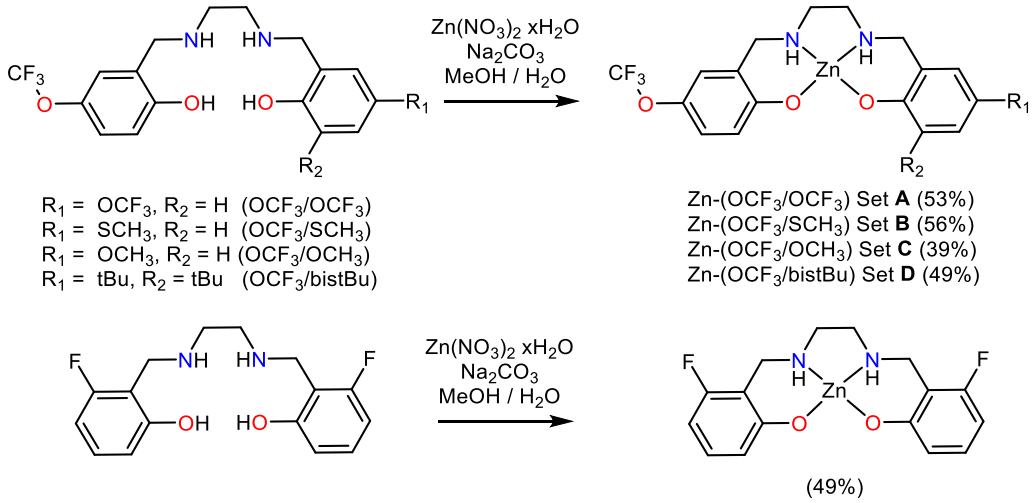

Figure 5.2.2. A general approach for the synthesis of the Zn-salan complexes.

5.3. Characterisation in the solid state.

Single crystal X-Ray diffraction studies (Table 5.3.1) reveal a general dimeric formula [(Zn_2L_2) x(solvent)], where x is 4(CH_3OH) for sets **A** and **D** and 2(CH_3OH) for set **B** (Figure 5.3.1.). Preliminary crystallographic data for set **C** suggest that this compound crystallises as a one-dimensional coordination polymer (Figure 5.1.2, right); however, the crystals are weakly diffracting even in a Synchrotron source; therefore, we were unable to elucidate its structure. Set **E** that incorporates a symmetric ligand crystallises without lattice molecules. Notably, for set **B,** the asymmetric Zn-salan complex crystallises with the OCF_3/SCH_3 groups pointing in the same direction (Figure 5.1.2). It is worth noting that complexation reactions for all five sets were simultaneously performed and left for crystallisation under the same conditions; therefore, this crystallographic evidence pinpoints the formulation complexity (dimensionality and ligand orientation) on the present SARS. Specifically for the asymmetric complexes, three different species are formed; dimer-same orientation (set **B**), 1D coordination polymer (set **C**) and dimer–opposite orientation (set **D**). In all cases, except set **C**, large block crystals were formed, which were then used for crystallographic studies, and no other type(s) of crystals were found. In all cases, the lattice solvent molecules interact via H-bonds with the complexes. The coordination number around the Zn centre is five. The geometry of the Zn centre can be described as square pyramidal for sets **A**, **B** and **E**

and trigonal bipyramidal for set **D** (Table 5.3.1). As anticipated, the tert-butyl bulky groups impose steric hindrance, and the geometry of the metal centre significantly deviates. Thermogravimetric (TG) and elemental (CHN) analysis further characterised the compounds in the solid state. Results for both studies differ from the expected calculated values from the crystallographic analysis (Tables 5.3.2. & 5.3.3). They are consistent with additional lattice solvent molecules, indicating that these complexes are susceptible to absorbing moisture upon storing (Figure S4-36.). This notion suggests that the morphology of these molecular species may change, thus, we didn't perform PXRD studies.

Table 5.3.1. Selected Bond distances for all complexes and originality index

	Zn-O1	Zn-O2	Zn-O3	Zn-N1	Zn-N2	Trigonality index (τ)[299]
Set A	2.057(3)	2.068(3)	1.963(3)	2.110(4)	2.141(3)	0.17
Set B	2.079(7)	1.987(7)	1.990(8)	2.132(8)	2.186(8)	0.29
Set C	1.985(8)	2.108(7)	1.987(7)	2.101(8)	2.189(8)	
Set D	2.088(5)	2.002(5)	1.981(6)	2.132(7)	2.190(6)	0.64
Set E	1.995(5)	2.086(5)	1.966(6)	2.194(7)	2.126(8)	0.33

The Trigonality index indicates the geometry of the coordination center.[299] When τ = 0 the geometry corresponds to square pyramidal, when τ= 1 corresponds to trigonal bipyramidal.

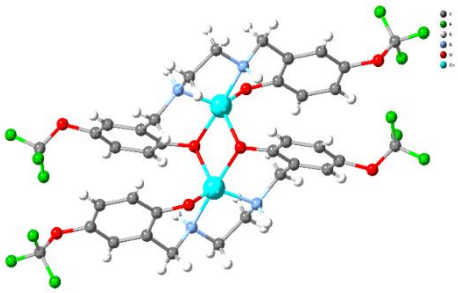

Zn-OCF$_3$-OCF$_3$

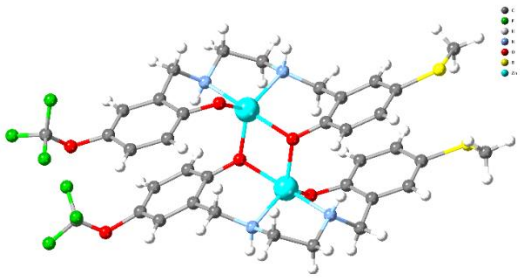

Zn-OCF$_3$-SCH$_3$

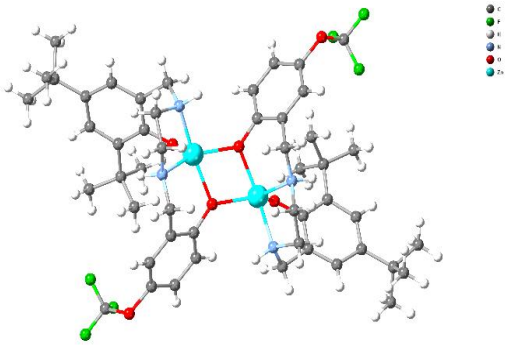

Zn-OCF$_3$-bistBu

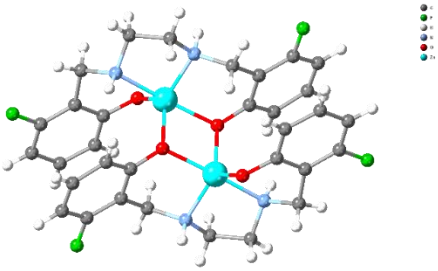

Zn-F-F

Figure 5.3.1. Crystallographic representation of all compounds. Lattice solvent molecules have been omitted for clarity. Colour code; Zn (light blue), O (red), N (blue), C (grey), H(white), F (green), S (yellow).

Elemental analysis results for all complexes were recorded at London Metropolitan University. The samples, upon crystallisation, were filtered, dried and collected (Table 5.3.2.). The samples were stored in Eppendorf. There is a deviation in the data; we assume this deviation is caused by losing their crystallinity and absorbing moisture from the atmosphere, therefore, we provide an estimated formula that matches the experimental values. Our assumption is further supported by thermogravimetric analysis, see below. The expected lattice solvent molecule loss (up to 130^{o}C) is higher than expected, thus an estimated formula is given in (Table 5.3.3.)

Table 5.3.2. Elemental analysis results explanation. Underneath the formula, the corresponding formula that matches the CHN analysis is given for immediate comparison.

Compound	Formula	Calculated(%)			Found(%)			Corresponding(%)		
		C	H	N	C	H	N	C	H	N
Set A	$C_{40}H_{48}F_{12}N_4O_{12}Zn_2$ $C_{36}H_{32}F_{12}N_4O_8Zn_2(H_2O)_1$	42.31	4.26	4.94	42.44	3.17	5.42	42.16	3.34	5.47
Set B	$C_{38}H_{46}F_6N_4O_8S_2Zn_2$ $C_{36}H_{38}F_6N_4O_6S_2Zn_2(H_2O)_{10}$	45.84	4.66	5.63	38.36	5.48	5.33	38.89	5.26	5.04
Set C	$C_{36}H_{38}F_6N_4O_8Zn_2$ $C_{36}H_{38}F_6N_4O_8Zn_2(H_2O)$	48.07	4.26	6.23	47.30	4.02	5.98	47.13	4.39	6.11
Set D	$C_{54}H_{82}F_6N_4O_{10}Zn_2$ $C_{54}H_{82}F_6N_4O_{10}Zn_2(H_2O)_8$	54.41	6.93	4.70	48.61	7.15	4.36	48.54	7.39	4.19
Set E	$C_{32}H_{32}F_4N_4O_4Zn_2$	51.70	4.34	7.54	51.64	4.06	7.35	51.64	4.06	7.35

Table 5.3.3. Thermogravimetric analysis results explanation

Compound	Lattice Solvent molecule	Calculated Solvent loss (%)	Observed Solvent loss (%)	Theoretical final Residue (%)	Found Final Residue (%)
Set A	4 (CH_3OH)	11.23	7.13	14.33	25.95
Set B	2 (CH_3OH)	6.44	4.53	16.34	NA
Set C	NA	NA	6.74	18.09	31.07
Set D	4 (CH_3OH)	10.75	NA	13.65	NA
Set E	none	0	2.47	21.90	41.41

5.4. Characterisation in solution state.

With the complexes in hand, we attempted to elucidate if they retain their structure in solution; therefore, we recorded ^{1}H and ^{19}F NMR and ESI-MS. The ESI-MS data for sets **A**, **B**, **D** and **E** (Figures S4-36-S4-42,) validate the formation of monomeric and dimeric species; a characteristic peak with corresponding isotropic distribution can be identified. Then we recorded the ^{1}H NMR in d_6-DMSO-H_2O media (Figure 5.4.1.). The symmetric sets (**A** and **E**) show distinct peaks; however, the asymmetric sets (**B**, **C** and **D**) show broad and different peaks a possible outcome of the existence of other species (Figure 5.1.2). To avoid the interpretation of these complicated patterns, we recorded the ^{19}F NMR data. For sets **A**, **B** and **C** a single peak in the -58.65 ppm area can be found, with a minor peak for **C** at -58.76ppm, whereas set **D** shows two peaks; one broad with a shoulder centred at -58.68 ppm and one at -58.74ppm. The single peak shifts at -121.59 ppm for set **E** and exhibits a shoulder. Given that we performed solution and theoretical studies for similar systems in another chapter (chapter 3), we consider that these species exist in an equilibrium of monomer-dimer in aqueous media; thus the broad peak observed in the ^{19}F NMR can be an average signal of both species. Notably, as it is depicted in Figure 5.1.2, for the asymmetric salan complexes, two different conformations may appear, therefore, the number of potential species increases.

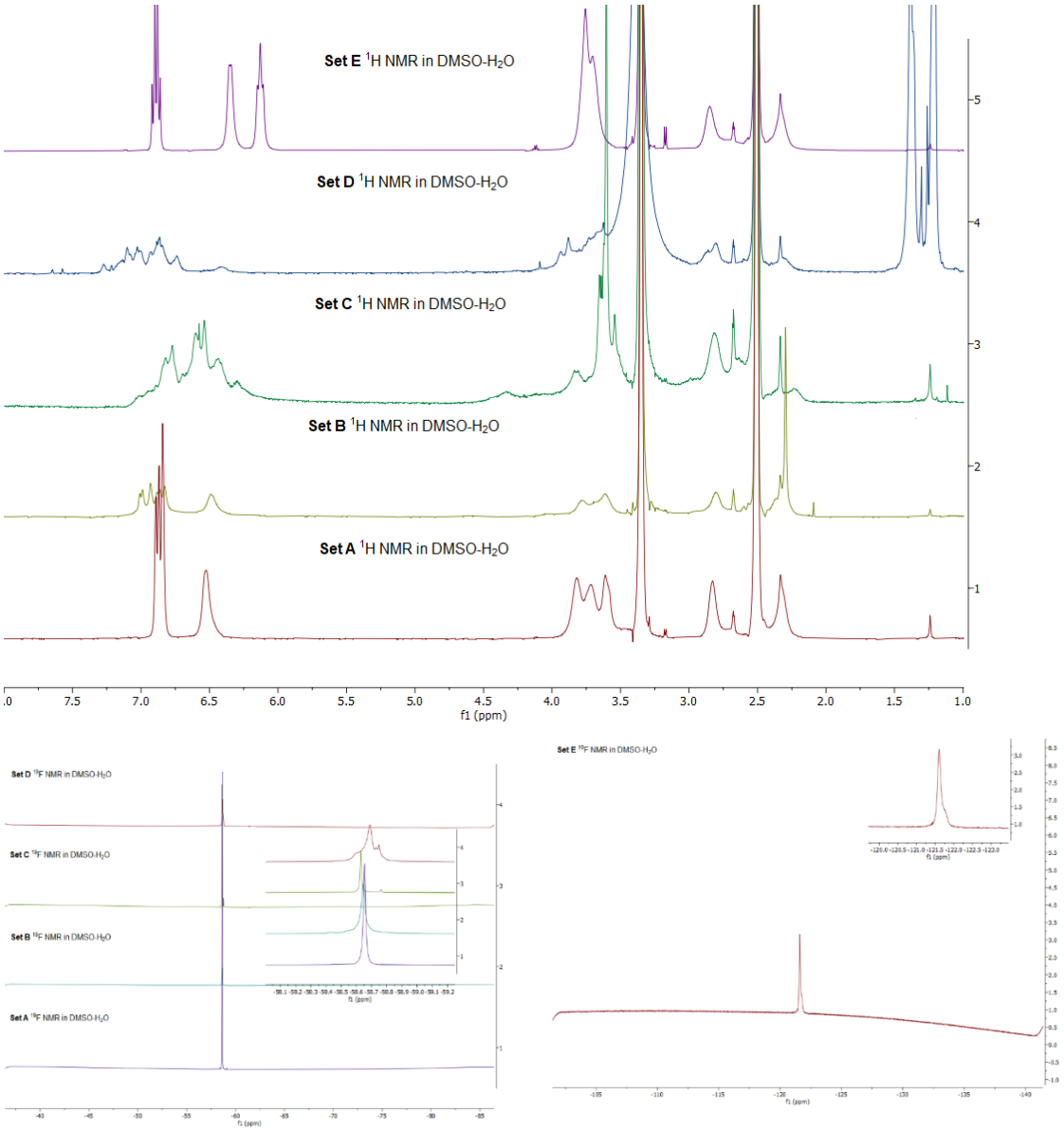

Figure 5.4.1. (Upper) ^{1}H NMR data for sets **A – E**, (lower) ^{19}F NMR data for sets **A** - **D** (left) and **E** (right)

5.5. Theoretical calculations

We investigated the species present in the DMSO-water solution of the asymmetric **set B** and symmetric **set E**, see Figure 5.1.1. To find the most relevant species present in the solution, we screened the conformation space using CREST, after re-optimising the lowest and most representative minima at the B3LYP -D3 /6-31g(d,p) &SDD level treating the solvent (DMSO) as a continuum media with PCM in Gaussian. We aimed to find the relative energies of monomeric and dimeric species without coordinated species, water coordinated, and DMSO coordinated, based on data obtained in the chiral amine sensing. For **sets B** and **E** searched the conformers and optimised the geometries

only of the species to be most relevant in the previous study: these are the **BDimer**, **BMonomer**, **BDimer(H₂O)₃**, **BMonomer(H₂O)₃**, **BDimer(DMSO)₂** and **BMonomer(DMSO)₂**, and **EDimer**, **EMonomer**, **EDimer(H₂O)₃**, **EMonomer(H₂O)₃**, **EDimer(DMSO)₂** and **EMonomer(DMSO)₂** for **sets B** and **E**, respectively. The results are summarised in Figure 5.5.1

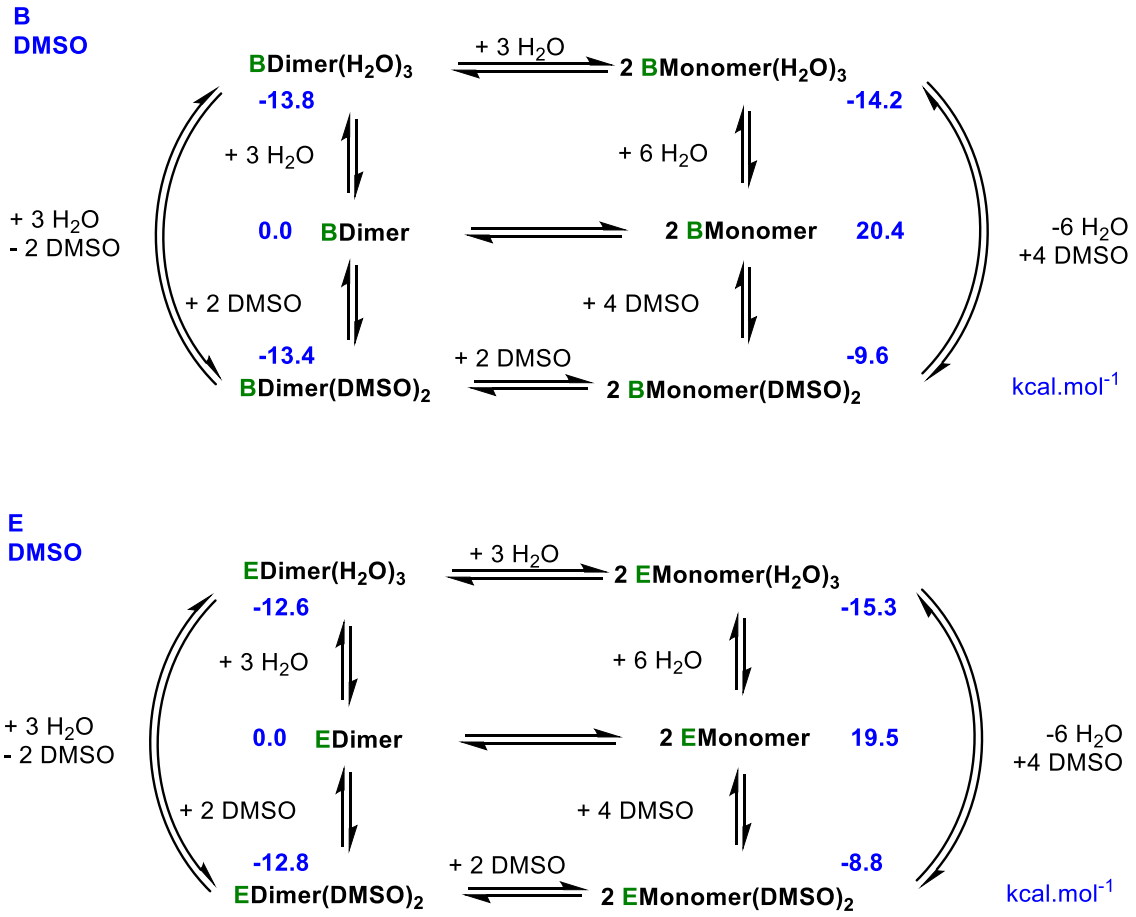

Figure 5.5.1. Schematic representation of the reaction network of the most relevant species for **set B** (top) and **set E** (bottom) in DMSO. Relative energies correspond to free energies in DMSO and in kcal.mol^{-1}.

The calculations for the two **sets B** and **E,** show exciting differences and similarities. The relative stability of **BDimer** and **BMonomer** and **EDimer** and **EMonomer** (without any molecule coordinated) is close to 20 kcal.mol^{-1}. In both cases, the existence of the dimer is favoured. The differences appear when water is coordinated; for **sets B** and **E,** the **BMonomer(H₂O)₃** and **EMonomer(H₂O)₃** species are favoured over **BDimer(H₂O)₃** and **EDimer(H₂O)₃**. Both species have close energies, and the equilibrium could be observed depending on the water concentration. Coordination of DMSO instead of water forms **BDimer(DMSO)₂** and **EDimer(DMSO)₂** with similar energy to the dimer water complexes. At the same time, monomers **BMonomer(DMSO)₂** and **EMonomer(DMSO)₂** are slightly

less stable, 4.6 kcal.mol^{-1} above **BDimer(H_2O)** and 6.5 kcal.mol^{-1} above **EDimer(H_2O)$_3$**. These species coordinate the DMSO through the oxygen, and coordination by the sulfur is disfavored. Using the equilibrium constants of the above-mentioned chemical equations and the mass balances, we can find the preferred species in solution according to computational energies. Finally, considering the parameters for the sensing studies, these are complex (**BDimer** or **EDimer**) 1 10^{-3} M, DMSO 14.06 M and 0.1 M water, only one species would be formed in significant amounts of the **BMonomer($DMSO$)$_2$** or **EMonomer($DMSO$)$_2$**. However, if the concentration of water increases then the species **BMonomer(H_2O)$_3$** or **EMonomer(H_2O)$_3$** become abundant.

5.6. Sensing studies.

To understand the behaviour of the ligand and the corresponding complex, we performed titration studies for one system (Set A). The results are shown in Figures 5.6.1 and 5.6.2. It is evident that the addition of the $Cd(NO_3)_2$ into the ligand or complex system imposes a different impact; the peak in the former case shifts to the right and above one equivalent shift to the left, while for the latter case, the peak shifts to the left.

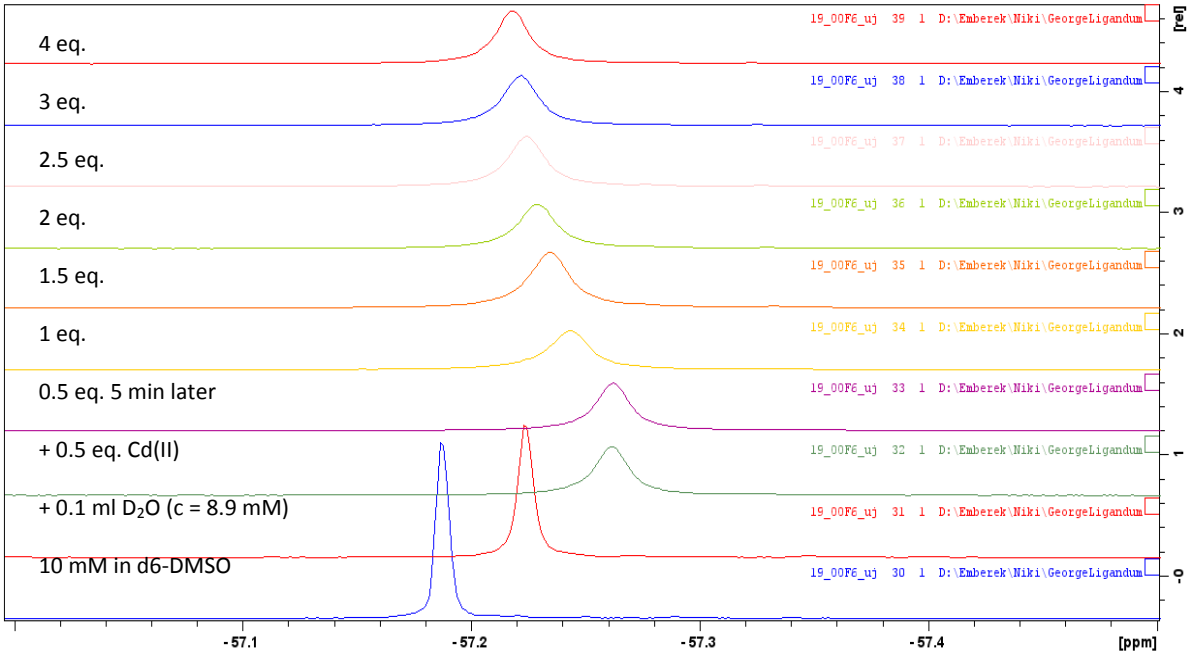

Figure 5.6.1: The effect of Cd^{2+} ions on the ^{19}F NMR spectra of ligand for set **A**

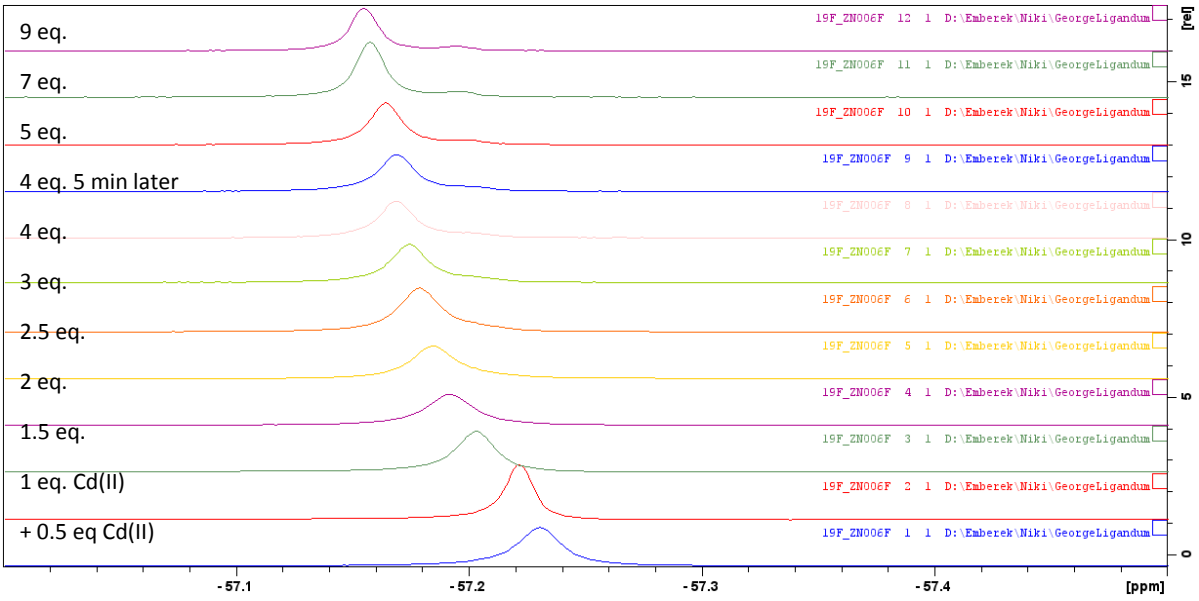

Figure 5.6.2.: The effect of Cd^{2+} ions on the ^{19}F NMR spectra for set **A**.

Then we performed the same studies with Pb^{2+} (Figure 5.6.3 &5.6.4). Adding Pb^{2+} causes a continuous shift in the ^{19}F NMR spectra. After adding four equivalent Pb^{2+} the peak flattens (Fig. 5.6.3). This shift is only partly due to the increasing amount of water in the solution. The composition of the solution changes continuously. For the complex titrations, the peak is broad compared to the ligand, indicating the presence of several species. Adding 0.33 equivalent Pb^{2+} causes a significant up-field shift, then a little reversal. Later, an up-field shift is observed again. (Fig. 5.6.4). The addition of three equivalents of Pb^{2+} ions causes double peaks (a shoulder also can be seen at two equivalents), where the excess of Pb^{2+} ions may displace $zinc^{2+}$ ions. The solution becomes opalescent when four equivalents Pb^{2+} ions are added to the solution.

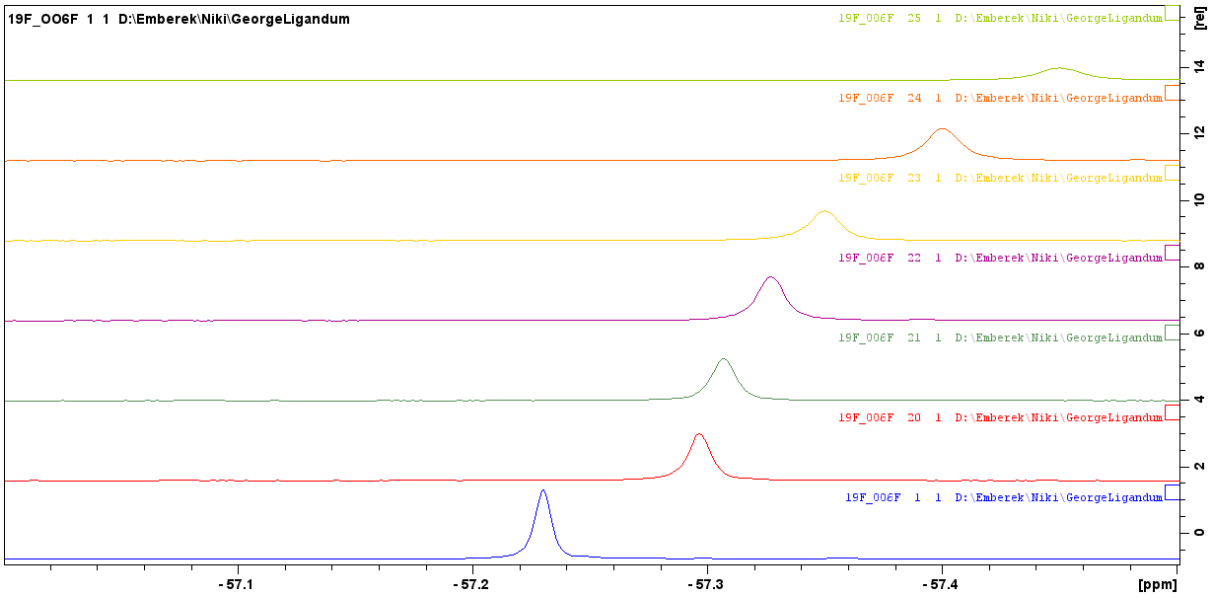

Figure 5.6.3: The effect of Pb^{2+} ions on the the^{19}F NMR spectra of the ligand set **A**.

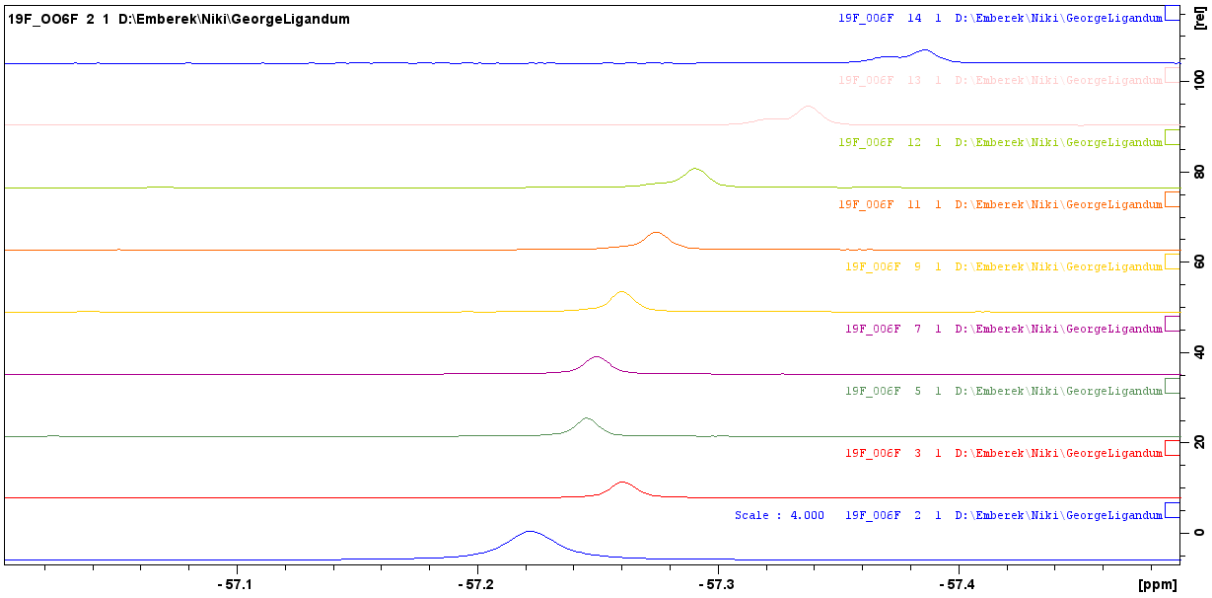

Figure 5.6.4: The effect of Pb^{2+} ions on the ^{19}F NMR spectra for set **A**.

Then we investigated the behaviour of system **E**, with different equivalents of Cd^{2+}. As seen in Figure 5.6.5, adding one equivalent of Cd^{2+} imposes the appearance of three other peaks. In contrast, adding more Cd^{2+} equivalents favours the peak at -120.5 ppm.

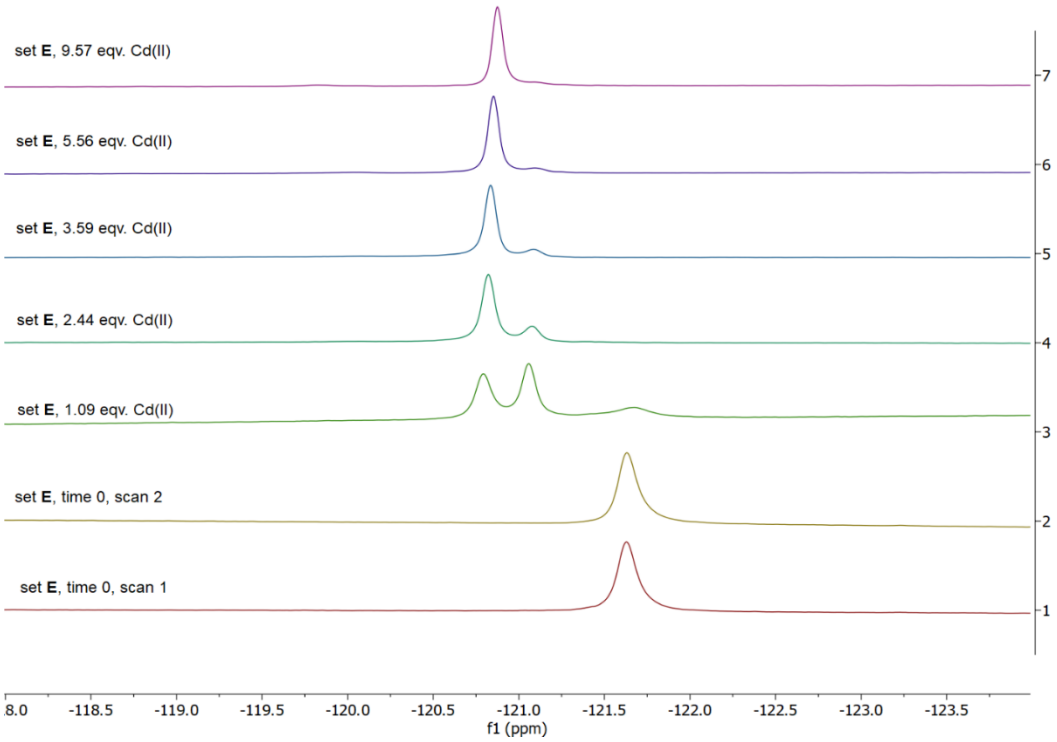

Figure 5.6.5. (Upper) ^{19}F NMR data for set **E** with different equivalents of Cd (0.6 ml DMSO + 0.1 ml D_2O (c = 10 mM)

5.7. Conclusions

We examined for the first time the ability of fluorine-based Zn-salan complexes to sense HMIs with ^{19}F NMR. The symmetric sets (**A** and **E**) crystallise as anticipated in a dimeric form. However, different speciations are isolated for the asymmetric sets (**B**, **C** and **D**), and all compounds are susceptible to moisture upon storage. This finding suggests that fine-tuning the periphery of these systems significantly impacts the nature of the final specie. In solution, the compounds are in an equilibrium of dimeric-monomeric form. However, for the asymmetric sets, additional speciation's can be identified (Figure 5.1.2). ^{19}F NMR studies prove challenging since several species can be identified, especially for the asymmetric system. Preliminary studies of set **A** with Cd^{2+} and Pb^{2+} ions suggest a different type of interaction. In contrast, for set **E**, it is evident that three different species can be identified when titration with Cd^{2+} takes place. More titrations and theoretical studies are needed to elucidate these molecular systems' interaction (aggregation-antenna, transmetallation, Figure 5.1.1.) mechanism. The work from this PhD has established the basis to underpin the mechanism, and future work is necessary to underpin the mechanism.

6. Chapter 6: Conclusions and future directions

6.1.1. Concluding summary

Despite the many environmental legislations and regulations, the Niger Delta region has continued to witness devastating ecological damage owing to the activities of International Oil companies and their subsidiaries; these leads to massive pollution of the area with both toxic organic and inorganic compounds and hence my motivation to be In the University of Sussex to develop a mechanism for detecting and sensing purposes. Therefore, this thesis is aimed at designing, developing, and synthesizing economically viable ligands using easy synthetic steps and readily available precursors, fine-tuning their scaffolds to suit their application, and incorporating both the Naptho and F-atom for Fluorescence and ^{19}F-NMR spectroscopy respectively was very helpful to monitor and detect the presence of compounds in an aqueous medium. This project successfully synthesized a library of symmetric and asymmetric molecular ligands, and their corresponding complexes were used as probes for sensing studies. The novel synthesized SH-nap, OH-nap, and OF-nap asymmetric salans could selectively sense and detect Cu^{2+} and Fe^{3+} in the presence of other metal ions and monitored using fluorescence spectroscopy, as described in chapter 2. Another library of both symmetric and asymmetric salans was Successfully synthesized, and their corresponding zinc complexes were used as sensing probes for selected HMPs; the sensing mechanism and signal changes were monitored and studied using ^{19}F-NMR spectroscopy, and from the results obtained, these zinc complexes probes are excellent scaffolds in detecting and sensing of theses selected HMPs as described in chapter 5. To further improve on my research and sensing techniques, A novel water-soluble asymmetric fine-tune ligand ($H_4oct^{(p\text{-}OCF3)}salox$) was synthesized after several steps and successfully characterised with their toxicity evaluated, salox ligand was found to readily complex with yttrium to form a non-toxic molecular entity $[Yoct^{(p\text{-}OCF3)}salox]^-$ and is demonstrated that it can be used for multimodal monitoring purposes of GABA NT. *In vitro* monitoring with UV-Vis, ^{19}F NMR, and fluorescence and DFT calculations allow mapping complex/NT interaction and rationalising the selective sensing mechanism. This work opens new research directions in coordination and bioinorganic chemistry by introducing a non-toxic molecular sensor with immediate (in vivo potential) application in neuroscience, as described in chapter 4. We had, for the first time, examined the sensing potentials of fluorine-based chiral zinc complexes as probes derived from a library of symmetric chiral

salan ligands, these probes sense and detect some selected chiral amines, and the Zn^{2+} complexes were successfully isolated as dimers, and changes to monomeric form when coordinating solvents are used, these coordinating solvents occupy the vacant position in the coordinating spheres and as such makes exchanging with the analyte very difficult and hence in excess amount indicating that the presence of coordinating solid solvents is a critical parameter to look into when designing scaffolds for sensing studies.

6.2.1. Future studies

Future studies will mainly focus on the design and development of molecular scaffolds that incorporate the F-atom close to the metal centre, thus making the molecular scaffolds to be more sensitive and selective to any changes in their local environments during sensing studies using ^{19}F-NMR spectroscopy, the choice of solvents for sensing studies and investigations will also be considered as important due to coordinating solvents might hinder sensing studies of HMPs because they tend to occupy the vacant coordination spheres and thus affect sensing/detecting studies.

The design and development of this scaffold will also centre on introducing less toxic water-soluble compounds that can be encapsulated onto a solid substrate for sensing studies in bioinorganic chemistry with possible applications in neurosciences, drug discoveries and cancer research. However, this would be analysed, and their potential evaluated before using it on natural live aqueous environments like rivers, running waters, lakes, and seas.

Changing the position of the Fluorine-based atom linker in the scaffold closer to the metal centre, as illustrated in figures 6.2.1 and 6.2.2 below, will hopefully increase the sensitivity and selectivity potentials of fluorinated-zinc-based sensors towards any changes in their local environments.

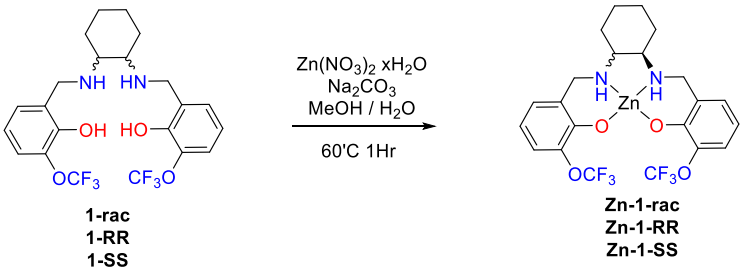

Figure 6.2.1. Future works showing changes in the position of Fluorine-based linkers as attached.

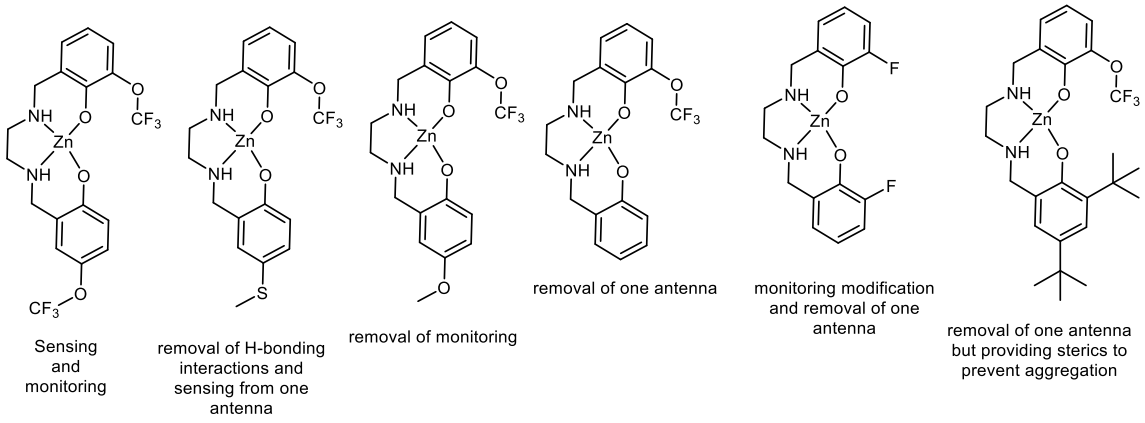

Figure 6.2.2. Future works showing changes in the position of Fluorine-based linkers are attached.

Other future works include developing and designing asymmetric salan ligands with linkers to increase their hydrophilicity, stability and less of toxicity; this can be achieved by incorporating into the scaffold carboxylic group to promote its hydrophilicity.

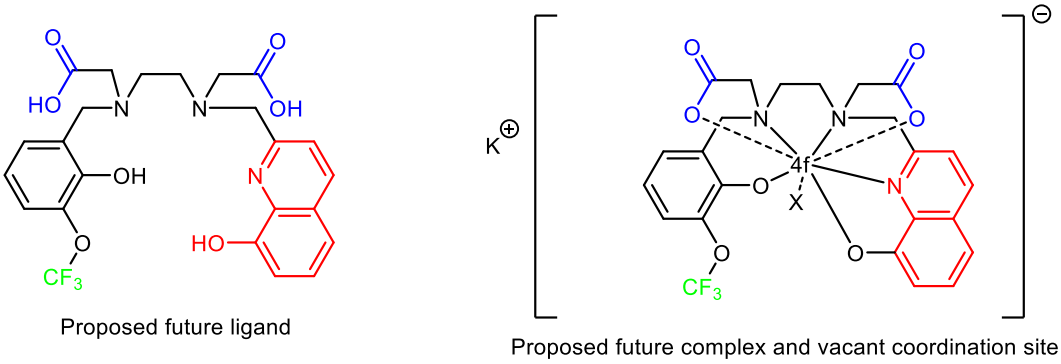

Figure 6.2.3. Future works showing changes in the position of Fluorine-based linkers are attached.

Other future studies will involve a structural and conformational changes in the possible structure of the Naphtho salan ligand by improving on its hydrophilicity and improved sensing by changing the position of the F-atom linker for both Fluorescence and 19F-NMR spectroscopic studies towards selective sensing and detecting mechanism of Cu^{2+} and Fe^{3+} as illustrated in the figure 6.2.4. below.

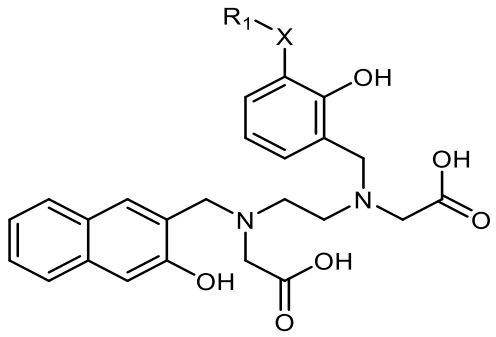

X= F
R1= SH, OH, OF

Figure 6.2.4. Future works showing changes in the position of Fluorine-based linkers and improved hydrophilicity for the Naphtho asymmetric salan ligand.

7 Chapter 7: Experimental design and synthetic procedures

7.1 Materials

All reagents used were bought from Fluorochem, Apollo Scientific, Sigma Aldrich, Acro organics, and Tokyo Chemical industries and were used without any further purification. All experiments were performed under Nitrogen or Argon and or aerobic conditions.

7.2. General Scientific methods and instrumentation

NMR spectra obtained were recorded with Varian VNMRS 600 and 400 at 25 °C, at either 600 MHz, 376 MHz, or 151 MHz in Chloroform-d or DMSO-d_6. Or D_2O. NMR chemical shift signals were recorded in parts per million(ppm). HRMS data were obtained with a Bruker Daltonics Fourier Transform (FTMS) Apex II spectrometer with electrospray ionization (ESI) using Dichloromethane, methanol, and water as solvent. HR-MS data were obtained on a VG Autospec Fissions instrument (EI at 70 eV), It is a destructive method that reports the fragments of molecular ions as mass/charge (m/z) ratios. The FT-IR spectra were recorded over the range of 4000–650 cm^{-1} on a PerkinElmer Spectrum fitted with a UATR polarisation accessory. The Thermogravimetric analysis (TGA) was carried out using a Thermogravimetric analyzer model number Q-50 V20.13 with a platinum pan, in a nitrogen atmosphere from 25 – 820 °C, at a scan rate of 5 °C/min, UV−Vis measurements (280-750 nm) were performed at room temperature (15-20˚C) using a Thermo Scientific Evolution 300 UV-Vis spectrophotometer equipped with 5mm path length quartz cells, and the collected data were processed using the Vision Pro software. The LCMS investigations of the water-soluble compound in Chapter 1 were carried out using Shimadzu LC-MS 2020, on a Gemini 5 m C18110 Å. Purification of the novel compounds was done using normal-phase silica flash column chromatography and conducted on a Teledyne Isco Combiflash with UV detection at all wavelengths.

pH-metric titrations (Chapters 2 & 4) were carried out in Hungary using MOLSPIN by one of our collaborators using a pH-meter equipped with a 6.0234.100 combined glass electrode (Metrohm) used for pH measurements (in the pH range 2.9–11.5), while the dosing of the titrant was made with a MOL-ACS micro burette controlled by a computer. During the measurement, argon was bubbled through the samples to ensure the absence of oxygen and carbon dioxide. All pH-potentiometric measurements were carried out at a constant ionic strength of 0.2 M KCl and a constant temperature (298 K). The LCMS investigations of the $H_4oct^{(p\text{-}OCF3)}$salox ligand were carried out using Shimadzu

LC-MS 2020, on a Gemini 5 m C18110 Å. Purification of $H_4oct^{(p\text{-}OCF3)}$salox was done using normal-phase silica flash column chromatography and conducted on a Teledyne Isco Combiflash with UV detection at all wavelengths

The fluorescent excitation studies conducted in Chapter two and four were carried out at the University of Sussex at sapells lab.

Toxicity and circular dichroism studies of the novel water-soluble and chiral compounds in chapter 2 and chapter 4 were carried out in Sapell's lab, Biochemistry department, School of life science.

The X-ray diffraction (XRD) measurements of crystals were carried out at the University of Sussex and the National Crystallography Service, University of Southampton, In both cases, suitable colourless block-shaped Zinc crystals were selected and mounted on a MITIGEN holder in perfluoro ether oil on a Rigaku FRE+ equipped with VHF Varimax confocal mirrors and an AFC12 goniometer and HyPix 6000HE detector and data were collected at T = 100(2)K. The data were processed with CrysAlisPro and solved by intrinsic phasing methods with SHELXT.

7.3. Chapter 2: Synthetic procedure

7.3.1.1 Synthesis of Half unit for non-Symmetric salan ligand

2-((2-aminoethyl) amino)-4-methoxyphenol

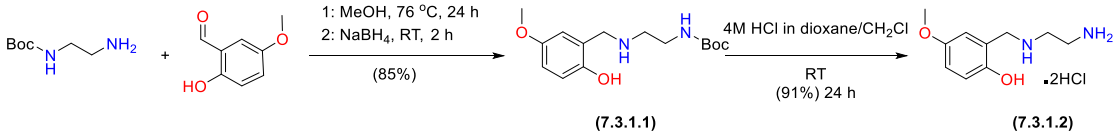

(7.3.1.1) (7.3.1.2)

Scheme 7.3.1.1. Synthetic route for the half unit of non-asymmetric salan ligand.

The compound (7.3.1.2) was synthesized using a modified protocol earlier described above by loving,[362] (0.488mL, 4mmol, 1eq) of 2-hydroxy, 5-methoxy benzaldehyde was dissolved in 15mL of methanol inside a 100mL RBF, and (0.633mL, 4mmol, 1eq) of tertiary butyl carbamate was added and the mixture stirred at reflux for 24 hours, the reaction mixture was cooled to room temperature before adding stepwise $NaBH_4$ (0.454 g, 12 mmol, 3eq) in small portions over 20 minutes. The reaction was further stirred at room temperature for 2 hours before quenching with saturated sodium carbonate (65mL) and extract with dichloromethane (3 x 50 mL). The combined organic phases were washed with saturated brine (40 mL) and dried over $MgSO_4$. The solvent was evaporated *in vacuo* to give (1.000g, 3.376mmol, 84%) of **(7.3.1.1)** as a brownish solid

which was used without further purification, To synthesized compound (7.6.1.2), (0.557g, 1.880mmol) of (7.3.1.1.) were dissolved in (9mL) of dichloromethane to obtain a clear solution before adding (3mL) of 4N HCL in dioxane solvent ratio and stirred overnight at room temperature, visible formation of white solid was observed, which was filtered, washed with pet ether and dried to obtain the desired white solid.(0.464g, 1.712mmol, 91% yield)

^{1}H NMR (600 MHz, DMSO) δ 6.82 (t, *J* = 5.8, 5.8 Hz, 1H), 6.70 (d, *J* = 2.9 Hz, 1H), 6.67 – 6.59 (m, 2H), 3.73 (s, 2H), 3.64 (s, 3H), 3.03 (q, *J* = 6.3, 6.3, 6.3 Hz, 2H), 2.52 (t, *J* = 6.5, 6.5 Hz, 2H), 1.36 (s, 9H).

^{13}C NMR (151 MHz, DMSO) δ 155.66, 151.83, 150.72, 125.22, 115.65, 114.21, 112.73, 77.56, 55.29, 49.99, 48.02, 28.27.

(HRMS + TOF MS ES+) calculated $C_{15}H_{24}N_2O_4$: 296.17, observed: 297.1832.

^{1}H NMR (600 MHz, DMSO) δ 9.78 (s, 1H), 9.59 (s, 2H), 8.43 (s, 3H), 7.13 (d, *J* = 3.0 Hz, 1H), 6.89 (d, *J* = 8.9 Hz, 1H), 6.84 – 6.79 (m, 1H), 4.09 (s, 2H), 3.69 (s, 2H), 3.23 – 3.17 (m, 3H).

^{13}C NMR (151 MHz, DMSO) δ 151.93, 149.70, 118.11, 116.50, 116.24, 116.00, 55.50, 44.98, 43.60, 35.22.

(HRMS + TOF MS ES+) calculated $C_{10}H_{18}N_2O_2$: 196.25, observed: 197.1278.

7.3.2.1. Synthesis of non-Symmetric salan ligand

3-(((2-((2-hydroxy-5-methoxybenzyl) amino) ethyl) amino) methyl) naphthalen-2-ol

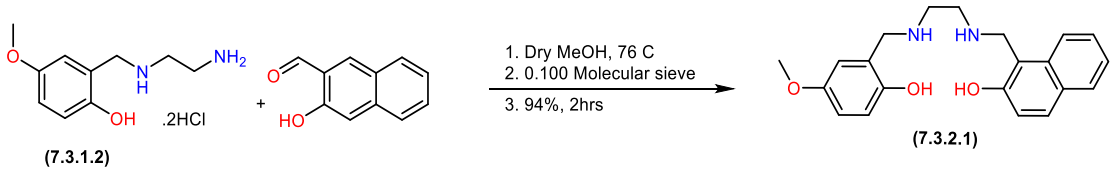

(7.3.1.2) (7.3.2.1)

Scheme 7.3.2.1. Synthetic route for the synthesis of non-Symmetric salen Ligand.

The above named Non-symmetric salan ligand was synthesized using the modified protocol of Loving[362] and Thiele[363] with one step, (0.898g, 3.3mmol, 1eq) of (7.3.1.2.) was placed in a 100ml RBF containing 0.100g activated molecular sieve and 20mL of dry methanol under stirring at room temperature, (0.919mL, 6.6mmol, 2eq) of triethylamine was added stepwise and stirred for 15 minutes before adding (0.568g, 3.3mmol, 1eq) of 2-hydroxy-napthalene carbaldehyde and refluxed for two hours at 76°C. Upon reaction completion, the solution was allowed to cool to room temperature before adding slowly and stepwise (0.499g, 13.2mmol, 4eq) of sodium borohydride and

stirring continued at room temperature for 2hrs, the reduction process was quenched using 75ml of ice/cold water and 3ml of methanol added and the RBF was left overnight in a Fume hood for the desired compound to crystalize out to obtain a yellowish solid **(7.3.2.1)**.(1.098g, 3.115mmol, 94% yield**).**

^{1}H NMR (600 MHz, DMSO) δ 7.87 (d, *J* = 8.5 Hz, 1H), 7.76 (d, *J* = 8.1 Hz, 1H), 7.67 (d, *J* = 8.8 Hz, 1H), 7.44 – 7.38 (m, 1H), 7.28 – 7.22 (m, 1H), 7.01 (d, *J* = 8.8 Hz, 1H), 6.72 (s, 1H), 6.68 – 6.60 (m, 2H), 4.27 (s, 2H), 3.75 (s, 2H), 3.64 (s, 3H), 2.72 (t, *J* = 6.1, 6.1 Hz, 2H), 2.66 (t, *J* = 6.1, 6.1 Hz, 2H).

^{13}C NMR (151 MHz, DMSO) δ 156.09, 152.00, 150.77, 132.85, 128.53, 127.94, 126.32, 122.25, 121.96, 119.12, 115.79, 114.39, 113.86, 112.88, 55.44, 50.16, 48.01, 47.63, 45.79.

(HRMS + TOF MS ES+) calculated $C_{21}H_{24}N_2O_3$: 352.430, observed: 353.1866.

7.3.3.1. Synthesis of the half unit for non-Symmetric salan ligand

2-((2-aminoethyl) amino)-4- (methyl thio) phenol

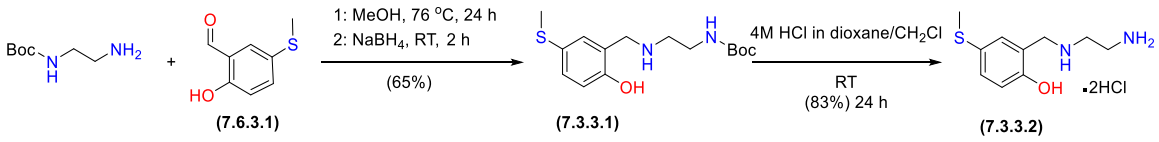

Scheme 7.3.3.1. Synthetic route for the synthesis of the half unit of non-Symmetric Salan Ligand.

^{1}H NMR (600 MHz, DMSO) δ 7.21 (d, *J* = 2.4 Hz, 1H), 7.19 – 7.14 (m, 1H), 6.98 – 6.93 (m, 1H), 6.80 (d, *J* = 8.3 Hz, 1H), 5.61 (s, 2H), 3.88 (s, 2H), 3.16 (d, *J* = 6.2 Hz, 2H), 2.65 (s, 1H), 2.50 (s, 3H), 1.49 (s, 9H).

^{13}C NMR (151 MHz, DMSO) δ 156.11, 156.09, 129.32, 128.50, 125.94, 125.84, 116.53, 78.00, 50.12, 48.41, 40.47, 40.03, 28.69, 28.55, 17.63.

(HRMS + TOF MS ES+) calculated $C_{15}H_{24}N_2O_3S$: 312.430, observed: 312.1655.

^{1}H NMR (600 MHz, DMSO) δ 7.47 (d, *J* = 2.4 Hz, 1H), 7.21 – 7.17 (m, 1H), 6.96 (d, *J* = 8.4 Hz, 1H), 4.09 (s, 2H), 3.38 (s, 3H), 3.18 (s, 1H), 2.42 (s, 3H).

^{13}C NMR (151 MHz, DMSO) δ 154.33, 131.14, 130.16, 126.53, 118.75, 116.26, 44.77, 43.73, 35.24, 16.80.

(HRMS + TOF MS ES+) calculated $C_{10}H_{16}N_2OS$: 212.310, observed: 213.1066.

The name half-unit of (7.3.3.2.) was synthesized following a similar protocol to obtained (0.300g, 0.960mmol, 65%) of (7.6.3.1) and (0.212g, 0.737mmol, 83%) of (7.6.3.2.) white solid.

7.3.4.1. Synthesis of non-Symmetric salan ligand

3-(((2-((2-hydroxy-5-(methyl thio) benzyl) amino) ethyl) amino) methyl) naphthalen-2-ol

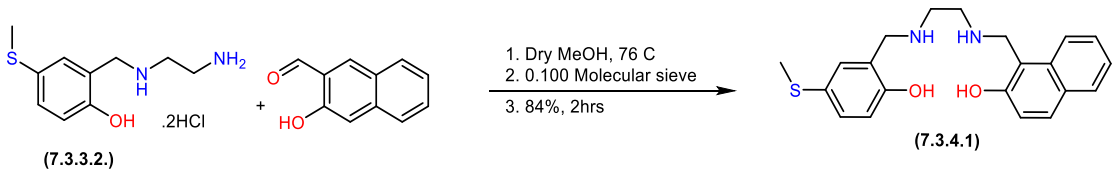

(7.3.3.2.) (7.3.4.1)

Scheme 7.3.4.1. Synthetic route for the synthesis of non-symmetric salan Ligand.

The above-named non-symmetric salen ligand was synthesized following similar protocol to obtained (0.718g, 1.948mmol, 84%) of (7.3.3.1) which was yellowish solid.

^{1}H NMR (600 MHz, DMSO) δ 7.88 (d, *J* = 8.6 Hz, 1H), 7.76 (d, *J* = 8.1 Hz, 1H), 7.67 (d, *J* = 8.8 Hz, 1H), 7.44 – 7.38 (m, 1H), 7.28 – 7.22 (m, 1H), 7.17 (t, *J* = 4.9, 4.9 Hz, 1H), 7.07 – 6.99 (m, 2H), 6.72 – 6.66 (m, 1H), 4.27 (s, 2H), 3.77 (d, *J* = 6.1 Hz, 2H), 2.75 – 2.70 (m, 2H), 2.69 – 2.64 (m, 2H), 2.36 (d, *J* = 14.8 Hz, 3H).

^{13}C NMR (151 MHz, DMSO) δ 156.32, 156.03, 155.32, 133.14, 129.36, 128.80, 128.48, 128.22, 126.59, 122.53, 122.25, 119.39, 116.51, 116.35, 114.16, 50.14, 48.22, 47.88, 46.02, 17.62, 17.53.

(HRMS + TOF MS ES+) calculated $C_{21}H_{24}N_2O_2S$: 368.50, observed: 367.1634.

7.3.5.1. Synthesis of non-Symmetric salan ligand

3-(((2-((2-hydroxy-5-(trifluoromethoxy) benzyl) amino) ethyl) amino) methyl) naphthalen-2-ol

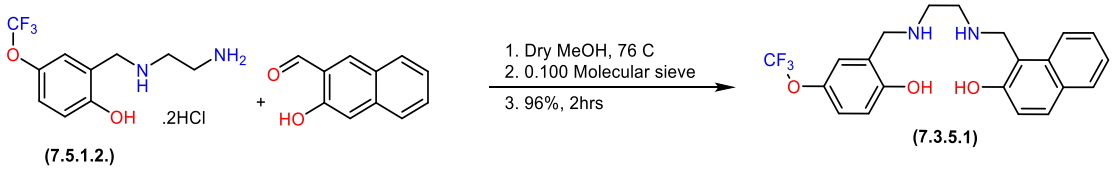

(7.5.1.2.) (7.3.5.1)

Scheme 7.3.5.1. Synthetic route for the synthesis of non-Symmetric salen Ligand.

The above-named non-symmetric salen ligand was synthesized following similar protocol to obtained (0.906g, 2.229mmol, 96%) of (7.6.5.1) which was light yellowish solid.

^{1}H NMR (600 MHz, DMSO) δ 7.94 (d, *J* = 8.6 Hz, 1H), 7.79 (d, *J* = 8.1 Hz, 1H), 7.74 (d, *J* = 8.8 Hz, 1H), 7.45 (t, *J* = 7.7, 7.7 Hz, 1H), 7.28 (t, *J* = 7.5, 7.5 Hz, 1H), 7.23 – 7.18 (m, 1H), 7.12 (s, 1H), 7.07 (dd, *J* = 8.7, 2.9 Hz, 1H), 6.82 (d, *J* = 8.7 Hz, 1H), 4.35 (s, 3H), 3.79 (s, 2H), 2.87 (d, *J* = 12.4 Hz, 2H), 2.76 (t, *J* = 6.2, 6.2 Hz, 2H).

^{13}C NMR (151 MHz, DMSO) δ 156.34, 156.24, 133.04, 128.68, 128.10, 126.86, 126.46, 122.40, 122.12, 121.68, 120.77, 119.76, 119.30, 116.26, 114.07, 49.39, 48.11, 47.84, 45.88, 40.34.

^{19}F NMR (376 MHz, DMSO) δ -57.20.

(HRMS + TOF MS ES+) calculated $C_{21}H_{21}N_2O_2F_3$: 406.41 observed: 407.1569.

7.4. Chapter 3: Synthetic procedure

7.4.1.2. Synthesis of 1R,2R Chiral ligand with cyclo-backbone

2,2'-(((1R,2R)-cyclohexane-1,2-diylbis(azanediyl)) bis (methylene)) bis (4-(trifluoromethoxy)phenol)

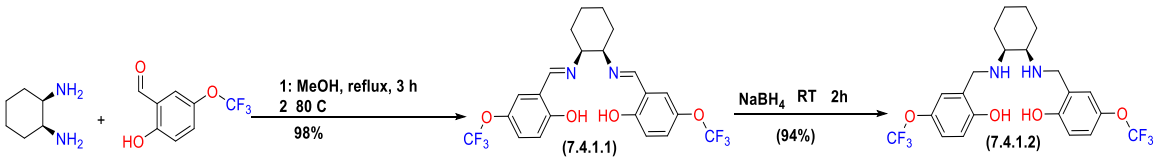

Scheme 7.4.1.2. Synthetic route for the synthesis of the 1R,2R (7.4.1.2) Chiral ligand.

The above-named compounds were synthesized as a novel chiral ligand by modifying the procedure described by Loving.(1.00g , 8.75mmol, 1eq) of (R,R)-(-)-1,2-diaminocyclohexane was dissolved in a 15mL of MeOH in a 100 ml RBF and stirred at RT for 10mins before adding slowly (2.45ml, 17.51mmol ,2eq) of 2-hydroxy-5-triflouromethoxybenzaldehyde and refluxed for 2 hours at 80°C. Upon reaction completion, the solution was allowed to cool to RT before filtering to obtain a yellowish solid and washing with cold MeOH to obtained (4.209g, 8.68mmol, 98% yield) (7.4.1.1.) T0 synthesized (7.4.1.2.), the unreduced version (7.4.1.1.) (2.00g, 4.078mmol, 1eq) was dissolved in a 10mL of MeOH in a 100mL RBF and stirred for 15 minutes to obtain a clear solution, $NaBH_4$ (0.463g, 12.23mmol, 3eq) was added stepwise. The stirring continued under room temperature for 2 hours, before quenching the reaction with icy cold water

and 5mL of MeOH to obtain a white crystalline solid through suction filtration, dried, and weighed (1.892g, 4.03mmol, 94% yield).

^{1}H NMR (600 MHz, DMSO) δ 13.41 (s, 2H), 8.53 (s, 2H), 7.43 (d, *J* = 3.0 Hz, 2H), 7.28 (dd, *J* = 9.0, 3.0 Hz, 2H), 6.90 (d, *J* = 9.0 Hz, 2H), 3.47 – 3.41 (m, 2H), 1.91 – 1.86 (m, 2H), 1.82 – 1.76 (m, 2H), 1.65 – 1.59 (m, 2H), 1.50 – 1.41 (m, 2H).

^{13}C NMR (151 MHz, DMSO) δ 164.06, 159.39, 139.77, 139.76, 125.60, 123.69, 122.71, 121.02, 119.32, 118.71, 117.98, 117.63, 71.08, 40.06, 32.25, 23.64.

^{19}F NMR (376 MHz, DMSO) δ -57.62.

(HRMS + TOF MS ES+) calculated $C_{22}H_{20}N_2O_4F_6$: 490.40, observed: 491.1416.

^{1}H NMR (600 MHz, DMSO) δ 7.14 (d, *J* = 3.1 Hz, 2H), 7.01 (dd, *J* = 8.8, 2.9 Hz, 2H), 6.75 (d, *J* = 8.8 Hz, 2H), 3.82 (d, *J* = 14.6 Hz, 2H), 3.71 (d, *J* = 14.5 Hz, 2H), 2.29 (d, *J* = 8.8 Hz, 2H), 2.02 – 1.97 (m, 2H), 1.65 – 1.60 (m, 2H), 1.16 (t, *J* = 10.1, 10.1 Hz, 2H), 1.07 (d, *J* = 10.8 Hz, 2H).

^{13}C NMR (151 MHz, DMSO) δ 155.86, 140.14, 127.61, 121.18 (d, *J* = 12.9 Hz), 120.28, 115.89, 59.87, 46.07, 30.17, 24.20.

^{19}F NMR (376 MHz, DMSO) δ -57.29.

(HRMS + TOF MS ES+) calculated $C_{22}H_{24}N_2O_4F_6$: 494.43. observed: 495.1721.

7.4.2.2. Synthesis of 1S,2S Chiral ligand with cyclo-backbone

2,2'-(((1S,2S)-cyclohexane-1,2-diylbis(azanediyl)) bis (methylene)) bis (4-(trifluoromethoxy)phenol)

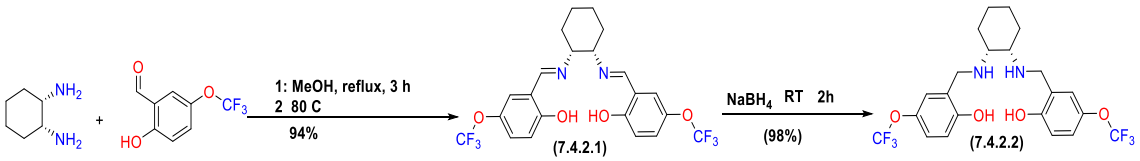

Scheme 7.4.2.2. Synthetic route for the synthesis of the 1S,2S (7.4.2.2) Chiral ligand.

The above-named compound was synthesized according to the general known procedure in 7.4.1.2. above, yellowish solid (4.017g, 8.191mmol, 94% yield) (74.2.1.) and whitish solid (1.980g, 4.006mmol, 98% yield) (7.4.2.2).

^{1}H NMR (600 MHz, DMSO) δ 13.35 (s, 2H), 8.53 (s, 2H), 7.43 (d, *J* = 3.0 Hz, 2H), 7.27 (dd, *J* = 9.0, 3.0 Hz, 2H), 6.90 (d, *J* = 9.0 Hz, 2H), 3.47 – 3.39 (m, 2H), 1.90 – 1.85 (m, 2H), 1.78 (dd, *J* = 7.2, 3.8 Hz, 2H), 1.62 (d, *J* = 13.2 Hz, 2H), 1.49 – 1.40 (m, 2H).

^{13}C NMR (151 MHz, DMSO) δ 164.27, 159.63, 139.99, 125.82, 123.90, 122.93, 121.24, 119.54, 118.91, 118.20, 117.85, 71.29, 40.20, 32.46, 23.84.

^{19}F NMR (376 MHz, DMSO) δ -57.63.

(HRMS + TOF MS ES+) calculated $C_{22}H_{20}N_2O_4F_6$: 490.43. observed: 491.1390.

^{1}H NMR (600 MHz, DMSO) δ 7.21 (d, *J* = 3.1 Hz, 2H), 7.09 – 7.04 (m, 2H), 6.81 (d, *J* = 8.8 Hz, 2H), 3.94 – 3.66 (m, 4H), 2.39 (d, *J* = 6.9 Hz, 2H), 2.04 (d, *J* = 11.2 Hz, 2H), 1.67 – 1.63 (m, 2H), 1.15 (p, *J* = 11.6, 11.6, 11.4, 11.4 Hz, 4H).

^{13}C NMR (151 MHz, DMSO) δ 156.33, 140.29, 127.95, 121.50, 121.42, 120.54, 116.20, 60.15, 46.35, 30.47, 24.50.

^{19}F NMR (376 MHz, DMSO) δ -57.31.

(HRMS + TOF MS ES+) calculated $C_{22}H_{24}N_2O_4F_6$: 494.43, observed: 495.1727.

7.4.3.2. Synthesis of 1S,2R Chiral ligand with cyclo-backbone

2,2'-(((1S,2R)-cyclohexane-1,2-diylbis(azanediyl)) bis (methylene)) bis (4-(trifluoromethoxy)phenol)

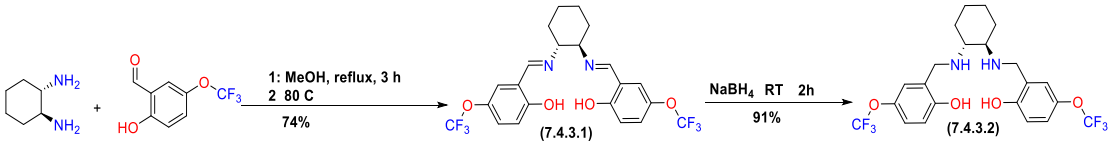

Scheme 7.4.3.2. Synthetic route for the synthesis of the 1S,2R (7.4.3.2) Chiral ligand.

The named compound was synthesized following a similar protocol as stated above in 7.4.1.2. yellowish solid (3.174g, 6.472mmol, 74% yield) (74.3.1.) and whitish solid (1.460g, 2.952mmol, 91% yield) (7.4.3.2).

^{1}H NMR (600 MHz, DMSO) δ 13.41 (s, 2H), 8.53 (s, 2H), 7.43 (d, *J* = 3.0 Hz, 2H), 7.30 – 7.25 (m, 2H), 6.90 (d, *J* = 9.0 Hz, 2H), 3.46 – 3.41 (m, 2H), 1.91 – 1.85 (m, 2H), 1.81 – 1.76 (m, 2H), 1.65 – 1.58 (m, 2H), 1.49 – 1.41 (m, 2H).

^{13}C NMR (151 MHz, DMSO) δ 164.32, 159.65, 140.02, 125.86, 123.95, 122.96, 121.27, 119.58, 118.97, 118.23, 117.89, 71.34, 32.50, 23.89.

^{19}F NMR (376 MHz, DMSO) δ -57.63.

(HRMS + TOF MS ES+) calculated $C_{22}H_{20}N_2O_4F_6$: 490.40. observed: 491.1416.

^{1}H NMR (600 MHz, DMSO) δ 7.16 (d, *J* = 3.0 Hz, 2H), 7.05 – 7.00 (m, 2H), 6.76 (d, *J* = 8.7 Hz, 2H), 3.83 (d, *J* = 14.6 Hz, 2H), 3.72 (d, *J* = 14.6 Hz, 2H), 2.33 – 2.28 (m, 2H), 2.03 – 1.97 (m, 2H), 1.65 – 1.60 (m, 2H), 1.16 (t, *J* = 10.3, 10.3 Hz, 2H), 1.07 (d, *J* = 10.7 Hz, 2H).

^{13}C NMR (151 MHz, DMSO) δ 155.72, 140.20, 127.59, 122.81, 121.23, 121.13, 120.30, 119.44, 117.75, 115.87, 59.85, 46.04, 30.15, 24.19.

^{19}F NMR (376 MHz, DMSO) δ -57.30.

(HRMS + TOF MS ES+) calculated $C_{22}H_{24}N_2O_4F_6$: 494.43. observed: 495.1727.

7.4.4.2. Synthesis of 1R,2R Chiral ligand with cyclo-backbone

6,6'-(((1R,2R)-cyclohexane-1,2-diylbis(azanediyl)) bis (methylene)) bis (2-methylphenol)

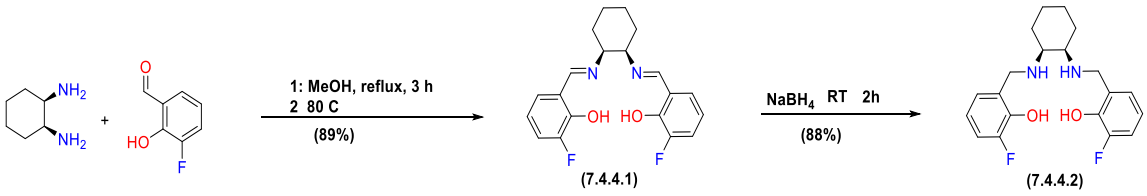

Scheme 7.4.4.2. Synthetic route for the synthesis of the 1S,2R (7.4.4.2.) Chiral ligand.

The above name compound was synthesized using the same protocol as described above, (0.5000g, 4.374mmol, 1eq) of (1R,2R)-(+)-1,2-diphenylethelenediamine was placed in a 100ml RB flask containing 15ml of MeOH and stirred for 15 mins to obtained a clear dissolved solution before slowly adding (1.226g, 8.750mmol, 2eq) of 2-hydroxy-3-flourobenzaldehyde and refluxed for two hours at 80°C. Upon reaction completion, the solution was allowed to cool to RT and suction filtered to have desired yield yellowish solid (1.391g, 1.743mmol, 89% yield) (7.4.4.1)

To synthesized (7.4.4.2.), aminative reduction of (7.4.4.1) was carried out, (0.794g, 2.216mmol, 1eq) of **(7.4.4.1)** was dissolved in a 100ml RBF containing 10mL of MeOH and stirred to obtained a clear solution before adding stepwise (0.252g, 6.65mmol, 3eq) of sodium borohydride and stirring continues under RT for 2hrs, the reaction was quenched with icy cold water and 5mL of MeOH to obtain a whitish crystalline flakes under suction filtration, dried, and weighed (0.707g, 1.950mmol, 88% yield).

^{1}H NMR (600 MHz, DMSO) δ 13.90 (s, 2H), 8.57 (s, 2H), 7.27 – 7.20 (m, 2H), 7.20 – 7.16 (m, 2H), 6.78 – 6.72 (m, 2H), 3.55 – 3.48 (m, 2H), 1.95 – 1.90 (m, 2H), 1.80 (tq, *J* = 7.7, 7.7, 5.0, 4.0, 4.0 Hz, 2H), 1.68 – 1.60 (m, 2H), 1.50 – 1.42 (m, 2H).

^{13}C NMR (151 MHz, DMSO) δ 165.32, 165.30, 151.50, 150.48, 150.39, 149.89, 127.12, 127.10, 119.91, 119.88, 118.63, 118.51, 117.42, 117.38, 70.19, 32.25, 23.62.

^{19}F NMR (376 MHz, DMSO) δ -138.27.

(HRMS + TOF MS ES+) calculated $C_{20}H_{20}N_2O_2F_2$: 358.15. observed: 359.1588.

^{1}H NMR (600 MHz, DMSO) δ 7.03 – 6.96 (m, 2H), 6.91 (d, *J* = 7.6 Hz, 2H), 6.65 (td, *J* = 7.8, 7.8, 4.9 Hz, 2H), 3.91 (d, *J* = 13.9 Hz, 2H), 3.82 (d, *J* = 13.9 Hz, 2H), 2.40 (s, 2H), 2.01 (s, 2H), 1.63 (s, 2H), 1.17 (s, 4H).

^{13}C NMR (151 MHz, DMSO) δ 152.38, 150.80, 146.01, 145.93, 128.10, 128.08, 124.17, 124.15, 117.62, 117.58, 114.58, 114.46, 59.19, 47.00, 46.98, 29.57, 24.08.

^{19}F NMR (376 MHz, DMSO) δ -137.83.

(HRMS + TOF MS ES+) calculated $C_{20}H_{24}N_2O_2F_2$: 362.41. observed: 363.1912.

7.4.5.2. Synthesis of 1S,2S Chiral ligand with cyclo-backbone

6,6'-(((1S,2S)-cyclohexane-1,2-diylbis(azanediyl)) bis (methylene)) bis (2-methylphenol)

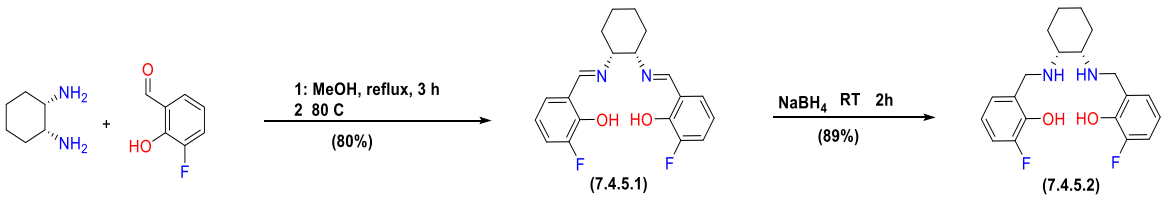

Scheme 7.4.5.2. Synthetic route for the synthesis of the 1S,2S (7.4.5.2.) Chiral ligand.

The named compound was synthesized following the similar protocol as stated above. yellowish solid (1.249g, 3.485mmol, 80% yield) (74.5.1.) and whitish solid (0.904g, 2.494mmol, 89% yield) (7.4.5.2).

^{1}H NMR (600 MHz, DMSO) δ 13.90 (s, 2H), 8.57 (s, 2H), 7.26 – 7.20 (m, 2H), 7.18 (d, *J* = 7.8 Hz, 2H), 6.78 – 6.72 (m, 2H), 3.53 – 3.47 (m, 2H), 1.94 – 1.88 (m, 2H), 1.81 – 1.76 (m, 2H), 1.67 – 1.59 (m, 2H), 1.49 – 1.40 (m, 2H).

^{13}C NMR (151 MHz, DMSO) δ 165.44, 165.42, 151.63, 150.59, 150.51, 150.02, 127.25, 127.23, 120.06, 120.03, 118.75, 118.64, 117.56, 117.52, 70.35, 32.38, 23.74.

^{19}F NMR (376 MHz, DMSO) δ -138.40.

(HRMS + TOF MS ES+) calculated $C_{20}H_{20}N_2O_2F_2$: 358.15. observed: 359.1588.

^{1}H NMR (600 MHz, DMSO) δ 7.01 – 6.96 (m, 2H), 6.90 (d, *J* = 7.6 Hz, 2H), 6.67 – 6.61 (m, 2H), 3.91 (d, *J* = 13.9 Hz, 2H), 3.82 (d, *J* = 13.9 Hz, 2H), 2.43 – 2.37 (m, 2H), 2.00 (d, *J* = 10.3 Hz, 2H), 1.63 (d, *J* = 8.9 Hz, 2H), 1.21 – 1.11 (m, 4H).

^{13}C NMR (151 MHz, DMSO) δ 152.24, 150.65, 145.86, 145.78, 127.97, 127.95, 124.03, 124.01, 117.48, 117.44, 114.44, 114.32, 59.05, 46.85, 29.44, 23.93.

^{19}F NMR (376 MHz, DMSO) δ -137.82.

(HRMS + TOF MS ES+) calculated $C_{20}H_{24}N_2O_2F_2$: 362.41. observed: 363.1873.

7.4.6.2. Synthesis of 1R,2S Chiral ligand with cyclo-backbone

6,6'-(((1R,2S)-cyclohexane-1,2-diylbis(azanediyl)) bis (methylene)) bis (2-methylphenol)

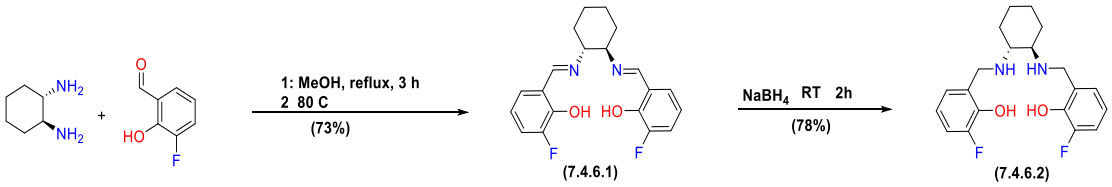

Scheme 7.4.6.2. Synthetic route for the synthesis of the 1S,2R (7.4.6.2.) Chiral ligand.

The name compound was synthesized following similar protocol to obtained yellowish solid (0.571g, 1.594mmol, 73% yield) (74.6.1.) and whitish solid (0.391g, 1.078mmol, 78% yield) (7.4.6.2).

^{1}H NMR (600 MHz, DMSO) δ 13.83 (s, 2H), 8.57 (s, 2H), 7.26 – 7.20 (m, 2H), 7.18 (d, *J* = 7.8 Hz, 2H), 6.78 – 6.72 (m, 2H), 3.55 – 3.47 (m, 2H), 1.95 – 1.89 (m, 2H), 1.82 – 1.77 (m, 2H), 1.66 – 1.61 (m, 2H), 1.50 – 1.41 (m, 2H).

^{13}C NMR (151 MHz, DMSO) δ 165.34, 165.32, 151.50, 150.51, 150.42, 149.89, 127.14, 127.12, 119.91, 119.88, 118.64, 118.53, 117.42, 117.38, 70.17, 32.25, 23.63.

^{19}F NMR (376 MHz, DMSO) δ -138.25.

(HRMS + TOF MS ES+) calculated $C_{20}H_{20}N_2O_2F_2$: 358.15. observed: 359.1588.

^{1}H NMR (600 MHz, DMSO) δ 7.02 – 6.96 (m, 2H), 6.90 (d, *J* = 7.5 Hz, 2H), 6.68 – 6.61 (m, 2H), 3.91 (d, *J* = 13.9 Hz, 2H), 3.82 (d, *J* = 13.9 Hz, 2H), 2.42 – 2.38 (m, 2H), 2.00 (d, *J* = 10.5 Hz, 2H), 1.66 – 1.61 (m, 2H), 1.21 – 1.13 (m, 4H).

^{13}C NMR (151 MHz, DMSO) δ 152.26, 150.67, 145.89, 145.82, 127.96, 124.05, 124.03, 117.48, 117.44, 114.46, 114.34, 59.05, 46.85, 29.44, 23.95.

^{19}F NMR (376 MHz, DMSO) δ -137.84.

(HRMS + TOF MS ES+) calculated $C_{20}H_{24}N_2O_2F_2$: 362.42. observed: 363.1873.

7.4.7.1. Synthesis of symmetric Zn^{2+} complexes. [$ZnOCF_3$(1R.2R)]

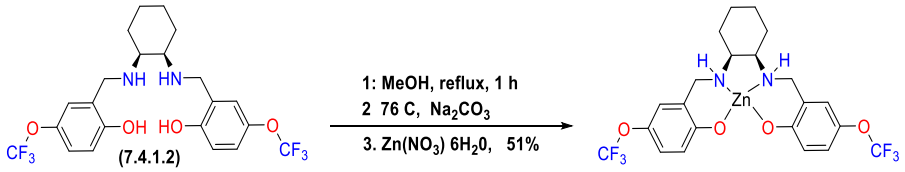

Scheme 7.4.7.1. Synthetic route for the synthesis of the Zinc complex [Zn-1-RR)].

Ligand (50 mg, 0.10mmol, 1eq) of (7.4.1.2) was dissolved in MeOH (5 mL) and stirred at room temperature for 10 minutes to obtain a clear solution before adding zinc nitrate hexahydrate. (60mg, 0.20mmol, 2eq) and seconded with sodium carbonate (11mg, 0.10mmol, 1eq) and the reaction mixture was heated at reflux for 1 hours at 76°C. The mixture was cooled to room temperature and filtered, kept in a vial covered with thin film to allow for slow evaporation and growth of crystals, crystals obtained were whitish and suitable for XRD measurements with 56% yield.

7.4.8.1. Synthesis of symmetric Zn^{2+} complexes. [$ZnOCF_3$(1S.2S)]

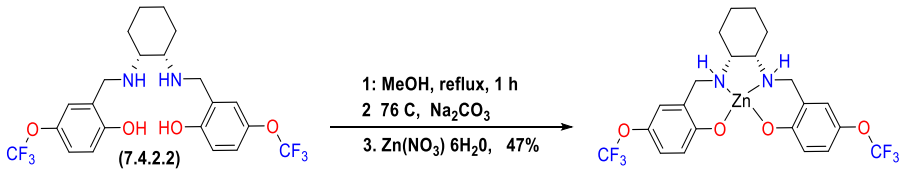

Scheme 7.4.8.1. Synthetic route for the synthesis of the Zinc complex [Zn-1-SS)].

The name Zinc complex of **[$ZnOCF_3$(1S.2S)]** was synthesized following similar protocol to obtained bright whitish coloured needle-like crystals suitable for XRD measurements with 61% yield.

7.4.9.1. Synthesis of symmetric Zn^{2+} complexes. [$ZnOCF_3$(1S.2R)]

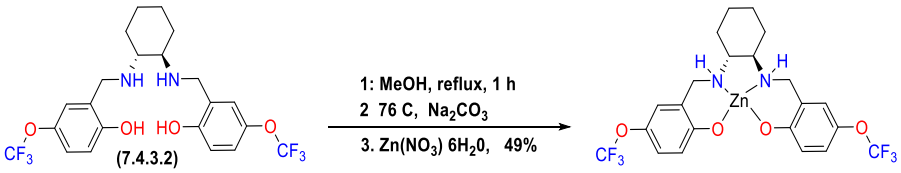

Scheme 7.4.9.1. Synthetic route for the synthesis of the Zinc complex [Zn-1-rac)].

The name Zinc complex of **[ZnOCF$_3$(1S.2R)]** was synthesized following similar protocol to obtained bright whitish coloured needle-like crystals suitable for XRD measurements with 51% yield.

7.4.10.1. Synthesis of symmetric Zn^{2+} complexes. [Zn-F (1R.2R)]

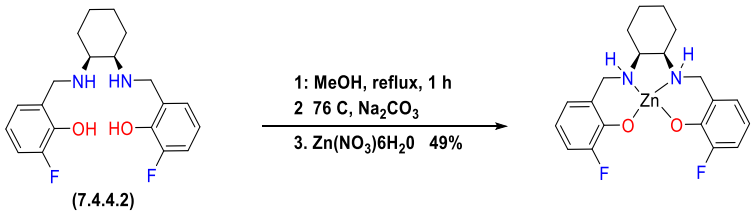

Scheme 7.4.10.1. Synthetic route for the synthesis of the Zinc complex [Zn-2-RR)].

The name Zinc complex of **[Zn-F (1R.2R)]** was synthesized following similar protocol to obtained bright whitish coloured needle-like crystals suitable for XRD measurements with 49% yield.

7.4.11.1. Synthesis of symmetric Zn^{2+} complexes. [Zn-F (1S.2S)]

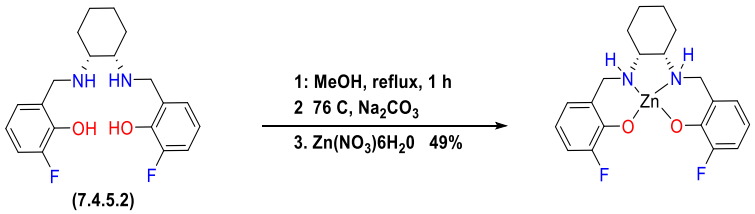

Scheme 7.4.11.1. Synthetic route for the synthesis of the Zinc complex [Zn-2-SS)].

The name Zinc complex of **[Zn-F (1S.2S)]** was synthesized following similar protocol to obtained bright whitish coloured needle-like crystals suitable for XRD measurements with 59% yield.

7.4.12.1. Synthesis of symmetric Zn^{2+} complexes. [Zn-F (1S.2R)]

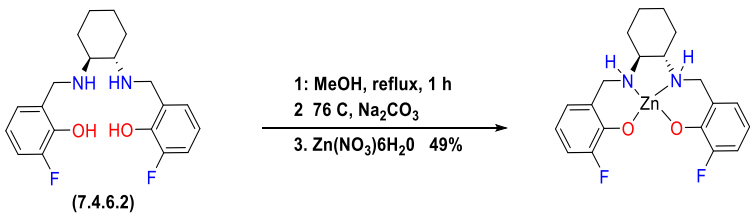

Scheme 7.4.12.1. Synthetic route for the synthesis of the Zinc complex [Zn-2-rac].

The name Zinc complex of **[Zn-F (1S.2R)]** was synthesized following similar protocol to obtained bright whitish coloured needle-like crystals suitable for XRD measurements with 47% yield.

7.5. Chapter 4: Synthetic procedure

7.5.1.2. Synthesis of Half unit for $H_4oct^{(p\text{-}OCF3)}$salox

2-(((2-aminoethyl) amino) methyl)-4-(trifluoromethoxy)phenol

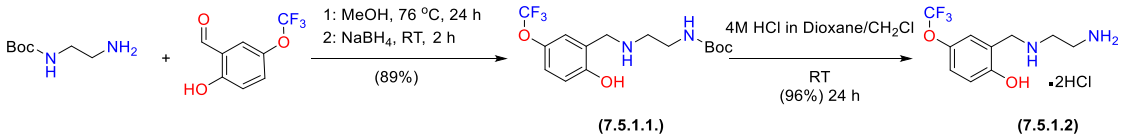

Scheme 7.5.1.2. Synthetic route for the half unit of $H_4oct^{(p\text{-}OCF3)}$salox

The above-named compound was synthesized using a modified procedure as described by Loving et al[362] (1.1mL, 8mmol, 1eq) of 2-hydroxy, 5-trifluoromethoxy benzaldehyde in 15mL of methanol was placed inside a 100mL round bottom flask, and (1.26mL, 8mmol, 1eq) of tertiary butyl carbamate was added and the mixture stirred at reflux for 24 hours, the reaction mixture was cooled to room temperature before adding stepwise $NaBH_4$ (0.908 g, 24 mmol, 3eq) in small portions over 20 minutes. The reaction was further stirred at room temperature for 2 hours before quenching with saturated sodium carbonate (65mL) and extracted with dichloromethane (3 x 50 mL). The combined organic phases were washed with saturated brine (40 mL) and dried over $MgSO_4$. The solvent was evaporated *in vacuo* to obtained (1.983g, 5.66mmol, 71%) of **(7.5.1.1)** as a brownish solid which was used without further purification, (1.632g, 4.659mmol,) of (7.5.1.1) were dissolved in (9mL) of dichloromethane to obtain a clear solution before adding (3mL) of 4N HCL in dioxane solvent ratio and stirred overnight at room temperature, visible formation of white solid was observed, which was filtered, washed with pet ether and dried to obtain the desired white solid.(1.474g, 4.532mmol, 97% yield)

^{1}H NMR (600 MHz, DMSO) δ 7.13 (d, *J* = 3.0 Hz, 1H), 7.07 – 7.02 (m, 1H), 6.85 – 6.80 (m, 1H), 6.77 (d, *J* = 8.7 Hz, 1H), 3.77 (s, 2H), 3.07 – 3.00 (m, 2H), 2.57 – 2.48 (m, 3H), 1.37 (s, 9H).

^{13}C NMR (151 MHz, DMSO) δ 155.95, 155.68, 140.25, 126.43, 121.30, 120.46, 119.45, 115.95, 77.57, 48.98, 48.08, 28.24.

^{19}F NMR (376 MHz, DMSO) δ -57.69.

(HRMS + TOF MS ES+) calculated $C_{15}H_{21}N_2O_4F_3$: 350.34, observed: 351.1538.

^{1}H NMR (600 MHz, DMSO) δ 10.79 (s, 1H), 9.60 (s, 2H), 8.39 (s, 3H), 7.52 (d, *J* = 3.0 Hz, 1H), 7.28 – 7.23 (m, 1H), 7.07 (d, *J* = 8.9 Hz, 1H), 4.14 (s, 2H), 3.37 (s, 2H).

^{13}C NMR (151 MHz, DMSO) δ 155.25, 140.10, 124.46, 123.46, 119.38, 119.23, 116.38, 44.55, 43.89, 35.22.

^{19}F NMR (376 MHz, DMSO) δ -57.22.

(HRMS + TOF MS ES+) calculated $C_{10}H_{13}N_2O_2F_3$: 250.22, observed: 251.0995.

7.5.2.1. Synthesis of the precursor

2-(((2-((2-hydroxy-5-(trifluoromethoxy)benzyl)amino)ethyl)amino)methyl)quinolin-8-ol

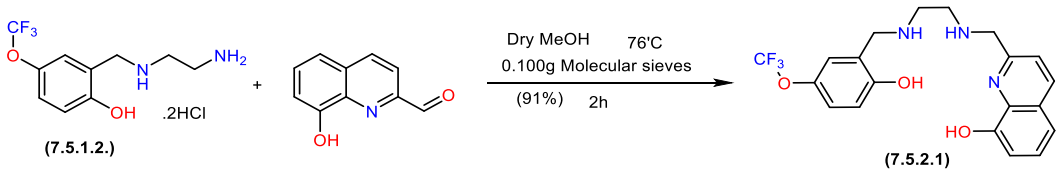

Scheme 7.5.2.1. Synthetic route for the precursor $H_4oct^{(p\text{-}OCF3)}salox$

The above named precursor for water-soluble ligand was synthesized using the modified procedures of Loving[362] and Thiele[363] with one step, (1.000g, 3.093mmol, 1eq) of 2-hydroxy-5-triflouromethoxybenzaldehyde was placed in a 100ml RB flask containing 0.100g activated molecular sieve and dry methanol under stirring at 72°C, (0.862ml, 6.187mmol, 2eq) of triethylamine was added stepwise and stirred for 15 minutes before adding (0.535g, 3.093mmol, 1eq) of 8-Hydroxyquinoline-2-carbaldehyde and refluxed for two hours at 72°C. Upon reaction completion, the solution was allowed to cool to room temperature before adding slowly and stepwise (0.468g, 12.37mmol, 4eq) of sodium borohydride and stirring continuously at room temperature for 2hrs, the reduction process was quenched using 75ml of ice/cold water and 3ml of methanol added and the RBF was left overnight in a Fume hood for the desired compound to crystalize out to obtain a yellowish solid **(7.5.2.1)**.(1.143g, 2.80mmol, 91% yield**).**

^{1}H NMR (600 MHz, DMSO) δ 8.26 – 8.22 (m, 1H), 7.55 – 7.52 (m, 1H), 7.40 – 7.32 (m, 2H), 7.14 – 7.02 (m, 3H), 6.75 (s, 1H), 3.99 (s, 2H), 3.82 (s, 2H), 2.74 – 2.60 (m, 4H).

^{13}C NMR (151 MHz, DMSO) δ 158.70, 156.56, 152.88, 137.47, 136.21, 127.61, 126.81, 126.10, 121.30, 120.97, 120.53, 117.45, 116.10, 111.02, 54.61, 49.55, 48.29, 47.97.

^{19}F NMR (376 MHz, DMSO) δ -57.23.

(HRMS + TOF MS ES+) calculated $C_{20}H_{20}N_3O_3F_3$: 407.39. observed: 407.491.1550.

7.5.3.1. Synthesis of water-soluble ligand

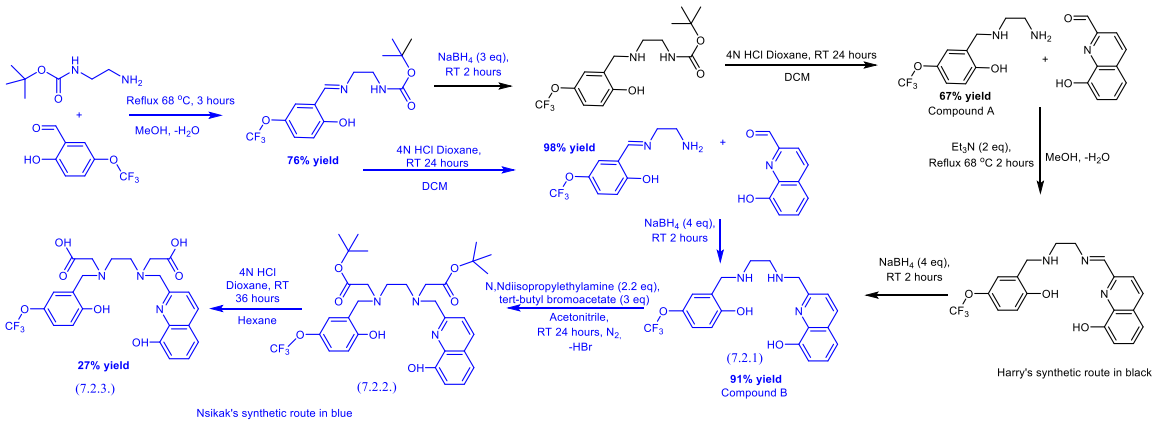

Scheme 7.5.3.1. Synthetic route for the synthesis of $H_4oct^{(p\text{-}OCF3)}salox$

2-((2-((carboxymethyl)((8-hydroxyquinolin-2-yl) methyl) amino) ethyl) (2-hydroxy-5-(trifluoromethoxy)benzyl) amino) acetic acid.

To synthesize **(7.5.3.1.**), (2.00g, 4.91mmol, 1eq) of (**7.5.2.1**.) was dissolved in a 250mL RB flask containing 25mL of dry acetonitrile under stirring for 5 minutes to obtain a clear solution before adding stepwise (1.85mL, 10.8mmol, 2.2eq) of N, N-Diisopropylethylamine as a base under stirred for 10 minutes, then(2.17mL, 14.7mmol, 3eq) of Tert-butyl bromoacetate in 10mL of dry acetonitrile was added slowly to the reaction flask under stirring, the mixture was stirred at room temperature under nitrogen overnight to obtained crude sample, crude sample Purification using CH_2Cl_2 8:2 MeOH and standard reverse face chromatography using water and acetonitrile both containing 0.1% formic acid, the column started with 95% water and 5% acetonitrile and ends at 5% water, 95% acetonitrile to obtained crude of (1.800g, 2.83mmol, 58%) and it was deprotected using Hexane 6:2 TFA and stirred overnight, filtered to obtained bright yellowish oily water-soluble compound. To displaced the TFA to HCl, the water soluble compound (**7.5.3.1**) was dissolved in distilled water and CH_2Cl_2 was added and concentrated through rotary evaporator (x3), finally, three drops of 6M HCl and CH_2Cl_2 was added and concentrated to obtained the pure water soluble

compound(7.2.3)(0.400g, 0.764mmol, 27%) with TFA displaced to HCl and with over 96% purity.

^{1}H NMR (600 MHz, D_2O) δ 8.73 (d, *J* = 8.6 Hz, 1H), 7.75 (d, *J* = 8.6 Hz, 1H), 7.53 (d, *J* = 7.3 Hz, 2H), 7.20 (d, *J* = 6.8 Hz, 1H), 7.04 (s, 1H), 6.93 – 6.83 (m, 1H), 6.39 (d, *J* = 8.9 Hz, 1H), 4.31 – 4.23 (m, 4H), 3.58 (s, 2H), 3.44 (s, 2H), 3.30 (t, *J* = 5.6, 5.6 Hz, 2H), 3.21 (d, *J* = 5.8 Hz, 2H).

^{13}C NMR (151 MHz, D_2O) δ 168.56, 147.34, 130.50, 128.78, 124.99, 124.88, 66.45, 54.73, 54.49.

^{19}F NMR (376 MHz, D_2O) δ -58.55.

(HRMS + TOF MS ES+) calculated $C_{24}H_{24}N_3O_7F_3$: 523.47, observed: 524.1661.

7.6. Chapter 5: Synthetic procedure

7.6.1.1. Synthesis of Symmetric Salen ligands

2,2'-((1E,1'E)-(ethane-1,2-diylbis(azanylylidene))bis(methanylylidene))bis(4-(trifluoromethoxy)phenol)

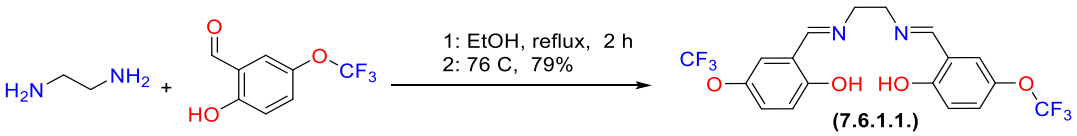

Scheme 7.6.1.1. Synthetic route for the synthesis OCF_3 /OCF_3 (Unreduced)

The above-named compound was synthesized using Davenport[36] procedure with little modifications, ethylenediamine (0.52mL, 8mmol, 1eq) was dissolved in a 100mL RBF containing 20ml of ethanol under stirring, (2.2ml, 16mmol , 2eq) of 2-hydroxy-5-trifluoro methoxy benzaldehyde was added slowly and there was an immediate formation of yellowish solid which re-dissolves shortly on continuous reflux for 2hrs at 76°C, the mixture was placed in an ice bath for 20 minutes and the desired compound was washed with cold ethanol and dried under vacuum to obtained (2.769g, 6.346mmol, 79% yield).

^{1}H NMR (600 MHz, DMSO) δ 13.49 (s, 2H), 8.63 (s, 2H), 7.51 (d, *J* = 3.0 Hz, 2H), 7.35 – 7.30 (m, 2H), 6.95 (d, *J* = 9.0 Hz, 2H), 3.94 (s, 4H).

^{13}C NMR (151 MHz, DMSO) δ 165.84, 159.76, 139.72, 125.76, 123.79, 122.78, 121.09, 119.40, 118.74, 118.17, 117.70, 58.49.

^{19}F NMR (376 MHz, DMSO) δ -57.57.

(HRMS + TOF MS ES+) calculated $C_{18}H_{14}N_2O_4F_6$: 436.31. observed: 437.0948.

7.6.2.1. Synthesis of Symmetric Salan ligands

2,2'-((ethane-1,2-diylbis(azanediyl)) bis (methylene)) bis (4-(trifluoromethoxy)phenol)

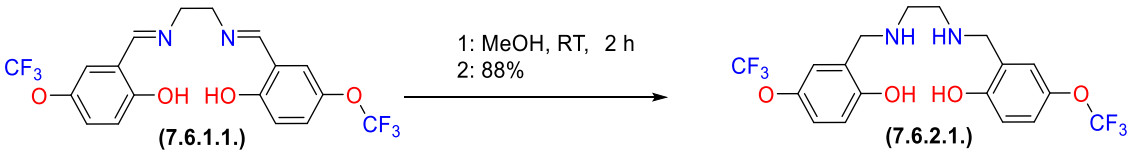

Scheme 7.6.2.1. Synthetic route for the synthesis OCF_3 /OCF_3

Compound (7.6.2.1.) was synthesis by dissolving (1.127g, 2.58mmol, 1eq) of (7.5.1.2) in a 100mL RBF containing 15ml of methanol under stirring at RT to obtained a clear solution before adding sodium borohydride (0.195g, 5.167mmol, 2eq) stepwise and the reaction mixture was stirred for 2hrs at room temperature, the reduction process was quenched using 5ml of ice/cold water and the desired product obtained through suction filtration to have a whitish solid (0.998g, 2.266mmol, 88% yield).

^{1}H NMR (600 MHz, DMSO) δ 7.14 (d, *J* = 3.0 Hz, 2H), 7.05 (dd, *J* = 8.7, 3.0 Hz, 2H), 6.76 (d, *J* = 8.7 Hz, 2H), 3.78 (s, 4H), 2.63 (s, 4H).

^{13}C NMR (151 MHz, DMSO) δ 156.00, 140.21, 126.46, 122.82, 121.32, 121.13, 120.48, 119.45, 115.94, 49.12, 47.62.

^{19}F NMR (376 MHz, DMSO) δ -57.22.

(HRMS + TOF MS ES+) Calculated $C_{18}H_{18}N_2O_4F_6$: 440.34, observed: 441.1256.

7.6.3.1. Synthesis of Half-unit

2-hydroxy-5-(methylthio)benzaldehyde

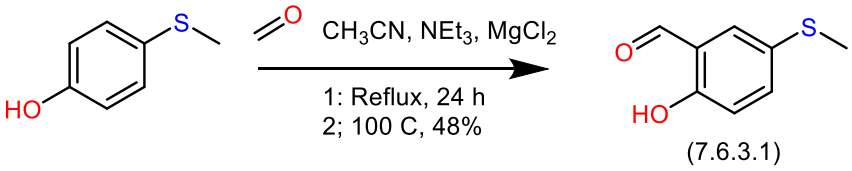

Scheme 7.6.3.1. Synthetic route for the Half-unit

The procedure for the synthesis of (**7.6.3.1**.) was achieve using Duff reaction method following Piel[364] protocol with minor modifications,(4.206g, 30mmol, 1 eq) of 4-methyl thiol phenol , (6.075g, 202.5mmol, 6.75eq) of paraformaldehyde, (4.285g, 45mmol, 1.5% eq)) of anhydrous magnesium chloride and (15.6mL, 112.5mmol, 3.75% eq) of triethylamine were dissolved in 100mL of acetonitrile and reflux overnight at 100°C, the reaction mixture was cool at room temperature, 5mL of with 1M aqueous HCL was added and the organic phase was extracted using Ethyl acetate (3x 15mL), the combine organic phase was washed with brine and dried over $MgSO_4$, the crude was concentrated using rotary evaporator, the crude was purified with column chromatography(Hex 8: Ethyl acetate 2) to have obtained yellowish crystalline solid(2.397g, 14.425mmol, 48%).

^{1}H NMR (600 MHz, cdcl$_3$) δ 10.67 (s, 1H), 9.62 (d, *J* = 0.7 Hz, 1H), 7.28 – 7.24 (m, 2H), 6.73 – 6.69 (m, 1H), 2.23 (s, 3H).

^{13}C NMR (151 MHz, cdcl$_3$) δ 196.36, 160.20, 137.99, 133.56, 128.71, 121.05, 118.68, 18.11.

7.6.4.1. Synthesis of Non-Symmetric Salan ligands

2-(((2-((2-hydroxy-5-(methylthio) benzyl) amino) ethyl) amino) methyl) -4-(trifluoromethoxy)phenol

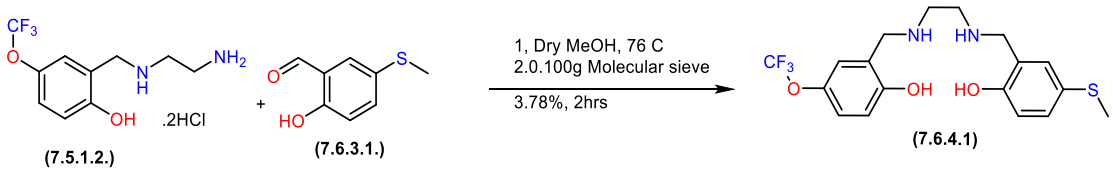

Scheme 7.6.4.1. Synthetic route for the non-Symmetric salen ligand (OCF_3/SCH_3)

The named compound **(7.6.4.1.)** was synthesized following similar protocol as described in (**7.3.2.1**.) to obtained light brown solid (0.631g,1.567mmol, 78%).

^{1}H NMR (600 MHz, DMSO) δ 7.14 (d, *J* = 3.0 Hz, 1H), 7.09 (d, *J* = 2.4 Hz, 1H), 7.07 – 7.02 (m, 2H), 6.76 (d, *J* = 8.7 Hz, 1H), 6.67 (d, *J* = 8.3 Hz, 1H), 3.77 (d, *J* = 9.7 Hz, 4H), 2.62 (s, 4H), 2.37 (s, 3H).

^{13}C NMR (151 MHz, DMSO) δ 156.07, 155.72, 140.19, 128.91, 128.08, 126.44, 125.50, 121.33, 120.48, 119.44, 116.10, 49.81, 49.18, 47.62, 17.20.

^{19}F NMR (376 MHz, DMSO) δ -57.63.

(HRMS + TOF MS ES+) calculated $C_{18}H_{21}N_2O_3F_3S_1$: 402.430, observed: 403.1308.

7.6.5.1. Synthesis of Non-Symmetric Salen ligands

2-(((2-((2-hydroxy-5-(trifluoromethoxy) benzyl) amino) ethyl) amino) methyl)-4-methoxyphenol

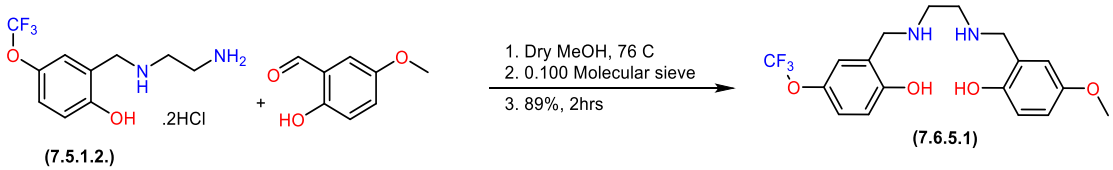

(7.5.1.2.) (7.6.5.1)

Scheme 7.6.5..1. Synthetic route for the non-Symmetric salen ligand (OCF_3/OCH_3)

The name compound **(7.6.5.1.)** was synthesized following similar protocol as described in (**7.3.2.1**.) to

obtained brownish solid (1.051g, 2.721mmol, 89%).

^{1}H NMR (600 MHz, DMSO) δ 7.11 (d, *J* = 3.0 Hz, 1H), 7.07 – 6.99 (m, 1H), 6.74 (d, *J* = 8.7 Hz, 1H), 6.68 (d, *J* = 2.8 Hz, 1H), 6.66 – 6.56 (m, 2H), 3.76 (s, 2H), 3.72 (s, 2H), 3.62 (s, 3H), 2.59 (s, 4H).

^{13}C NMR (151 MHz, DMSO) δ 156.09, 151.84, 150.71, 140.20, 126.42, 125.30, 121.34, 120.50, 115.97, 115.65, 114.20, 112.73, 55.28, 50.09, 49.23, 47.68, 47.59.

^{19}F NMR (376 MHz, DMSO) δ -57.23.

(HRMS + TOF MS ES+) calculated $C_{18}H_{21}N_2O_4F_3$: 386.150, observed: 387.1533.

7.6.6.1. Synthesis of Non-Symmetric Salan ligands

2-(((2-((2-hydroxybenzyl) amino) ethyl) amino) methyl)-4-(trifluoromethoxy)phenol

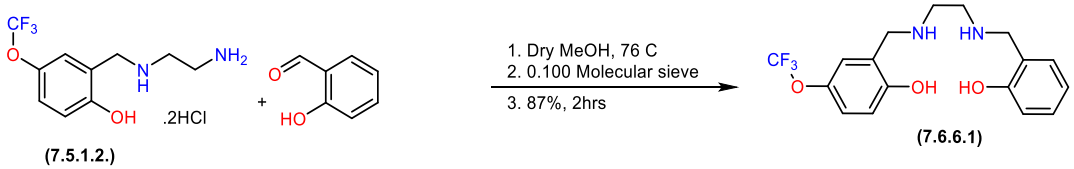

(7.5.1.2.) (7.6.6.1)

Scheme 7.6.6.1. Synthetic route for the non-Symmetric salen ligand (OCF_3/-)

The name compound **(7.6.6.1.)** was synthesized following similar protocol as described in (**7.3.2.1**.) to obtained light yellowish solid (2.239g, 6.283mmol, 87%).

^{1}H NMR (600 MHz, DMSO) δ 7.14 (d, *J* = 3.0 Hz, 1H), 7.07 (s, 1H), 6.79 – 6.67 (m, 2H), 3.79 (d, *J* = 6.4 Hz, 4H), 2.63 (s, 4H).

^{13}C NMR (151 MHz, DMSO) δ 157.30, 156.04, 140.22, 128.62, 127.84, 126.47, 124.33, 121.37, 120.52, 118.47, 115.96, 115.35, 50.28, 49.18, 47.63, 47.55.

^{19}F NMR (376 MHz, DMSO) δ -57.35.

(HRMS + TOF MS ES+) calculated $C_{17}H_{19}N_2O_3F_3$: 356.350, observed: 357.1433.

7.6.7.1. Synthesis of Non-Symmetric Salan ligands

2,4-di-tert-butyl-6-(((2-((2-hydroxy-5-(trifluoromethoxy)benzyl) amino) ethyl) amino) methyl) phenol

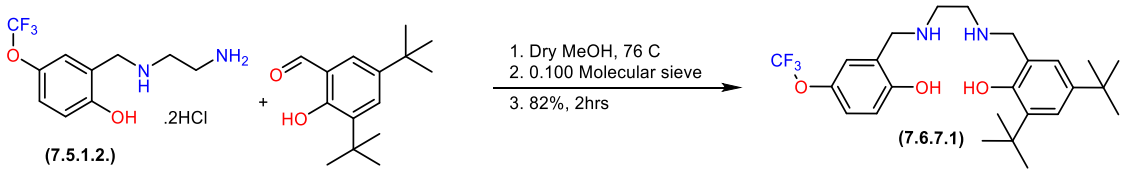

Scheme 7.6.7.1. Synthetic route for the non-Symmetric salen ligand (OCF_3/bis tertiary)

The name compound **(7.6.7.1.)** was synthesized following similar protocol as described in (**7.3.2.1**.) to obtained light yellowish solid (0.831g, 1.774mmol, 82%).

^{1}H NMR (600 MHz, DMSO) δ 7.18 (d, *J* = 2.8 Hz, 1H), 7.07 (q, *J* = 5.0, 4.4, 4.4 Hz, 2H), 6.88 (d, *J* = 2.2 Hz, 1H), 6.82 – 6.77 (m, 1H), 3.85 (s, 2H), 3.81 (s, 2H), 2.70 (d, *J* = 3.6 Hz, 4H), 1.34 (s, 9H), 1.22 (s, 9H).

^{13}C NMR (151 MHz, DMSO) δ 155.98, 155.86, 154.66, 140.28, 139.81, 139.35, 134.53, 126.63, 126.50, 123.08, 122.51, 77.64, 48.98, 48.12, 47.36, 45.74, 34.45, 33.80, 31.86, 31.65, 31.60, 31.57, 29.54, 29.43, 28.29, 11.70.

^{19}F NMR (376 MHz, DMSO) δ -57.32.

(HRMS + TOF MS ES+) calculated $C_{25}H_{35}N_2O_3F_3$: 468.260, observed: 469.2684.

7.6.8.1. Synthesis of Symmetric Salen ligands

2,2'-((1E,1'E) -(ethane-1,2-diylbis(azanylylidene))bis(methanylylidene))bis(3-fluorophenol)

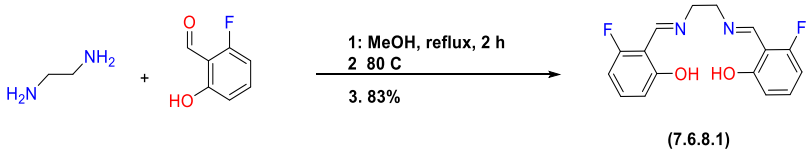

Scheme 7.6.8.1. Synthetic route for the non-Symmetric salen ligand (F/F) Unreduced

The name compound **(7.6.8.1.)** was synthesized following similar protocol as described in (**7.3.2.1**.) to obtained a light yellowish solid (1.105g, 3.630mmol, 83%).

^{1}H NMR (600 MHz, DMSO) δ 8.80 (s, 2H), 7.33 (td, *J* = 8.3, 8.3, 6.7 Hz, 2H), 6.69 (d, *J* = 8.5 Hz, 2H), 6.67 – 6.61 (m, 2H), 3.98 (s, 4H).

^{13}C NMR (151 MHz, DMSO) δ 163.45, 163.42, 162.58, 160.91, 160.73, 160.68, 133.99, 133.91, 113.53, 113.51, 107.02, 106.94, 104.05, 103.91, 57.91, 39.88.

^{19}F NMR (376 MHz, DMSO) δ -121.52.

(HRMS + TOF MS ES+) calculated $C_{16}H_{14}N_2O_2F_2$: 304.290, observed: 305.1112.

7.6.9.1. Synthesis of Symmetric Salan ligands

2,2'-((ethane-1,2-diylbis(azanediyl)) bis (methylene))bis(3-fluorophenol)

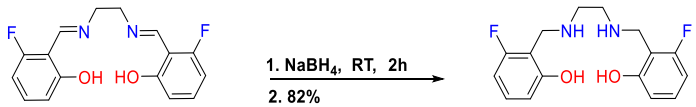

(7.6.8.1) (7.6.9.1)

Scheme 7.6.9.1. Synthetic route for the non-Symmetric salen ligand (F/F)

The name compound **(7.6.9.1.)** was synthesized following similar protocol as described in (**7.3.2.1**.) to obtained light yellowish solid (0.583g, 1.890mmol, 82%).

^{1}H NMR (600 MHz, DMSO) δ 7.07 (q, *J* = 7.8, 7.8, 7.8 Hz, 2H), 6.55 (t, *J* = 8.8, 8.8 Hz, 4H), 3.84 (s, 4H), 2.63 (s, 4H).

^{13}C NMR (151 MHz, DMSO) δ 161.65, 160.05, 159.36, 159.31, 128.60, 128.52, 111.69, 111.68, 111.52, 111.40, 105.19, 105.04, 47.30, 42.44, 42.41.

^{19}F NMR (376 MHz, DMSO) δ -118.98.

(HRMS + TOF MS ES+) calculated $C_{16}H_{18}N_2O_2F_2$: 308.370, observed: 309.1424.

7.6.10.1. Synthesis of symmetric Zn^{2+} complexes. [Zn-(OCF_3/OCF_3)]

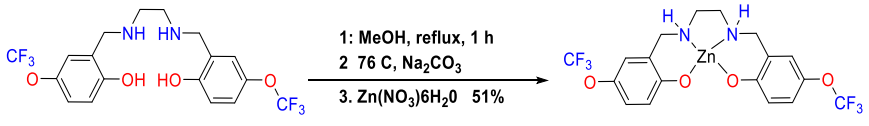

(7.6.2.1)

Scheme 7.6.10.1. Synthetic route for the synthesis of the Zinc complex [Zn-(OCF_3/OCF_3)].

Zinc complex for the new novel salen ligand was synthesized using (50 mg, 0.113mmol, 1eq) of (7.5.2.1) was dissolved in MeOH (5 mL) and stirred at room temperature for 10 minutes to obtain a clear solution, Zinc nitrate hexahydrate. (34mg, 0.113mmol, 1eq) and seconded with sodium carbonate (12mg, 0.113mmol, 1eq) and the reaction mixture was reflux for 1 hours at 76°C. The mixture was cooled to room temperature and filtered, kept in a vial covered with perforated thin film to allow for slow evaporation and growth of crystals, crystals obtained were whitish and suitable for XRD measurements.

7.6.11.1. Synthesis of Non-Symmetric Zn^{2+} complexes. [Zn-(OCF_3/SCH_3)]

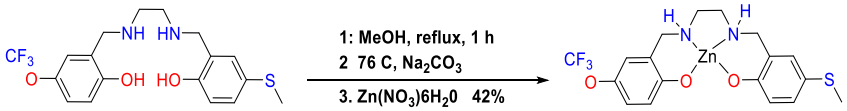

(7.6.4.1)

Scheme 7.6.11.1. Synthetic route for the synthesis of the Zinc complex [Zn-(OCF_3/SCH_3)].

The name Zinc complex of **[Zn-(OCF3/SCH_3)]** was synthesized following similar protocol to obtained bright whitish coloured needle-like crystals suitable for XRD measurements.

7.6.12.1. Synthesis of Non-Symmetric Zn^{2+} complexes. [Zn-(OCF_3/OCH_3)]

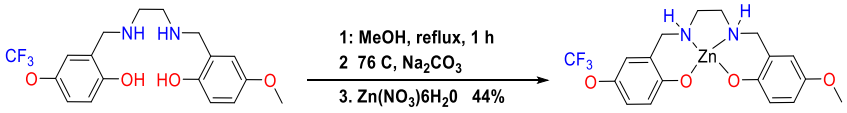

(7.6.5.1)

Scheme 7.6.12.1. Synthetic route for the synthesis of the Zinc complex [Zn-(OCF_3/OCH_3)].

The name Zinc complex of **[Zn-(OCF3/OCH_3)]** was synthesized following similar protocol to obtained bright whitish coloured needle-like crystals suitable for XRD measurements.

7.6.14.1. Synthesis of Non-Symmetric Zn^{2+} complexes. [Zn-(bis-tert-OCF_3)]

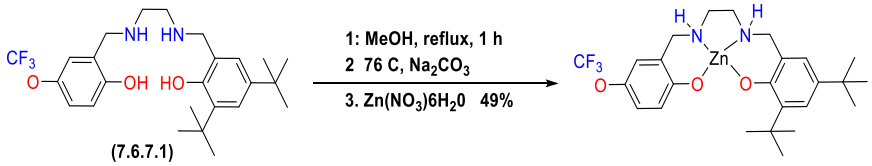

(7.6.7.1)

Scheme 7.6.14.1. Synthetic route for the synthesis of the Zinc complex [Zn-(bis-tert-OCF_3)]

The name Zinc complex of **[**Zn-(bis-tert-OCF_3)] was synthesized following a similar protocol to obtained bright whitish coloured needle-like crystals suitable for XRD measurements.

7.6.15.1. Synthesis of Non-Symmetric Zn^{2+} complexes. [Zn-(F/F)]

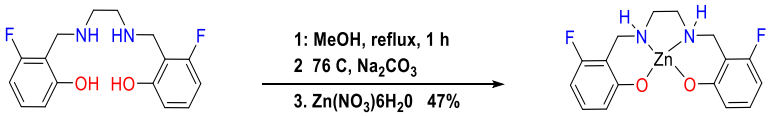

(7.6.9.1)

Scheme 7.6.15.1. Synthetic route for the synthesis of the Zinc complex [Zn-(F/F)]

The name Zinc complex of **[**Zn-(F/F)] was synthesized following similar protocol to obtained bright whitish coloured needle-like crystals suitable for XRD measurements.

8. Chapter 8. References

1 A. W. Kleij, *Eur. J. Inorg. Chem.*, 2009, 2009, 193–205.
2 V. K. Gupta, A. K. Singh and B. Gupta, *Anal. Chim. Acta*, 2006, **575**, 198–204.
3 J. S. Johnson and D. a Evans, *Acc. Chem. Res.*, 2000, **33**, 325–335.
4 E. N. Jacobsen, *Acc. Chem. Res.*, 2000, **33**, 421–431.
5 S. B. Ogunwumi and T. Bein, *Chem. Commun.*, 1997, 901–902.
6 T. D. Pasatoiu, A. M. Madalan, M. U. Kumke, C. Tiseanu and M. Andruh, *Inorg. Chem.*, 2010, **49**, 2310–2315.
7 U. Schatzschneider, *Inorganica Chim. Acta*, 2011, **374**, 19–23.
8 C. W. Schwietert and J. P. McCue, *Coord. Chem. Rev.*, 1999, **184**, 67–89.
9 S. Medici, M. Peana, G. Crisponi, V. M. Nurchi, J. I. Lachowicz, M. Remelli and M. A. Zoroddu, *Coord. Chem. Rev.*, 2016, **327**–**328**, 349–359.
10 B. R. Jagirdar, *Resonance*, 1999, **4**, 63–81.
11 E. B. Bauer, *Chem. Soc. Rev.*, 2012, **41**, 3153–3167.
12 J. Karges, R. W. Stokes and S. M. Cohen, *Trends Chem.*, 2021, **3**, 523–534.
13 J. Berrones Reyes, M. K. Kuimova and R. Vilar, *Curr. Opin. Chem. Biol.*, 2021, **61**, 179–190.
14 M. Strianese and C. Pellecchia, *Coord. Chem. Rev.*, 2016, **318**, 16–28.
15 Q. Zhang and K. M. C. Wong, *Coord. Chem. Rev.*, 2020, **416**, 213336.
16 K. B. Bischoff, 1965, **42**, 1965.
17 C. J. Elsevier, J. Reedijk, P. H. Walton and M. D. Ward, *Dalton Trans.*, 2003, 1869–1880.
18 S. Arata, K. Suzuki, K. Yamaguchi and Y. Sunada, *Dalt. Trans.*, 2020, **49**, 17537–17541.
19 C. Sarma, P. K. Chaurasia and S. L. Bharati, *Russ. J. Gen. Chem.*, 2019, **89**, 517–531.
20 B. Ali and M. A. Iqbal, *ChemistrySelect*, 2017, **2**, 1586–1604.
21 Z. Hua, V. C. Vassar, H. Choi and I. Ojima, *Proc. Natl. Acad. Sci. U. S. A.*, 2004, **101**, 5411–5416.
22 F. Tümer, S. A. Güngör, M. Köse, F. Koçer and M. Tümer, *J. Mol. Struct.*, , DOI:10.1016/j.molstruc.2019.127059.
23 C. Li, H. Yu, Z. Lin, F. Wang, N. Zhang and J. Wang, *J. Coord. Chem.*, 2017, **70**, 1303–1315.
24 B. Gao, R. Duan, X. Pang, X. Li, Z. Qu, H. Shao, X. Wang and X. Chen, *Dalt. Trans.*, 2013, **42**, 16334–16342.
25 J. Kuwabara, T. Namekawa, M. A. Haga and T. Kanbara, *Dalt. Trans.*, 2012, **41**, 44–46.
26 M. U. Anwar, A. Al-Harrasi and J. M. Rawson, *Dalt. Trans.*, 2021, **50**, 5099–5108.
27 A. Ratnam, M. Bala, R. Kumar, U. P. Singh and K. Ghosh, *J. Organomet. Chem.*, 2018, **856**, 41–49.
28 J. I. Van Der Vlugt and J. N. H. Reek, *Angew. Chemie - Int. Ed.*, 2009, **48**, 8832–8846.
29 H. M. Mousa, M. A. Mahmoud, A. S. Yasin and I. M. A. Mohamed, *J. Coatings Technol. Res.*, 2021, **18**, 1191–1197.
30 E. Gravel, C. Tanguy, E. Cassette, T. Pons, F. Knittel, N. Bernards, A. Garofalakis, F. Ducongé, B. Dubertret and E. Doris, *Chem. Sci.*, 2013, **4**, 411–417.
31 P. W. N. M. Van Leeuwen, P. C. J. Kamer, J. N. H. Reek and P. Dierkes, *Chem. Rev.*, 2000, **100**, 2741–2769.
32 E. Hao, Z. Wang, L. Jiao and S. Wang, *Dalt. Trans.*, 2010, **39**, 2660–2666.

33 L. Fourteau, E. Benoist and M. Dartiguenave, *Synlett*, 2001, 126–128.

34 T. Hosseinzadeh Sanatkar, A. Khorshidi, E. Sohouli and J. Janczak, *Inorganica Chim. Acta*, 2020, **506**, 119537.

35 P. K. Chow, C. Ma, W. P. To, G. S. M. Tong, S. L. Lai, S. C. F. Kui, W. M. Kwok and C. M. Che, *Angew. Chemie - Int. Ed.*, 2013, **52**, 11775–11779.

36 J. Devonport, J. Spencer and G. E. Kostakis, *Dalton Trans.*, 2021, **50**, 12069–12073.

37 S. Akine, *J. Incl. Phenom. Macrocycl. Chem.*, 2012, **72**, 25–54.

38 M. Azam, Z. Hussain, I. Warad, S. I. Al-Resayes, M. S. Khan, M. Shakir, A. Trzesowska-Kruszynska and R. Kruszynski, *Dalt. Trans.*, 2012, **41**, 10854–10864.

39 M. Holbach, X. Zheng, C. Burd, C. W. Jones and M. Weck, *J. Org. Chem.*, 2006, **71**, 2903–2906.

40 S. Kloß, D. Selent, A. Spannenberg, R. Franke, A. Börner and M. Sharif, *Catalysts*, , DOI:10.3390/catal9121036.

41 A. Böttcher, H. Elias, E. G. Jäger, H. Langfelderova, M. Mazur, L. Müller, H. Paulus, P. Pelikan, M. Rudolph and M. Valko, *Inorg. Chem.*, 1993, **32**, 4131–4138.

42 J. C. Pessoa and I. Correia, *Coord. Chem. Rev.*, 2019, **388**, 227–247.

43 L. Zhao, M. Hermann, N. Holzmann and G. Frenking, *Coord. Chem. Rev.*, 2017, **344**, 163–204.

44 G. A. Lawrance, *Introduction to Coordination Chemistry*, 2009.

45 A. Nandi and S. Kozuch, *Chem. - A Eur. J.*, 2020, **26**, 759–772.

46 R. G. Pearson, *Inorg. Chem.*, 1988, **27**, 734–740.

47 C. Cárdenas and P. W. Ayers, *Phys. Chem. Chem. Phys.*, 2013, **15**, 13959–13968.

48 U. Ndagi, N. Mhlongo and M. E. Soliman, *Drug Des. Devel. Ther.*, 2017, **11**, 599–616.

49 K. Barabas, R. Milner, D. Lurie and C. Adin, *Vet. Comp. Oncol.*, 2008, **6**, 1–18.

50 S. Komeda, .

51 D. L. Ma, V. P. Y. Ma, D. S. H. Chan, K. H. Leung, H. Z. He and C. H. Leung, *Coord. Chem. Rev.*, 2012, **256**, 3087–3113.

52 N. P. Ebosie, M. O. C. Ogwuegbu, G. O. Onyedika and F. C. Onwumere, *Biological and analytical applications of Schiff base metal complexes derived from salicylidene-4-aminoantipyrine and its derivatives: a review*, Springer Berlin Heidelberg, 2021, vol. 18.

53 V. Fernández-Moreira, F. L. Thorp-Greenwood and M. P. Coogan, *Chem. Commun.*, 2010, **46**, 186–202.

54 M. R. Dubois, *Chem. Rev.*, 1989, **89**, 1–9.

55 O. Gutten and L. Rulíšek, *Inorg. Chem.*, 2013, **52**, 10347–10355.

56 E. Rodríguez, J. L. Arqués, R. Rodríguez, M. Nuñez, M. Medina, T. L. Talarico, I. A. Casas, T. C. Chung, W. J. Dobrogosz, L. Axelsson, S. E. Lindgren, W. J. Dobrogosz, L. Kerkeni, P. Ruano, L. L. Delgado, S. Picco, L. Villegas, F. Tonelli, M. Merlo, J. Rigau, D. Diaz and M. Masuelli, *Intech*, 1989, **32**, 137–144.

57 D. M. Janrao, J. Pathan, D. D. Kayande and J. J. Mulla, *Sci. Revs. Chem. Commun*, 2014, **4**, 11–24.

58 E. S. S. A, A. Sabatini, A. Vacca and T. Uni-, *Time*, 1976, **18**, 237–239.

59 Z. Y. Tao, Z. J. Guo and W. M. Dong, *J. Radioanal. Nucl. Chem.*, 2003, **256**, 575–580.

60 Y. Xu and D. Zhao, *Ind. Eng. Chem. Res.*, 2006, **45**, 7380–7387.

61 J. Champion, C. Alliot, S. Huclier, D. Deniaud, Z. Asfari and G. Montavon, *Inorganica Chim. Acta*, 2009, **362**, 2654–2661.

62 Giorgi Makharadze, Nazi Goliadze, Tamar Makharadze and Guram Supatashvili, *J.*

Chem. Chem. Eng., 2014, **8**, 344–348.
63 N. Tanaka and H. Ogino, *Bull. Chem. Soc. Jpn.*, 1961, **34**, 1040–1045.
64 J. H. Christie and R. A. Osteryoung, *J. Am. Chem. Soc.*, 1960, **82**, 1841–1844.
65 A. G. Assefa, M. T. Negash, M. L. Akele, B. M. Anteneh, A. A. Mesfin, P. Shyamala and G. N. Rao, *SSRN Electron. J.*, 2021, 1–17.
66 H. A. Mayer and W. C. Kaska, *Chem. Rev.*, 1994, **94**, 1239–1272.
67 G. P. Lu, K. R. Voigtritter, C. Cai and B. H. Lipshutz, *J. Org. Chem.*, 2012, **77**, 3700–3703.
68 R. J. Lundgren and M. Stradiotto, in *Ligand Design in Metal Chemistry*, John Wiley & Sons, Ltd, 2016, pp. 1–14.
69 M. D. Godbole, A. C. G. Hotze, R. Hage, A. M. Mills, H. Kooijman, A. L. Spek and E. Bouwman, *Inorg. Chem.*, 2005, **44**, 9253–9266.
70 D. Parker, E. A. Suturina, I. Kuprov and N. F. Chilton, *Acc. Chem. Res.*, 2020, **53**, 1520–1534.
71 R. D. Hancock and A. E. Martell, *Chem. Rev.*, 1989, **89**, 1875–1914.
72 K. Koyasu, J. Atobe, M. Akutsu, M. Mitsui and A. Nakajima, *J. Phys. Chem. A*, 2007, **111**, 42–49.
73 J. Ulises Reveles and S. N. Khanna, *Phys. Rev. B - Condens. Matter Mater. Phys.*, 2006, **74**, 1–6.
74 A. Bose, I. Thomas and E. Abraham, *Int. J. Adv. Pharm. Anal.*, 2018, **8**, 1–8.
75 M. C. D. Santos, J. D. Monteiro, J. M. G. Araújo and K. M. G. Lima, *Sci. Rep.*, 2020, **10**, 1–13.
76 A. Romani, C. Clementi, C. Miliani and G. Favaro, *Acc. Chem. Res.*, 2010, **43**, 837–846.
77 J. A. Gardecki and M. Maroncelli, *Appl. Spectrosc.*, 1998, **52**, 1179–1189.
78 M. Sameiro and T. Gonçalves, *Chem. Rev.*, 2009, **109**, 190–212.
79 J. Feng, X. Chen, Q. Han, H. Wang, P. Lu and Y. Wang, *J. Lumin.*, 2011, **131**, 2775–2783.
80 M. C. Vlasiou and K. S. Pafiti, *Spectrochim. Acta - Part A Mol. Biomol. Spectrosc.*, 2020, **241**, 1–9.
81 N. Ullah, M. Mansha, I. Khan and A. Qurashi, *TrAC - Trends Anal. Chem.*, 2018, **100**, 155–166.
82 M. G. Boersma, T. Y. Dinarieva, W. J. Middelhoven, W. J. H. Van Berkel, J. Doran, J. Vervoort and I. M. C. M. Rietjens, *Appl. Environ. Microbiol.*, 1998, **64**, 1256–1263.
83 D. Rose-Sperling, M. A. Tran, L. M. Lauth, B. Goretzki and U. A. Hellmich, *Biol. Chem.*, 2019, **400**, 1277–1288.
84 M. A. Danielson and J. J. Falke, *Annu. Rev. Biophys. Biomol. Struct.*, 1996, **25**, 163–195.
85 L. P. Picard and R. S. Prosser, *Curr. Opin. Struct. Biol.*, 2021, **69**, 169–176.
86 A. O. Okaru, T. S. Brunner, S. M. Ackermann, T. Kuballa, S. G. Walch, M. Kohl-Himmelseher and D. W. Lachenmeier, *J. Anal. Methods Chem.*, , DOI:10.1155/2017/9206297.
87 G. J. Nesbitt, *TrAC Trends Anal. Chem.*, 1992, **11**, XVIII.
88 N. J. Greenfield, *Nat. Protoc.*, 2007, **1**, 2876–2890.
89 S. S. Andrews and J. Tretton, *J. Chem. Educ.*, 2020, **97**, 4370–4376.
90 B. Ranjbar and P. Gill, *Chem. Biol. Drug Des.*, 2009, **74**, 101–120.
91 D. Leung, S. O. Kang and E. V Anslyn, *Chem. Soc. Rev.*, 2012, **41**, 448–79.
92 A. J. Miles, R. W. Janes and B. A. Wallace, *Chem. Soc. Rev.*, 2021, **50**, 8400–8413.

93 E. R. Morris, D. A. Rees, G. R. Sanderson and D. Thom, *J. Chem. Soc. Perkin Trans. 2*, 1975, 1418–1425.

94 D. S. Hassan, F. Y. Thanzeel and C. Wolf, *Chirality*, 2020, **32**, 457–463.

95 Y. D. Liang and J. F. Song, *J. Pharm. Biomed. Anal.*, 2005, **38**, 100–106.

96 Q. Zhen, B. Xu, L. Ma, G. Tian, X. Tang and M. Ding, *Clin. Biochem.*, 2011, **44**, 226–230.

97 A. V. Colnaghi Simionato, E. P. Moraes, E. Carrilho, M. F. M. Tavares and E. Kenndler, *Electrophoresis*, 2008, **29**, 2051–2058.

98 E. Zor, I. Hatay Patir, H. Bingol and M. Ersoz, *Biosens. Bioelectron.*, 2013, **42**, 321–325.

99 G. Verma and M. Mishra, *World J. Pharm. Res.*, 2018, **7**, 1170–1180.

100 R. Gandhimathi, S. Vijayaraj and M. P. Jyothirmaie, *Int. J. Pharm. Res. Anal.*, 2012, **2**, 72–78.

101 J. quinc. Brown, 2010, **20**, 119–131.

102 R. Begum, Z. H. Farooqi, K. Naseem, F. Ali, M. Batool, J. Xiao and A. Irfan, *Crit. Rev. Anal. Chem.*, 2018, **48**, 503–516.

103 L. Gunti, R. S. Dass and N. K. Kalagatur, *Front. Microbiol.*, 2019, **10**, 1–17.

104 A. Ahmed, A. Singh, B. Padha, A. K. Sundramoorthy, A. Tomar and S. Arya, *Chemosphere*, 2022, **303**, 135208.

105 S. Behzadi, F. Ghasemi, M. Ghalkhani, A. A. Ashkarran, S. M. Akbari, S. Pakpour, M. R. Hormozi-Nezhad, Z. Jamshidi, S. Mirsadeghi, R. Dinarvand, F. Atyabi and M. Mahmoudi, *Nanoscale*, 2015, **7**, 5134–5139.

106 N. Norazmi, Z. R. A. Rasad, M. Mohamad and H. Manap, *IOP Conf. Ser. Mater. Sci. Eng.*, , DOI:10.1088/1757-899X/257/1/012031.

107 L. D. S. Yadav, *Org. Spectrosc.*, 2005, 7–51.

108 P. A. Kobielska, A. J. Howarth, O. K. Farha and S. Nayak, *Coord. Chem. Rev.*, 2018, **358**, 92–107.

109 Y. Hu, X. Liu, J. Bai, K. Shih, E. Y. Zeng and H. Cheng, *Environ. Sci. Pollut. Res.*, 2013, **20**, 6150–6159.

110 B. Wei and L. Yang, *Microchem. J.*, 2010, **94**, 99–107.

111 U. Farooq, J. A. Kozinski, M. A. Khan and M. Athar, *Bioresour. Technol.*, 2010, 101, 5043–5053.

112 H. Huang, R. Chen, J. Ma, L. Yan, Y. Zhao, Y. Wang, W. Zhang, J. Fan and X. Chen, *Chem. Commun.*, 2014, **50**, 15415–15418.

113 R. P. Schwarzenbach, T. Egli, T. B. Hofstetter, U. Von Gunten and B. Wehrli, *Annu. Rev. Environ. Resour.*, 2010, **35**, 109–136.

114 T. Wu, C. Liu, B. Kong, J. Sun, Y. Gong, K. Liu, J. Xie, A. Pei and Y. Cui, *ACS Cent. Sci.*, 2019, **5**, 719–726.

115 J. Briffa, E. Sinagra and R. Blundell, *Heliyon*, 2020, **6**, e04691.

116 R. A. Wuana and F. E. Okieimen, *ISRN Ecol.*, 2011, **2011**, 1–20.

117 M. Jaishankar, T. Tseten, N. Anbalagan, B. B. Mathew and K. N. Beeregowda, *Interdiscip. Toxicol.*, 2014, 7, 60–72.

118 V. Singh, P. C. Mondal, A. K. Singh and M. Zharnikov, *Coord. Chem. Rev.*, 2017, **330**, 144–163.

119 J. A. Buledi, S. Amin, S. I. Haider, M. I. Bhanger and A. R. Solangi, *Environ. Sci. Pollut. Res.*, 2020, 1–9.

120 B. Kaur, R. Srivastava and B. Satpati, *New J. Chem.*, 2015, **39**, 5137–5149.

121 K. J. Lohmann, *Nature*, 1993, **362**, 703.

122 X. Dai, O. Nekraseova, M. E. Hyde and R. G. Compton, *Anal. Chem.*, 2004, **76**,

5924–5929.
123 T. G. Moga, *Nat. Chem.*, 2012, **4**, 334.
124 S. K. Mustafa and M. A. AlSharif, *Am. J. Anal. Chem.*, 2018, **09**, 15–26.
125 I. Abdulazeez, C. Basheer and A. A. Al-Saadi, *RSC Adv.*, 2018, **8**, 39983–39991.
126 H. H. Wang, L. Xue, Z. J. Fang, G. P. Li and H. Jiang, *New J. Chem.*, 2010, **34**, 1239–1242.
127 M. Ghaedi, J. Tashkhourian, M. Montazerozohori, M. Nejati Biyareh and B. Sadeghian, *Arab. J. Chem.*, 2017, **10**, S2319–S2326.
128 F. A. Nicholson, B. J. Chambers, F. Nicholson, A. Gleadthorpe and M. Vale Mansfield, *SP0547: Sources and Impacts of Past, Current and Future Contamination of Soil Appendix 1 : Heavy metals*, 2007.
129 I. Ii. Ali, Hazrat, E. Khan and I. Ilahi, 2019, **2019**, 14.
130 R. Ricco, K. Konstas, M. J. Styles, J. J. Richardson, R. Babarao, K. Suzuki, P. Scopece and P. Falcaro, *J. Mater. Chem. A*, 2015, **3**, 19822–19831.
131 N. Lubick and D. Malakoff, *Science (80-.).*, 2013, **341**, 1443–1445.
132 N. E. Bagshaw, *J. Power Sources*, 1995, **53**, 25–30.
133 J. Larminie and J. Lowry, *James Larminie, John Lowry(auth.)-Electric Vehicle Technology Explained, Second Edition (2012).pdf*, 2012.
134 S. Vazquez, S. M. Lukic, E. Galvan, L. G. Franquelo and J. M. Carrasco, *IEEE Trans. Ind. Electron.*, 2010, **57**, 3881–3895.
135 H. Needleman, *Annu. Rev. Med.*, 2004, **55**, 209–222.
136 J. Goel, K. Kadirvelu, C. Rajagopal and V. K. Garg, *J. Hazard. Mater.*, 2005, **125**, 211–220.
137 Y. Jiao, J. Zhang, L. Zhang, Z. Lin, C. He and C. Duan, *Chem. Commun.*, 2012, **48**, 6022–6024.
138 I. W. G. on the Evaluation of Carcinogenic Risks to Humans, *IARC Monogr. Eval. Carcinog. Risks Hum.*, 2012, **100**, 11–465.
139 N. Rawal, *The characteristics, toxicity and effects of cadmium Blessy Baby Mathew Dayananda Sagar Institutions*, .
140 J. Wu, J. Lu, T. Chen, Z. He, Y. Su, X. Jin and X. Yao, *Environ. Earth Sci.*, 2010, **60**, 421–429.
141 I. A. Darwish and D. A. Blake, *Anal. Chem.*, 2001, **73**, 1889–1895.
142 J. Shao, J. D. Gu, L. Peng, S. Luo, H. Luo, Z. Yan and G. Wu, *J. Hazard. Mater.*, 2014, **272**, 83–88.
143 K. S. Rao, M. Mohapatra, S. Anand and P. Venkateswarlu, *Review on cadmium removal from aqueous solutions*, 2010, vol. 2.
144 T. M. Swager and K. A. Mirica, *Chem. Rev.*, 2019, **119**, 1–2.
145 M. Porchia, M. Pellei, F. Del Bello and C. Santini, *Molecules*, 2020, **25**, 5814.
146 L. Häggman, C. Lindblad, A. Cassel and I. Persson, *J. Solution Chem.*, 2020, **49**, 1279–1289.
147 J. A. Drewry and P. T. Gunning, *Coord. Chem. Rev.*, 2011, **255**, 459–472.
148 T. Li, S. Schulz and P. W. Roesky, *Chem. Soc. Rev.*, 2012, **41**, 3759–3771.
149 M. Strianese, D. Guarnieri, M. Lamberti, A. Landi, A. Peluso and C. Pellecchia, *Inorg. Chem.*, 2020, **59**, 15977–15986.
150 M. Musterman, .
151 T. Dudev and C. Lim, *J. Am. Chem. Soc.*, 2000, **122**, 11146–11153.
152 T. Hayashi, T. Aya, M. Nonoguchi, T. Mizutani, Y. Hisaeda, S. Kitagawa and H. Ogoshi, *Tetrahedron*, 2002, **58**, 2803–2811.
153 G. Li, X. Zhao, L. Wang and W. Liu, *ChemistrySelect*, 2019, **4**, 9317–9321.

154 A. Sano, S. Yasuda and T. Akitsu, *Res. Rev. J. Med. Org. Chem.*, 2016, **3**, 21–22.
155 T. Scrnitic, 2015, 19–20.
156 C. Ribeiro, C. Santos, V. Gonçalves, A. Ramos, C. Afonso and M. E. Tiritan, *Molecules*, , DOI:10.3390/molecules23020262.
157 G. Q. Lin, J. G. Zhang and J. F. Cheng, *Chiral Drugs Chem. Biol. Action*, 2011, 3–28.
158 J. Ma, X. Zhang, X. Huang, S. Luo and E. Meggers, *Nat. Protoc.*, 2018, **13**, 605–632.
159 X. Niu, X. Yang, H. Li, J. Liu, Z. Liu and K. Wang, *Microchim. Acta*, 2020, **187**, 676.
160 Y. Hou, Z. Liu, L. Tong, L. Zhao, X. Kuang, R. Kuang and H. Ju, *Dalton Trans.*, 2019, **49**, 31–34.
161 X. Yu, L. He, M. Pentok, H. Yang, Y. Yang, Z. Li, N. He, Y. Deng, S. Li, T. Liu, X. Chen and H. Luo, *Nanoscale*, 2019, **11**, 15589–15595.
162 L. A. Warning, A. R. Miandashti, L. A. McCarthy, Q. Zhang, C. F. Landes and S. Link, *ACS Nano*, 2021, **15**, 15538–15566.
163 K. W. Bentley and C. Wolf, *J. Am. Chem. Soc.*, 2013, **135**, 12200–12203.
164 E. G. Shcherbakova, V. Brega, T. Minami, S. Sheykhi, T. D. James and P. Anzenbacher, *Chem. Eur. J.*, 2016, **22**, 10074–10080.
165 Z. A. De los Santos, S. MacAvaney, K. Russell and C. Wolf, *Angew. Chemie Int. Ed.*, 2020, **59**, 2440–2448.
166 Z. A. De los Santos, C. C. Lynch and C. Wolf, *Angew. Chemie Int. Ed.*, 2019, **58**, 1198–1202.
167 K. W. Bentley, D. Proano and C. Wolf, *Nat. Commun.*, 2016, **7**, 12539.
168 J. M. Dragna, G. Pescitelli, L. Tran, V. M. Lynch, E. V. Anslyn and L. Di Bari, *J. Am. Chem. Soc.*, 2012, **134**, 4398–4407.
169 W. Yang, K. R. Cadwallader, Y. Liu, M. Huang and B. Sun, *Food Chem.*, 2019, **282**, 153–163.
170 Z. Liu, Y. Xu, C. Y. Ji, S. Chen, X. Li, X. Zhang, Y. Yao and J. Li, *Adv. Mater.*, 2020, **32**, 1–9.
171 S. R. Chaudhari and N. Suryaprakash, *Org. Biomol. Chem.*, 2012, **10**, 6410–6419.
172 Z. Xu, C. Liu, S. Zhao, S. Chen and Y. Zhao, *Chem. Rev.*, 2019, 119, 195–230.
173 Z. Chen, M. Yang, Z. Sun, X. Zhang, J. Xu, G. Bian and L. Song, *Anal. Chem.*, 2019, **91**, 14591–14596.
174 C. Dong, Z. Xu, L. Wen, S. He, J. Wu, Q. H. Deng and Y. Zhao, *Anal. Chem.*, 2021, **93**, 2968–2973.
175 M. S. Seo and H. Kim, *J. Am. Chem. Soc.*, 2015, **137**, 14190–14195.
176 C. M. Puentes and T. J. Wenzel, *Beilstein J. Org. Chem.*, 2017, **13**, 43–53.
177 Z. Sun, Z. Chen, Y. Wang, X. Zhang, J. Xu, G. Bian and L. Song, *Org. Lett.*, 2020, **22**, 589–593.
178 C. C. Hinckley, *J. Am. Chem. Soc.*, 1969, **91**, 5160–5162.
179 J. A. Dale, D. L. Dull and H. S. Mosher, *J. Org. Chem.*, 1969, **34**, 2543–2549.
180 W. H. Pirkle, D. L. Sikkenga and M. S. Pavlin, *J. Org. Chem.*, 1977, 42, 384–387.
181 J. Bravo, C. Cativiela, J. E. Chaves, R. Navarro and E. P. Urriolabeitia, *Inorg. Chem.*, 2003, **42**, 1006–1013.
182 J. X. Yu, R. R. Hallac, S. Chiguru and R. P. Mason, *Prog. Nucl. Magn. Reson. Spectrosc.*, 2013, **70**, 25–49.
183 J. Yu, V. Kodibagkar, W. Cui and R. Mason, *Curr. Med. Chem.*, 2005, **12**, 819–848.
184 E. N. G. Marsh and Y. Suzuki, *ACS Chem. Biol.*, 2014, 9, 1242–1250.
185 Y. Zhao and T. M. Swager, *J. Am. Chem. Soc.*, 2015, **137**, 3221–3224.
186 Y. Zhao, L. Chen and T. M. Swager, *Angew. Chemie Int. Ed.*, 2016, **55**, 917–921.
187 W. Wang, X. Xia, G. Bian and L. Song, *Chem. Commun.*, 2019, **55**, 6098–6101.

188 M. S. Chan and S. Da Huang, *Talanta*, 2000, **51**, 373–380.
189 T. Wen, F. Qu, N. B. Li and H. Q. Luo, *Arab. J. Chem.*, 2017, **10**, S1680–S1685.
190 J. Plastino, E. L. Green, J. Sanders-Loehr and J. P. Klinman, *Biochemistry*, 1999, **38**, 8204–8216.
191 Y. R. Kim, H. J. Kim, J. S. Kim and H. Kim, *Adv. Mater.*, 2008, **20**, 4428–4432.
192 Y. Zhou, S. Wang, K. Zhang and X. Jiang, *Angew. Chemie*, 2008, **120**, 7564–7566.
193 P. Chen, J. Bell, B. A. Eipper and E. I. Solomon, *Biochemistry*, 2004, **43**, 5735–5747.
194 Z. Yuan, N. Cai, Y. Du, Y. He and E. S. Yeung, *Anal. Chem.*, 2014, **86**, 419–426.
195 B. C. Dickinson and C. J. Chang, *Nat. Chem. Biol.*, 2011, **7**, 504–511.
196 N. Houstis, E. D. Rosen and E. S. Lander, *Nature*, 2006, **440**, 944–948.
197 J. Wu and E. A. Boyle, *Anal. Chem.*, 1997, **69**, 2464–2470.
198 M. C. Hsiang, Y. H. Sung and S. Da Huang, *Talanta*, 2004, **62**, 791–799.
199 J. Otero-Romaní, A. Moreda-Piñeiro, A. Bermejo-Barrera and P. Bermejo-Barrera, *Anal. Chim. Acta*, 2005, **536**, 213–218.
200 W. Yang, E. Chow, G. D. Willett, D. B. Hibbert and J. J. Gooding, *Analyst*, 2003, **128**, 712–718.
201 N. A. A. Qasem, R. H. Mohammed and D. U. Lawal, *Clean Water*, 2021, **4**, 1–15.
202 C. Yang, J. Tian, F. Jiang, Q. Chen and M. Hong, *Chem. Rec.*, 2021, **21**, 1455–1472.
203 W. Shi, W. Li, W. Nguyen, W. Chen, J. Wang and M. Chen, *Mater. Today Adv.*, 2022, **15**, 100273.
204 M. Senila, E. Neag, O. Cadar, E. D. Kovacs, I. Aschilean and M. H. Kovacs, *Molecules*, 2022, **27**, 3938.
205 N. Elboughdiri, *Cogent Eng.*, 2020, **7**, 1782623.
206 K. He, Y. Chen, Z. Tang and Y. Hu, *Environ. Sci. Pollut. Res.*, 2016, **23**, 2778–2788.
207 F. N. Muya, C. E. Sunday, P. Baker and E. Iwuoha, *Water Sci. Technol.*, 2016, **73**, 983–992.
208 T. N. Dharmapriya, D. Y. Li, Y. C. Chung and P. J. Huang, *ACS Omega*, 2021, **6**, 30478–30487.
209 Z. Wang, A. Sim, J. J. Urban and B. Mi, *Environ. Sci. Technol.*, 2018, **52**, 9741–9748.
210 I. Sheet, A. Kabbani and H. Holail, *Energy Procedia*, 2014, **50**, 130–138.
211 M. Royanudin, Y. Utomo and S. Wonorahardjo, in *AIP Conference Proceedings*, AIP Publishing LLC AIP Publishing, 2021, vol. 2353, p. 030123.
212 D. T. Quang and J. S. Kim, *Chem. Rev.*, 2010, **110**, 6280–6301.
213 B. Si and E. Song, *Chemosensors*, 2018, **6**, 1–24.
214 R. I. Teleanu, A. G. Niculescu, E. Roza, O. Vladâcenco, A. M. Grumezescu and D. M. Teleanu, *Int. J. Mol. Sci.*, , DOI:10.3390/ijms23115954.
215 T. Pradhan, H. S. Jung, J. H. Jang, T. W. Kim, C. Kang and J. S. Kim, *Chem. Soc. Rev.*, 2014, **43**, 4684–4713.
216 C. F. Valenzuela, M. P. Puglia and S. Zucca, *Alcohol Res. Heal.*, 2011, **34**, 106–120.
217 M. Perry, Q. Li and R. T. Kennedy, *Anal. Chim. Acta*, 2009, **653**, 1–22.
218 E. Başar and B. Güntekin, *Brain Res.*, 2008, **1235**, 172–193.
219 H. Gunduz-Bruce, *Brain Res. Rev.*, 2009, **60**, 279–286.
220 G. Maris, 2018.
221 A. Zapata, V. I. Chefer, T. S. Shippenberg and L. Denoroy, *Detection and quantification of neurotransmitters in dialysates*, 2009.
222 O. Niwa, R. Kurita, T. Horiuchi and K. Torimitsu, *Anal. Chem.*, 1998, **70**, 89–93.
223 O. A. Emuedo, G. O. Anoliefo and C. O. Emuedo, *Glob. J. Hum. - Soc. Sci. B Geogr. Geo-Sciences, Environ. Disaster Manag.*, 2014, **14**, 1–9.
224 A. O. Babatunde, *J. Contemp. African Stud.*, 2020, **38**, 274–293.

225 J. K. Nduka and O. E. Orisakwe, *Environ. Sci. Pollut. Res.*, 2011, **18**, 237–246.
226 A. Galadima and Z. N. Garba, *Elixir Pollut.*, 2012, **45**, 7917–7922.
227 Y. Shimazaki, in *Pure and Applied Chemistry*, Walter de Gruyter GmbH, 2014, vol. 86, pp. 163–172.
228 H. Nagae, R. Aoki, S. N. Akutagawa, J. Kleemann, R. Tagawa, T. Schindler, G. Choi, T. P. Spaniol, H. Tsurugi, J. Okuda and K. Mashima, *Angew. Chemie - Int. Ed.*, 2018, **57**, 2492–2496.
229 S. M. Kirk, P. McKeown, M. F. Mahon, G. Kociok-Köhn, T. J. Woodman and M. D. Jones, *Eur. J. Inorg. Chem.*, 2017, 5417–5426.
230 L. Chiang, K. Herasymchuk, F. Thomas and T. Storr, *Inorg. Chem.*, 2015, **54**, 5970–5980.
231 A. Thevenon, J. A. Garden, A. J. P. White and C. K. Williams, *Inorg. Chem.*, 2015, **54**, 11906–11915.
232 S. I. Sampani, V. Zdorichenko, M. Danopoulou, M. C. Leech, K. Lam, A. Abdul-Sada, B. Cox, G. J. Tizzard, S. J. Coles, A. Tsipis and G. E. Kostakis, *Dalton Trans.*, 2020, **49**, 289–299.
233 S. Di Bella, *Dalt. Trans.*, 2021, **50**, 6050–6063.
234 R. Xu, L. Hua, X. Li, Y. Yao, X. Leng and Y. Chen, *Dalt. Trans.*, 2019, **48**, 10565–10573.
235 T. Nakamura, S. Tsukuda and T. Nabeshima, *J. Am. Chem. Soc.*, 2019, **141**, 6462–6467.
236 G. Salassa, M. J. J. Coenen, S. J. Wezenberg, B. L. M. Hendriksen, S. Speller, J. A. A. W. Elemans and A. W. Kleij, *J. Am. Chem. Soc.*, 2012, **134**, 7186–7192.
237 I. Caretti, E. Carter, I. A. Fallis, D. M. Murphy and S. Van Doorslaer, *Phys. Chem. Chem. Phys.*, 2011, **13**, 20427–20434.
238 D. M. Murphy, I. Caretti, E. Carter, I. A. Fallis, M. C. Göbel, J. Landon, S. Van Doorslaer and D. J. Willock, *Inorg. Chem.*, 2011, **50**, 6944–6955.
239 B. Agrahari, S. Layek, R. Ganguly and D. D. Pathak, *New J. Chem.*, 2018, **42**, 13754–13762.
240 S. Mouri, Z. Chen, H. Mitsunuma, M. Furutachi, S. Matsunaga and M. Shibasaki, *J. Am. Chem. Soc.*, 2010, **132**, 1255–1257.
241 S. Shaw and J. D. White, *Chem. Rev.*, 2019, **119**, 9381–9426.
242 K. Matsumoto, H. Egami, T. Oguma, T. Katsuki, P. Hildebrandt, K. Hildenbrand, E. Bothe, K. Wieghardt, H. Bögge and T. Glaser, *Chem. Commun.*, 2012, **48**, 5823.
243 K. Matsumoto, B. Saito and T. Katsuki, *Chem. Commun.*, 2007, 3619–3627.
244 S. Hozumi, S. Honda, T. Arie, S. Akita and K. Takei, *ACS Sensors*, 2021, **6**, 1918–1924.
245 A. K. Muthusamy, C. H. Kim, S. C. Virgil, H. J. Knox, J. S. Marvin, A. L. Nichols, B. N. Cohen, D. A. Dougherty, L. L. Looger and H. A. Lester, *J. Am. Chem. Soc.*, 2022, **144**, 8480–8486.
246 N. Das Saha, S. Pradhan, R. Sasmal, A. Sarkar, C. M. Berač, J. C. Kölsch, M. Pahwa, S. Show, Y. Rozenholc, Z. Topçu, V. Alessandrini, J. Guibourdenche, V. Tsatsaris, N. Gagey-Eilstein and S. S. Agasti, *J. Am. Chem. Soc.*, 2022, **144**, 14363–14379.
247 D. G. J. Smethurst and N. Shcherbik, *J. Biol. Chem.*, 2021, **297**, 101374.
248 K. Kostenkova, G. Scalese, D. Gambino and D. C. Crans, *Curr. Opin. Chem. Biol.*, 2022, **69**, 102155.
249 J. H. Viles, *Coord. Chem. Rev.*, 2012, **256**, 2271–2284.
250 C. Hureau, *Coord. Chem. Rev.*, 2012, **256**, 2164–2174.
251 G. Perry, A. D. Cash and M. A. Smith, *J. Biomed. Biotechnol.*, 2002, **2002**, 120–123.

252 C. Cheignon, M. Tomas, D. Bonnefont-Rousselot, P. Faller, C. Hureau and F. Collin, *Redox Biol.*, 2018, **14**, 450–464.

253 M. Pohanka, *Curr. Med. Chem.*, 2013, **21**, 356–364.

254 Y. Tong, B. Liu, Y. Wu, B. Yang, G. Wen, Y. T. Yang, J. Chai and X. Hu, *Sensors Actuators, B Chem.*, 2017, **252**, 794–802.

255 P. Yadav, O. Blacque, A. Roodt and F. Zelder, *Inorg. Chem. Front.*, 2021, **8**, 4313–4323.

256 E. Y. L. Hui, D. W. P. Tay, J. A. Richard, Z. Pohancenikova, K. Renault, A. Romieu and Y. H. Lim, *Dye. Pigment.*, 2022, **207**, 110708.

257 B. Das, M. Dolai, A. Dhara, S. Mabhai, A. Jana, S. Dey and A. Misra, *Anal. Sci. Adv.*, 2021, **2**, 447–463.

258 P. Ju, Q. Su, Z. Liu, X. Li, B. Guo, W. Liu, G. Li and Q. Wu, *J. Mater. Sci.*, 2019, **54**, 851–861.

259 A. Jayaraj, M. S. Gayathri, G. Sivaraman and C. A. S. P, *J. Photochem. Photobiol. B Biol.*, 2022, **226**, 112371.

260 T. Zhu, Q. Gou, Y. Yang, Y. Zhang and M. Chen, *J. Mol. Struct.*, 2022, **1264**, 133258.

261 F. Song, X. Ma, J. Hou, X. Huang, Y. Cheng and C. Zhu, *Polymer (Guildf).*, 2011, **52**, 6029–6036.

262 F. Li, L. Li, W. Yang, L. S. Zheng, Z. J. Zheng, K. Jiang, Y. Lu and L. W. Xu, *Tetrahedron Lett.*, 2013, **54**, 1584–1588.

263 A. Böttcher, H. Elias, L. Müller and H. Paulus, *Angew. Chem. Int. Ed.*, 1992, **31**, 623–625.

264 J. Devonport, N. Bodnár, A. McGown, M. Bukar Maina, L. C. Serpell, C. Kállay, J. Spencer and G. E. Kostakis, *Inorg. Chem.*, 2021, **60**, 15310–15320.

265 M. H. Ihde, G. Covey, A. D. G. Johnson, F. R. Fronczek, K. J. Wallace and M. Bonizzoni, *Dalt. Trans.*, 2022, **51**, 14079–14087.

266 P. Wang, K. Yao, J. Fu, Y. Chang, B. Li and K. Xu, *Spectrochim. Acta - Part A Mol. Biomol. Spectrosc.*, 2019, **211**, 9–17.

267 L. F. Wei, C. Y. Chen, C. K. Lai, N. Thirumalaivasan and S. P. Wu, *Methods*, 2019, **168**, 18–23.

268 J. Nandre, S. Patil, V. Patil, F. Yu, L. Chen, S. Sahoo, T. Prior, C. Redshaw, P. Mahulikar and U. Patil, *Biosens. Bioelectron.*, 2014, **61**, 612–617.

269 X. Yang, X. Liu, Y. Li, F. Wu, J. Mao, Y. Yuan, Y. Cui, G. Sun and G. Zhang, *Biosens. Bioelectron.*, 2016, **80**, 288–293.

270 A. Pandith, J. H. Choi, O. S. Jung and H. S. Kim, *Inorganica Chim. Acta*, 2018, **482**, 669–680.

271 B. Lim, B. Baek, K. Jang, N. K. Lee, J. H. Lee, Y. Lee, J. Kim, S. W. Kang, J. Park, S. Kim, N. W. Kang, S. Hong, D. D. Kim, I. Kim, H. Hwang and J. Lee, *Dye. Pigment.*, 2019, **169**, 51–59.

272 T. Simon, M. Shellaiah, V. Srinivasadesikan, C. C. Lin, F. H. Ko, K. W. Sun and M. C. Lin, *Sensors Actuators, B Chem.*, 2016, **231**, 18–29.

273 L. Cai, B. M. Segal, J. R. Long, M. J. Scott and R. H. Holm, *J. Am. Chem. Soc.*, 1995, **117**, 8863–8864.

274 R. Shi, W. Hou, Z. Q. Wang and X. Xu, *Front. Cell Dev. Biol.*, 2021, **9**, 2676.

275 M. P. Mitoraj, A. Michalak and T. Ziegler, *J. Chem. Theory Comput.*, 2009, **5**, 962–975.

276 T. Lu and F. Chen, *J. Comput. Chem.*, 2012, **33**, 580–592.

277 E. Zor, H. Bingol and M. Ersoz, *Trends Anal. Chem.*, 2019, **121**, 115662.

278 X. Liang, W. Liang, P. Jin, H. Wang, W. Wu and C. Yang, *Chemosensors*, 2021, **9**, 1–

23.
279 F. Burg, S. Breitenlechner, C. Jandl and T. Bach, *Chem. Sci.*, 2020, **11**, 2121–2129.
280 C. Wolf and K. W. Bentley, *Chem. Soc. Rev.*, 2013, **42**, 5408–5424.
281 C. M. Kisukuri and L. H. Andrade, *Org. Biomol. Chem.*, 2015, **13**, 10086–10107.
282 S. R. Laplante, L. D. Fader, K. R. Fandrick, D. R. Fandrick, O. Hucke, R. Kemper, S. P. F. Miller and P. J. Edwards, *J. Med. Chem.*, 2011, **54**, 7005–7022.
283 R. Jayakumar, R. Vadivel and N. Ananthi, *Org. Med. Chem. Int. J.*, 2018, **5**, 1–6.
284 D. W. Armstrong, C. D. Chang and W. Y. Li, *J. Agric. Food Chem.*, 1990, **38**, 1674–1677.
285 N. Kelly, K. Schnaars, K. Gloe, T. Doert, J. J. Weigand and K. Gloe, *Aust. J. Chem.*, 2017, **70**, 601–607.
286 A. L. Singer and D. A. Atwood, *Inorg Chim Acta*, 1998, **277**, 157–162.
287 H. Adams, N. A. Bailey, D. E. Fenton, I. G. Ford, S. J. Kitchen, M. G. Williams, P. A. Tasker, A. J. Leong and L. F. Lindoy, *J. Chem. Soc. Dalt. Trans.*, 1991, 1665–1674.
288 M. Karmakar, A. Frontera and S. Chattopadhyay, *CrystEngComm*, 2020, **22**, 6876–6885.
289 H. R. Wen, J. J. Hu, K. Yang, J. L. Zhang, S. J. Liu, J. S. Liao and C. M. Liu, *Inorg. Chem.*, 2020, **59**, 2811–2824.
290 S. Bunda, N. V. May, D. Bonczidai-Kelemen, A. Udvardy, H. Y. V. Ching, K. Nys, M. Samanipour, S. Van Doorslaer, F. Joó and N. Lihi, *Inorg. Chem.*, 2021, **60**, 11259–11272.
291 S. Bunda, K. Voronova, Á. Kathó, A. Udvardy and F. Joó, *Molecules*, 2020, **25**, 3993.
292 N. Lihi, S. Bunda, A. Udvardy and F. Joó, *J. Inorg. Biochem.*, 2020, **203**, 110945.
293 F. H. Allen, *Acta Crystallogr. Sect. B-Structural Sci.*, 2002, **58**, 380–388.
294 J. Dong, C. Tan, K. Zhang, Y. Liu, P. J. Low, J. Jiang and Y. Cui, *J. Am. Chem. Soc.*, 2017, **139**, 1554–1564.
295 C. He, J. Wang, P. Wu, L. Jia, Y. Bai, Z. Zhang and C. Duan, *Chem. Commun.*, 2012, **48**, 11880–11882.
296 C. He, Z. Lin, Z. He, C. Duan, C. Xu, Z. Wang and C. Yan, *Angew. Chemie - Int. Ed.*, 2008, **47**, 877–881.
297 Y. Liu, X. Wu, C. He, Z. Li and C. Duan, *Dalt. Trans.*, 2010, **39**, 7727–7732.
298 Y. Li, L. Wen, H. Meng, J. Lv, G. Luo and Y. Zhao, *Cell Reports Phys. Sci.*, 2020, **1**, 100100.
299 A. W. Addison, T. N. Rao, J. Reedijk, J. Van Rijn and G. C. Verschoor, *J. Chem. Soc. Dalt. Trans.*, 1984, 1349–1356.
300 R. Evans, Z. Deng, A. K. Rogerson, A. S. McLachlan, J. J. Richards, M. Nilsson and G. A. Morris, *Angew. Chemie - Int. Ed.*, 2013, **52**, 3199–3202.
301 P. Pracht, F. Bohle and S. Grimme, *Phys. Chem. Chem. Phys.*, 2020, **22**, 7169–7192.
302 M. J. Frisch, G. W. Trucks, H. B. Schlegel, G. E. Scuseria, M. A. Robb, J. R. Cheeseman, G. Scalmani, V. Barone, G. A. Petersson, H. Nakatsuji, X. Li, M. Caricato, A. V. Marenich, J. Bloino, B. G. Janesko, R. Gomperts, B. Mennucci, H. P. Hratchian, J. V. Ortiz, A. F. Izmaylov, J. L. Sonnenberg, D. Williams, F. Ding, F. Lipparini, F. Egidi, J. Goings, B. Peng, A. Petrone, T. Henderson, D. Ranasinghe, V. G. Zakrzewski, J. Gao, N. Rega, G. Zheng, W. Liang, M. Hada, M. Ehara, K. Toyota, R. Fukuda, J. Hasegawa, M. Ishida, T. Nakajima, Y. Honda, O. Kitao, H. Nakai, T. Vreven, K. Throssell, J. A. Montgomery Jr., J. E. Peralta, F. Ogliaro, M. J. Bearpark, J. J. Heyd, E. N. Brothers, K. N. Kudin, V. N. Staroverov, T. A. Keith, R. Kobayashi, J. Normand, K. Raghavachari, A. P. Rendell, J. C. Burant, S. S. Iyengar, J. Tomasi, M. Cossi, J. M. Millam, M. Klene, C. Adamo, R. Cammi, J. W. Ochterski, R. L. Martin,

K. Morokuma, O. Farkas, J. B. Foresman and D. J. Fox, 2016, Gaussian 16, Revision C.01, Gaussian, Inc., Wallin.
303 P. J. Stephens, F. J. Devlin, C. F. Chabalowski and M. J. Frisch, *J. Phys. Chem.*, 1994, **98**, 11623–11627.
304 C. Lee, W. Yang and R. G. Parr, *Phys. Rev. B*, 1988, **37**, 785–789.
305 A. D. Becke, *J. Chem. Phys.*, 1993, **98**, 5648–5652.
306 S. Grimme, *J. Comput. Chem.*, 2006, **27**, 1787–1799.
307 R. Ditchfield, W. J. Hehre and J. A. Pople, *J. Chem. Phys.*, 1971, **54**, 724–728.
308 P. C. Hariharan and J. A. Pople, *Theor. Chim. Acta*, 1973, **28**, 213–222.
309 M. Dolg, U. Wedig, H. Stoll and H. Preuss, *J. Chem. Phys.*, 1987, **86**, 866–872.
310 G. Scalmani and M. J. Frisch, *J. Chem. Phys.*, 2010, **132**, 114110.
311 J. Tomasi, B. Mennucci and R. Cammi, *Chem. Rev.*, 2005, **105**, 2999–3093.
312 M. Besora and F. Maseras, *Wiley Interdiscip. Rev. Comput. Mol. Sci.*, 2018, **8**, e1372.
313 R. Pérez-Soto, M. Besora and F. Maseras, *Org. Lett.*, 2020, **22**, 2873–2877.
314 Z. Wu, D. Lin and Y. Li, *Nat. Rev. Neurosci.*, 2022, **23**, 257–274.
315 S. D. Niyonambaza, P. Kumar, P. Xing, J. Mathault, P. De Koninck, E. Boisselier, M. Boukadoum and A. Miled, *Appl. Sci.*, 2019, **9**, 4719.
316 R. B. Kelly, *Cell*, 1993, **72**, 43–53.
317 A. Mobed, M. Hasanzadeh, A. Ahmadalipour and A. Fakhari, *Anal. Methods*, 2020, **12**, 557–575.
318 K. S. Hettie, J. L. Klockow and T. E. Glass, *J. Am. Chem. Soc.*, 2014, **136**, 4877–4880.
319 A. V. Leopold, D. M. Shcherbakova and V. V. Verkhusha, *Front. Cell. Neurosci.*, 2019, **13**, 474.
320 I. Hossain, C. Tan, P. T. Doughty, G. Dutta, T. A. Murray, S. Siddiqui, L. Iasemidis and P. U. Arumugam, *Front. Neurosci.*, 2018, **12**, 500.
321 A. Masharina, L. Reymond, D. Maurel, K. Umezawa and K. Johnsson, *J. Am. Chem. Soc.*, 2012, **134**, 19026–19034.
322 J. S. Marvin, Y. Shimoda, V. Magloire, M. Leite, T. Kawashima, T. P. Jensen, I. Kolb, E. L. Knott, O. Novak, K. Podgorski, N. J. Leidenheimer, D. A. Rusakov, M. B. Ahrens, D. M. Kullmann and L. L. Looger, *Nat. Methods*, 2019, **16**, 763–770.
323 A. P. Prescot, J. J. Prisciandaro, S. R. Miller, G. Ingenito, D. G. Kondo and P. F. Renshaw, *Sci. Reports 2018 81*, 2018, **8**, 1–12.
324 P. Hermann, J. Kotek, V. Kubíček and I. Lukeš, *Dalt. Trans.*, 2008, **0**, 3027–3047.
325 S. Rast, A. Borel, L. Helm, E. Belorizky, P. H. Fries and A. E. Merbach, *J. Am. Chem. Soc.*, 2001, **123**, 2637–2644.
326 G. Angelovski, *Angew. Chem. Int. Ed.*, 2016, **55**, 7038–7046.
327 R. Pujales-Paradela, T. Savić, D. Esteban-Gómez, G. Angelovski, F. Carniato, M. Botta and C. Platas-Iglesias, *Chem. - A Eur. J.*, 2019, **25**, 4782–4792.
328 F. Oukhatar, S. V. Eliseeva, C. S. Bonnet, M. Placidi, N. K. Logothetis, S. Petoud, G. Angelovski and É. Tóth, *Inorg. Chem.*, 2019, **58**, 13619–13630.
329 O. Toljić and G. Angelovski, *Chem. Commun.*, 2019, **55**, 11924–11927.
330 F. Oukhatar, H. Meudal, C. Landon, N. K. Logothetis, C. Platas-Iglesias, G. Angelovski and É. Tóth, *Chem. - A Eur. J.*, 2015, **21**, 11226–11237.
331 F. Oukhatar, S. Même, W. Même, F. Szeremeta, N. K. Logothetis, G. Angelovski and É. Tóth, *ACS Chem. Neurosci.*, 2015, **6**, 219–225.
332 G. Angelovski and É. Tóth, *Chem. Soc. Rev.*, 2017, **46**, 324–336.
333 S. Hirano, N. Kodama, K. Shibata and K. T. Suzuki, *Toxicol. Appl. Pharmacol.*, 1993, **121**, 224–232.

334 B. J. Tickner, G. J. Stasiuk, S. B. Duckett and G. Angelovski, *Chem. Soc. Rev.*, 2020, **49**, 6169–6185.

335 T. I. Kostelnik and C. Orvig, *Chem. Rev.*, 2019, **119**, 902–956.

336 E. W. Price, J. F. Cawthray, M. J. Adam and C. Orvig, *Dalton Trans.*, 2014, **43**, 7176–7190.

337 X. Wang, M. D. G. Jaraquemada-Peláez, C. Rodríguez-Rodríguez, Y. Cao, C. Buchwalder, N. Choudhary, U. Jermilova, C. F. Ramogida, K. Saatchi, U. O. Häfeli, B. O. Patrick and C. Orvig, *J. Am. Chem. Soc.*, 2018, **140**, 15487–15500.

338 G. Gambino, T. Gambino and G. Angelovski, *Chem. Commun.*, 2020, **56**, 9433–9436.

339 A. Daina, O. Michielin and V. Zoete, *Sci. Rep.*, 2017, **7**, 1–13.

340 M. Himmelstoß, K. Erharter, E. Renard, E. Ennifar, C. Kreutz and R. Micura, *Chem. Sci.*, 2020, **11**, 11322–11330.

341 D. R. Eaton, A. D. Josey and W. A. Sheppard, *J. Am. Chem. Soc.*, 1963, **85**, 2689–2694.

342 P. Gans, A. Sabatini and A. Vacca, *J. Chem. Soc. Dalt. Trans.*, 1985, 1195–1200.

343 C. Lee, W. Yang and R. G. Parr, *Phys. Rev. B*, 1988, **37**, 785–789.

344 S. H. Vosko, L. Wilk and M. Nusair, *Can. J. Phys.*, 1980, **80**, 1200–1211.

345 J. Tomasi, B. Mennucci and E. Cancès, *J. Mol. Struct. THEOCHEM*, 1999, **464**, 211–226.

346 A. Schäfer, H. Horn and R. Ahlrichs, *J. Chem. Phys.*, 1992, **97**, 2571–2577.

347 A. Schäfer, C. Huber and R. Ahlrichs, *J. Chem. Phys.*, 1994, **100**, 5829–5835.

348 F. Weigend and R. Ahlrichs, *Phys. Chem. Chem. Phys.*, 2005, **7**, 3297–3305.

349 F. Weigend, *Phys. Chem. Chem. Phys.*, 2006, **8**, 1057–1065.

350 J. R. Cheeseman, *J. Chem. Phys.*, 1996, **104**, 5497–5509.

351 R. K. Harris, E. D. Becker, S. M. Cabral De Menezes, P. Granger, R. E. Hoffman and K. W. Zilm, *Pure Appl. Chem.*, 2008, **80**, 59–84.

352 G. Farruggia, S. Iotti, L. Prodi, M. Montalti, N. Zaccheroni, P. B. Savage, V. Trapani, P. Sale and F. I. Wolf, *J. Am. Chem. Soc.*, 2006, **128**, 344–350.

353 R. T. Bronson, M. Montalti, L. Prodi, N. Zaccheroni, R. D. Lamb, N. K. Dalley, R. M. Izatt, J. S. Bradshaw and P. B. Savage, *Tetrahedron*, 2004, **60**, 11139–11144.

354 N. B. Essien, *Chem. Res. J.*, 2018, **3**, 34–44.

355 N. B. Essien, S. Odoemelam and U. B. Essien, *Chem. Res. J.*, 2018, **3**, 74–83.

356 J. Liu, T. A. Goetjen, Q. Wang, J. G. Knapp, M. C. Wasson, Y. Yang, Z. H. Syed, M. Delferro, J. M. Notestein, O. K. Farha and J. T. Hupp, *Chem. Soc. Rev.*, 2022, **51**, 1045–1097.

357 W. Xuan, C. Ye, M. Zhang, Z. Chen and Y. Cui, *Chem. Sci.*, 2013, **4**, 3154–3159.

358 H. Zhang, L. L. Lou, K. Yu and S. Liu, *Small*, 2021, **17**, 2005686.

359 M. Ranocchiari and A. Mezzetti, *Organometallics*, 2009, **28**, 1391–1405.

360 A. Cohen, G. W. Coates and M. Kol, *J. Polym. Sci. Part A Polym. Chem.*, 2013, **51**, 593–600.

361 A. Cohen, A. Yeori, J. Kopilov, I. Goldberg and M. Kol, *Chem. Commun.*, 2008, 2149–2151.

362 G. S. Loving, S. Mukherjee and P. Caravan, *J. Am. Chem. Soc.*, 2013, **135**, 4620–4623.

363 N. A. Thiele and K. B. Sloan, *ChemMedChem*, 2016, **32610**, 1596–1599.

364 I. Piel, M. Steinmetz, K. Hirano, R. Fröhlich, S. Grimme and F. Glorius, *Angew. Chemie - Int. Ed.*, 2011, **50**, 4983–4987.